# WORK FUNCTION OF INDIUM TIN OXIDE STUDIED

# BY PHOTOEMISSION SPECTROSCOPY

**Thanit  Saisopa**

**A Thesis Submitted in Partial Fulfillment of the Requirements for the**

**Degree of Doctor of Philosophy in Physics**

**Suranaree University of Technology**

**Academic Year 2016**

# ฟังก์ชันงานของอินเดียมทินออกไซด์ศึกษาโดยเทคนิค
# โฟโตอิมิชชันสเปกโทรสโกปี

นายธนิษฐ์ สายโสภา

วิทยานิพนธ์นี้เป็นส่วนหนึ่งของการศึกษาตามหลักสูตรปริญญาวิทยาศาสตรดุษฎีบัณฑิต
สาขาวิชาฟิสิกส์
มหาวิทยาลัยเทคโนโลยีสุรนารี
ปีการศึกษา 2559

# WORK FUNCTION OF INDIUM TIN OXIDE STUDIED BY

# PHOTOEMISSION SPECTROSCOPY

Suranaree University of Technology has approved this thesis submitted in partial fulfillment of the requirements for the Degree of Doctor of Philosophy.

Thesis Examining Committee

_____

(Asst. Prof. Dr. Worawat Meevasana)

Chairperson

_____
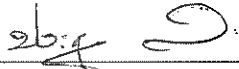
(Assoc. Prof. Dr. Prayoon Songsiriritthigul)

Member (Thesis Advisor)

_____
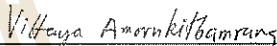
(Assoc. Prof. Dr. Vittaya Amornkitbamrung)

Member

_____

(Dr. Hideki Nakajima)

Member

_____
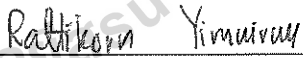
(Assoc. Prof. Dr. Rattikorn Yimnirun)

Member

_____
(Prof. Dr. Sukit Limpijumnong)

Vice Rector for Academic Affairs

and Innovation

_____
(Prof. Dr. Santi Maensiri)

Dean of Institute of Science

ธนิษฐ์ สายโสภา : ฟังก์ชันงานของอินเดียมทินออกไซด์ศึกษาโดยเทคนิคโฟโตอิมิชชัน สเปกโทรสโกปี (WORK FUNCTION OF INDIUM TIN OXIDE STUDIED BY PHOTOEMISSION SPECTROSCOPY). อาจารย์ที่ปรึกษา : รองศาสตราจารย์ ดร. ประยูร ส่งสิริฤทธิกุล, 133 หน้า.

วิทยานิพนธ์นี้มุ่งศึกษาฟังก์ชันงานของอินเดียมทินออกไซด์ โดยอาศัยเทคนิคโฟโตอิมิช ชันสเปกโทรสโกปี ในการนี้ได้มีการศึกษาสาเหตุต่าง ๆ ที่ทำให้เกิดการเปลี่ยนแปลงฟังก์ชันงาน ของอินเดียมทินออกไซด์ พบว่า การฉายด้วยแสงซินโครตรอนอัลตราไวโอเลตสุญญากาศ (VUV) ทำให้ค่าฟังก์ชันงานของอินเดียมทินออกไซด์มีค่าลดลงตามปริมาณของรังสี และที่ปริมาณของรังสี ขนาดที่เท่ากันนี้ VUV ที่มีพลังงานโฟตอนที่ต่ำกว่าจะส่งผลต่อการลดลงของฟังก์ชันงานมากกว่า VUV ที่มีพลังงานสูง เนื่องจากความสามารถในการดูดกลืนพลังงานโฟตอนโดยชั้นปนเปื้อน บริเวณพื้นผิวที่ค่าพลังงานโฟตอนต่ำมีมากกว่าพลังงานโฟตอนสูง การดูดกลืนพลังงานโฟตอนนี้ อาจทำให้เกิดการลดลงของสารปนเปื้อนบริเวณพื้นผิว ซึ่งมีผลต่อการเปลี่ยนแปลงฟังก์ชันงานของ อินเดียมทินออกไซด์ สมมติฐานนี้ได้รับการยืนยันจากการทดลองที่สิ่งปนเปื้อนบริเวณพื้นผิวได้ถูก ทำความสะอาดออก พบว่าไม่มีการเปลี่ยนแปลงฟังก์ชันงานของอินเดียมทินออกไซด์หลังจากการ ฉายด้วยVUV เป็นที่สังเกตได้ว่าเมื่อใดก็ตามที่มีสิ่งปนเปื้อนอยู่บนบริเวณพื้นผิวจะทำให้เกิดการ ลดลงของฟังก์ชันงานของอินเดียมทินออกไซด์เสมอ ซึ่งสามารถยืนยันด้วยผลจากการวัดเมื่อสัมผัส กับออกซิเจนและอากาศ

นอกจากนี้ยังเป็นที่น่าสนใจที่งานวิทยานิพนธ์นี้ได้ชี้ให้เห็นว่าฟังก์ชันงานของอินเดียม ทินออกไซด์ สามารถทำให้มีค่าเพิ่มขึ้นโดยการฉายแสงซินโครตรอนหลายรงค์ (zero-order light) ได้มีการพบว่า แสงดังกล่าวสามารถทำให้ค่าฟังก์ชันงานของอินเดียมทินออกไซด์เพิ่มขึ้นได้ถึงร้อย ละ 10 12 และ 14 เมื่อฉายด้วยเวลา 10 20 และ 30 นาที ตามลำดับ ซึ่งการเพิ่มขึ้นของฟังก์ชันงาน อาจจะเกิดจากสร้างชั้นไดโพล์ของสารปนเปื้อนบนพื้นผิวหลังจากถูกฉายด้วยโฟตอนฟลักซ์สูงของ แสงซินโครตรอนหลายรงค์ และในขณะเดียวกันพบว่ามีการลดลงของสารปนเปื้อนบริเวณผิว มากกว่ากรณีที่ฉายด้วย VUV

เทคนิคโฟโตอิมิชชันสเปกโทรสโกปียังใช้ศึกษาฟังก์ชันงานของอินเดียมทินออกไซด์ ที่ถูกปรับปรุงพื้นผิวด้วยซีเซียมฟลูออรีนและคลอรีน พบว่าด้วยเงื่อนไขที่เหมาะสมของการปรับปรุงพื้นผิวทั้งสองแบบสามารถเพิ่มค่าฟังก์ชันงานของอินเดียมทินออกไซด์ได้ถึง 5.7 eV
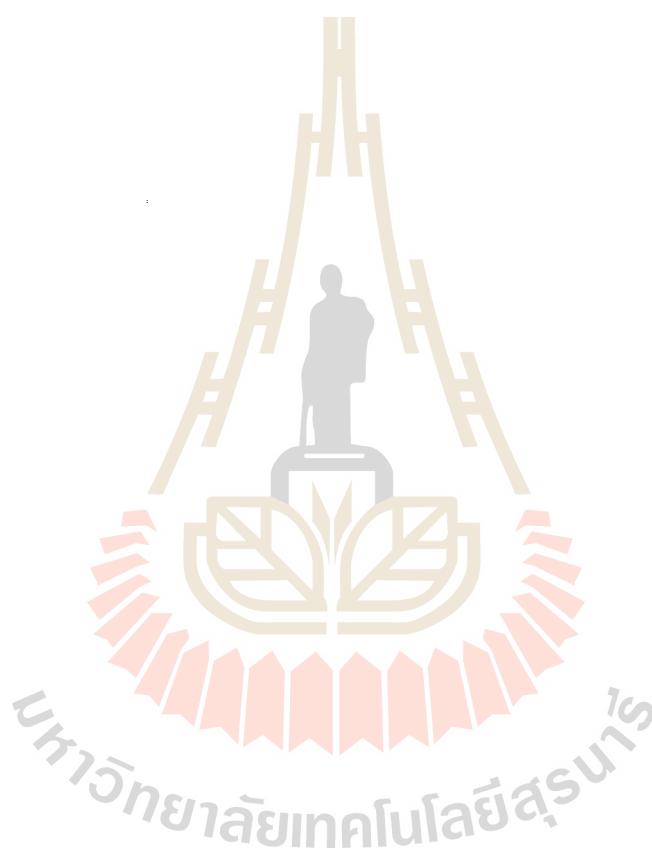
สาขาวิชาฟิสิกส์     ลายมือชื่อนักศึกษา_____

ปีการศึกษา 2559     ลายมือชื่ออาจารย์ที่ปรึกษา_____

THANIT SAISOPA : WORK FUNCTION OF INDIUM TIN OXIDE
STUDIED BY PHOTOEMISSION SPECTROSCOPY.
THESIS ADVISOR : ASSOC. PROF. PRAYOON SONGSIRIRITTHIGUL,
Ph.D. 133 PP.

INDIUM TIN OXIDE/WORK FUNCTION/PHOTOEMISSION SPECTROSCOPY/
SYNCHROTRON IRRADIATION

This thesis focuses on the study of work function of indium tin oxide (ITO)
by using synchrotron photoemission spectroscopy (PES). Various causes for the
change in the work function of ITO were investigated. When ITO is exposed to
monochromatic vacuum ultraviolet (VUV), it was found that the work function of
ITO is reduced with the exposure photon fluence. With the same value of photon
fluence, the lower photon energy gives the higher impact on the reduction of the work
function. At lower photon energy, the top most layer, surface contaminations, absorbs
more photons with lower energy than higher ones. The absorbed energy may cause
the reduction in the surface contamination resulting in the decrease in the work
function of ITO. This assumption has been experimentally confirmed; when the
surface contaminations were removed, no change in the work function was observed
after VUV irradiation. Whenever, surface contaminations exist, the reduction of the
work function of ITO is always observed. This was confirmed with air and oxygen
exposure experiments.

It is also interesting to point out that the work function of ITO can be
increased by irradiating with the zero-order light. It was found that the work function

of ITO could be increased by 10%, 12% and 14% when irradiated with the zero-order light for 10, 20 and 30 min, respectively. The cause for the increase may be due to the formation of a dipole layer on the ITO surface exposing to the high photons flux of the zero-order light. PES study also shows that the reduction of the contamination in the case of the zero-order light irradiations is much larger than when irradiated with VUV.

PES was used to measure the work function of ITO treated by CsF and by dichlorobenzene with UV light. With proper conditions, the work function of both surface treated ITO samples as high as 5.7 eV could be obtained.
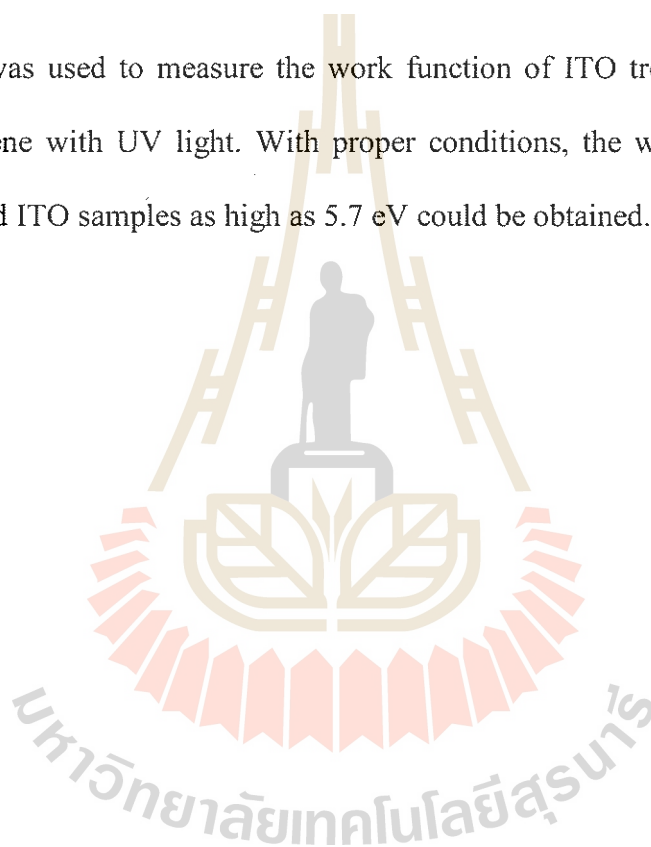
School of Physics

Academic Year 2016

Student's Signature_____

Advisor's Signature_____
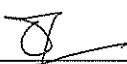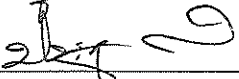
# ACKNOWLEDGEMENTS

This thesis is not just a summary of my own work. It could not be accomplished without support from many people. There are many people, to whom I would like to express my sincere words of acknowledgments:

First of all, I would like to thank Assoc. Prof. Dr. Prayoon Songsiriritthigul, my thesis advisor, thank you for introducing me to the field of photoemission spectroscopy and synchrotron radiation. Thanks for your continual support, discussions and for sharing your knowledge about from the experiments to the final proofreading of the manuscript. In addition to scientific knowledge, I also learned to enjoy performing research and daily life from you. Thank you for support me to study abroad. I feel very lucky to be your student.

I would also like to thank Prof. Dr. Kai Lin Woon for excellent collaborations. Dr. Thomas Whitcher thanks for all time spent in experiment at SLRI, great fun and a rewarding collaborations.

I am also very thankful Assoc. Prof. Dr. Vittaya Amornkitbamrung, Dr.Hideki Nakajima, Assoc. Prof. Dr. Ruttikorn Yimnirun and Asst. Prof. Dr. Worawat Meewasana for comments and suggestions and for accepting to be a member of the examination committee for my thesis.

Finally, this thesis is dedicated to my parents: my father, Thanongsak Saisopa; my mother, Somporn Saisopa and my sister Tipsuda Saisopa for your love and belief in me which has endowed me with endless power to approach my goals. I feel so proud to be your son.

Last but not least, my great thanks to my family, Theerada Saisopa my daughter, Theerawit Saisopa my son. You are my inspiration.

Thanit  Saisopa

# CONTENTS

# CONTENTS (Continued)

# LIST OF TABLES

# LIST OF FIGURES

# LIST OF FIGURES (Continued)

# LIST OF FIGURES (Continued)

# LIST OF FIGURES (Continued)

# LIST OF FIGURES (Continued)

# LIST OF FIGURES (Continued)

# LIST OF FIGURES (Continued)

# LIST OF ABBREVIATIONS

°A                Angstrom

A                 Ampere

AES               Auger electron spectroscopy

AFM               Atomic force microscopy

$Ar^+$            Argon ion

ARPES             Angle resolved photoemission spectroscopy

BL3.2Ua           Beamline 3.2Ua

°C                degree Celsius

CAE               Constant analysis energy

CHA               Concentric hemispherical analyzer

$C_x$             The atomic concentration of element x

D                 Photon density

ESCA              Electron spectroscopy for chemical analysis

e                 Electron charge ($1.602176 \times 10^{-19}$ C)

eV                Electron Volt

$E_B$             Binding energy

$E_e$             Electron energy

$E_B$             Binding energy of electron

# LIST OF ABBREVIATIONS (Continued)

| | |
|---|---|
| $E_F$ | The Fermi energy level |
| $E_{Kin}$ | Kinetic energy of electron |
| $E_{vac}$ | The vacuum energy level |
| F | Fluence |
| h | Plank's constant |
| i | Current density |
| $I_e$ | Electron current |
| $I_p$ | Photon current |
| IMPF | Inelastic mean free path |
| p | The momentum of photoelectron |
| PES | Photoemission spectroscopy |
| $R$ | Major radius of mirror |
| $R_1, R_2$ | Inner and outer hemisphere of curvature of analyzer |
| Sx | Sensitivity of element x |
| SLRI | Synchrotron Light Research Institute |
| UHV | Ultrahigh vacuum |
| UPS | Ultraviolet photoelectron spectroscopy |
| UV | Ultraviolet |

# LIST OF ABBREVIATIONS (Continued)

| | |
|---|---|
| U60 | Undulator with 60 mm of period length |
| VUV | Vacuum ultraviolet |
| XPS | X-ray photoelectron spectroscopy |
| λ | Wavelength |
| Φ, WF | Work function |
| ε | Emittance of electron beam |
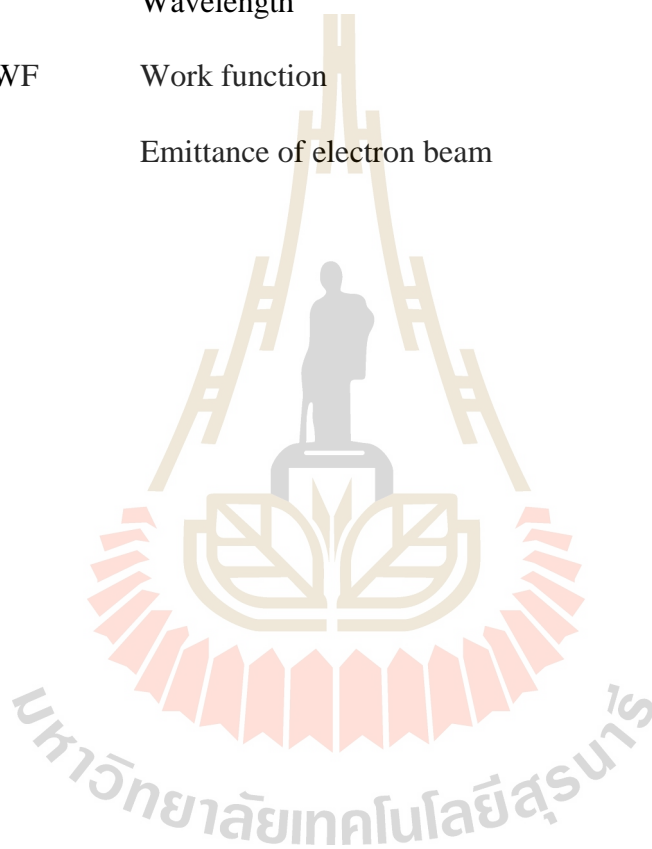
# CHAPTER I

# INTRODUCTION

Because of optical transparency and low electrical resistivity, transparent conducting oxides (TCOs) have been developed for many applications such as anti-reflection coating, heat reflecting mirrors, gas sensors, solar cells, transistors, light emitting or photo diodes, defrosting windows, electromagnetic shielding and flat-panel displays (Chiou and Tsai, 1999; Gordon, 2000; Patel *et al.*, 2003; Shaheen *et al.*, 2001). Cadmium oxide (CdO) was the first TCO introduced in 1907 (Lewis and Paine, 2000). Later, other TCO materials were introduced such as zinc oxide (ZnO), tin oxide (SnO), indium tin oxide (ITO) and cadmium tin oxide (CTO). In the last decade, thin films of TCOs have attracted attentions from many research groups because of the need for effective transparent electrode for organic light-emitting diodes (OLEDs) employed in display devices (Kim *et al.*, 1999). ITO is widely used as a transparent anode electrode (hole injection layer) for OLEDs in many commercial displays (Tang and VanSlyke, 1987). In principle, the anode electrodes in OLEDs require TCO with high work function (WF) to match with the highest occupied molecular orbital (HOMO) of organic semiconductor materials (Wang *et al.*, 2010). However, the WF of ITO is about 4.1-4.7 eV (Sugiyama *et al.*, 2000) which is lower than the HOMO level of organic semiconductors which is typically 5.7-6.3 eV (Helander *et al.*, 2011). The problem introduced by this mismatch in the energy may

be alleviated by introducing additional layers between the ITO electrode and the active layer. This increases the production cost. Thus, many research groups have focused on the development of methods to increase the WF of ITO.

It has long been known that WF of ITO can be modified by various methods. For examples, cleaning in acid-base solution (Nuesch *et al.*, 1999), UV ozone treatment (Kim *et al.*, 2004; Sugiyama *et al.*, 2000) and oxygen plasma etching (Chaney *et al.*, 2003; Ding *et al.*, 2000) have been shown to be able to increase WF of ITO. However, it is still unclear whether it is the physical or chemical changes to the surface which have the greater impact on the change of WF. Recently, Halander *et al.* reported that the increase of WF of ITO could be controlled by the degree of surface chlorination, and that the value of WF above 6.0 eV was achieved (Helander *et al.*, 2011). In addition, they demonstrated that the performance of OLED could greatly be improved when using a chlorinated ITO as the electrode.

To be able to control WF of ITO and to know the accurate value of WF are crucial for designing high performance OLED. Photoemission spectroscopy (PES) is one of a few techniques for determining WF of solids. In addition, PES is a direct and powerful technique for investigating the electronic structures and chemical information of solids and solid surfaces. Most of the experimental results reported in the past decades regarding the energy level alignment at organic material/electrode interfaces were obtained by using PES. It was realized already WF of ITO could be altered by exposing to the exciting UV (h$\upsilon$ = 21.2 eV) during PES measurements, the technique known as ultraviolet photoelectron spectroscopy (UPS). The reduction of WF of ITO by 0.5 eV during UPS measurements was reported (Schlaf *et al.*, 2001). The reduction of WF was suggested to be due to the formation of the surface dipole

induced by UV irradiation. Accurate value of WF of ITO may be obtained by PES measurements using low intensity X-ray (Al $K_\alpha$ radiation, $h\upsilon$ = 1486.7 eV), the technique known as low-intensity X-ray photoelectron spectroscopy (XPS) (Yi *et al.*, 2006).

This work focused on the investigation of the change of WF of ITO exposed to monochromatic synchrotron vacuum ultraviolet (VUV). The photon energy of VUV used in this work was chosen to be in the region where the trend of the attenuation coefficients for ITO and for hydrocarbon surface contamination are obviously distinguishable, and the variation of the coefficients in UV or VUV for ITO and for hydrocarbon surface contamination is different from that in UV and X-ray regions. This thesis work aims to provide more important pieces of information to explain the mechanism behind the change of WF of ITO induced by light. In addition to monochromatic VUV, polychromatic light covering visible light to soft X-ray is also used for irradiation to observe the change in WF of ITO. Various schemes of *in-situ* experiments were carried out to observe the change in WF of ITO by Ar+ ion sputter and oxygen and air exposures. Finally, PES was used for investigations of WF of ITO surface-treated chlorine and by caesium-fluoride.

## 1.1 References

Chaney, J. A., Koh, S. E., Dulcey, C. S. and Pehrsson, P. E. (2003). Surface chemistry of carbon removal from indium tin oxide by base and plasma treatment, with implications on hydroxyl termination. **Applied Surface Science** 218: 259.

Chiou, B.-S. and Tsai, J.-H. (1999). Antireflective coating for ITO films deposited on glass substrate. **Journal of Materials Science: Materials in Electronics** 10: 491.

Ding, X. M., Hung, L. M., Cheng, L. F., Deng, Z. B., Hou, X. Y., Lee, C. S. and Lee, S. T. (2000). Modification of the hole injection barrier in organic light-emitting devices studied by ultraviolet photoelectron spectroscopy. **Applied Physics Letters** 76: 2704.

Gordon, R. G. (2000). Criteria for Choosing Transparent Conductors. **MRS Bulletin** 25: 52.

Helander, M. G., Wang, Z. B., Qiu, J., Greiner, M. T., Puzzo, D. P., Liu, Z. W. and Lu, Z. H. (2011). Chlorinated Indium Tin Oxide Electrodes with High Work Function for Organic Device Compatibility. **Science** 332: 944.

Kim, H., Gilmore, C. M., Pique, A., Horwitz, J. S., Mattoussi, H., Murata, H., Kafafi, Z. H. and Chrisey, D. B. (1999). Electrical, optical, and structural properties of indium--tin--oxide thin films for organic light-emitting devices. **Journal of Applied Physics** 86: 6451.

Kim, S. Y., Lee, J.-L., Kim, K.-B. and Tak, Y.-H. (2004). Effect of ultraviolet--ozone treatment of indium--tin--oxide on electrical properties of organic light emitting diodes. **Journal of Applied Physics** 95: 2560.

Lewis, B. G. and Paine, D. C. (2000). Applications and Processing of Transparent Conducting Oxides. **MRS Bulletin** 25: 22.

Nuesch, F., Rothberg, L. J., Forsythe, E. W., Toan Le, Q. and Gao, Y. (1999). A photoelectron spectroscopy study on the indium tin oxide treatment by acids and bases. **Applied Physics Letters** 74: 880.

Patel, N. G., Patel, P. D. and Vaishnav, V. S. (2003). Indium tin oxide (ITO) thin film gas sensor for detection of methanol at room temperature. **Sensors and Actuators B: Chemical** 96: 180.

Schlaf, R., Murata, H. and Kafafi, Z. H. (2001). Work function measurements on indium tin oxide films. **Journal of Electron Spectroscopy and Related Phenomena** 120: 149.

Shaheen, S. E., Radspinner, R., Peyghambarian, N. and Jabbour, G. E. (2001). Fabrication of bulk heterojunction plastic solar cells by screen printing. **Applied Physics Letters** 79: 2996.

Sugiyama, K., Ishii, H., Ouchi, Y. and Seki, K. (2000). Dependence of indium--tin--oxide work function on surface cleaning method as studied by ultraviolet and x-ray photoemission spectroscopies. **Journal of Applied Physics** 87: 295.

Tang, C. W. and VanSlyke, S. A. (1987). Organic electroluminescent diodes. **Applied Physics Letters** 51: 913.

Wang, Z. B., Helander, M. G., Qiu, J., Liu, Z. W., Greiner, M. T. and Lu, Z. H. (2010). Direct hole injection in to 4,4[sup [prime]]-N,N[sup [prime]]-dicarbazole-biphenyl: A simple pathway to achieve efficient organic light emitting diodes. **Journal of Applied Physics** 108: 024510.

Yi, Y., Lyon, J. E., Beerbom, M. M. and Schlaf, R. (2006). Characterization of indium tin oxide surfaces and interfaces using low intensity x-ray photoemission spectroscopy. **Journal of Applied Physics** 100: 093719.
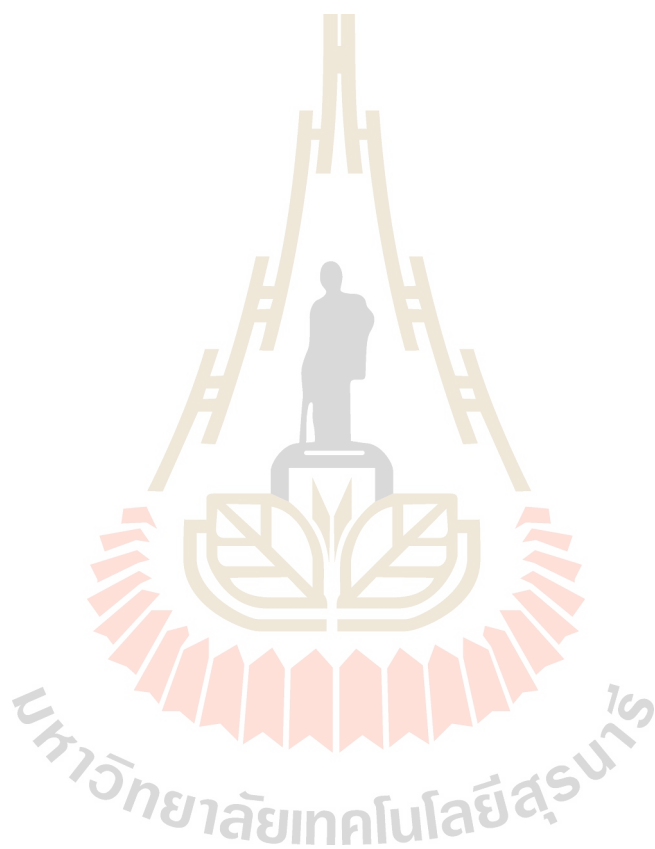
# CHAPTER II

# BACKGROUND

This chapter is a summary of the literature review on ITO, emphasizing on the topics related to this thesis work. General information of ITO, such as the crystal structure, electrical and optical properties are given in the first part of this chapter. Different deposition techniques for preparing ITO thin film are mentioned shortly. The background of the work function (WF) of ITO and surface-treated ITO is given before mentioning about the energy alignment at the interface of electrodes.

## 2.1 General properties of ITO

It is well-known that ITO is one of the most used as transparent conducting electrodes. This is due to the fact that its conductivity of about $1\times10^4$ $\Omega^{-1}cm^{-1}$ is achievable while the transmittance in visible light region can be as high as 95% (Ma *et al.*, 1995). At present, OLED lighting and display make the most use of ITO thin film as the transparent electrode (Kim *et al.*, 1999).

### 2.1.1 Crystal structure of ITO

ITO is formed by substitutional doping of $In_2O_3$ with Sn. The crystal structure of $In_2O_3$ at normal pressure and room temperature is a cubic bixbyite type structure with the space group Ia3 (Elfallal *et al.*, 1993). The lattice parameter is 1.0117 nm and

the density is 7.12 $g/cm^3$. The conventional unit cell consists of 16 formula units of $In_2O_3$, with 80 atoms in the unit cell. Two kinds of non-equivalent $In^{3+}$ sites are present in $In_2O_3$ structure as shown in Figure 2.1.

Figure 2.1 shows one quarter of the cations which is located on trigonally compressed octahedral sites, referred to as b sites, while the remaining three quarters are located on highly distorted octahedral d sites. Indium atoms, on both b and d sites, reside at the center of a distorted cube with the six corners occupied by oxygen atoms, while the remaining two corners unoccupied. In the case of the b site, oxygen vacancies are located along the body diagonal, the separation between indium and oxygen atoms is 2.18°A. In the case of the d site, oxygen vacancies are located along a face diagonal, the separation between indium and oxygen atoms are 2.13, 2.19 and 2.23°A.

For ITO, it was found that tin atoms preferentially occupy by $Sn^{4+}$ replacing the $In^{3+}$ at the cation site as shown in Figure 2.2 (Huang *et al.*, 2013). When tin atoms substitute for indium atoms, they form either $SnO$ or $SnO_2$. The material retains its bixbyite structure. However, if the doping level is extremely high, the tin atoms may enter interstitially and distort the lattice structure. As a polycrystalline structure, the ITO crystal grain size depends on various processing parameters such as substrate temperature and deposition rate.

9
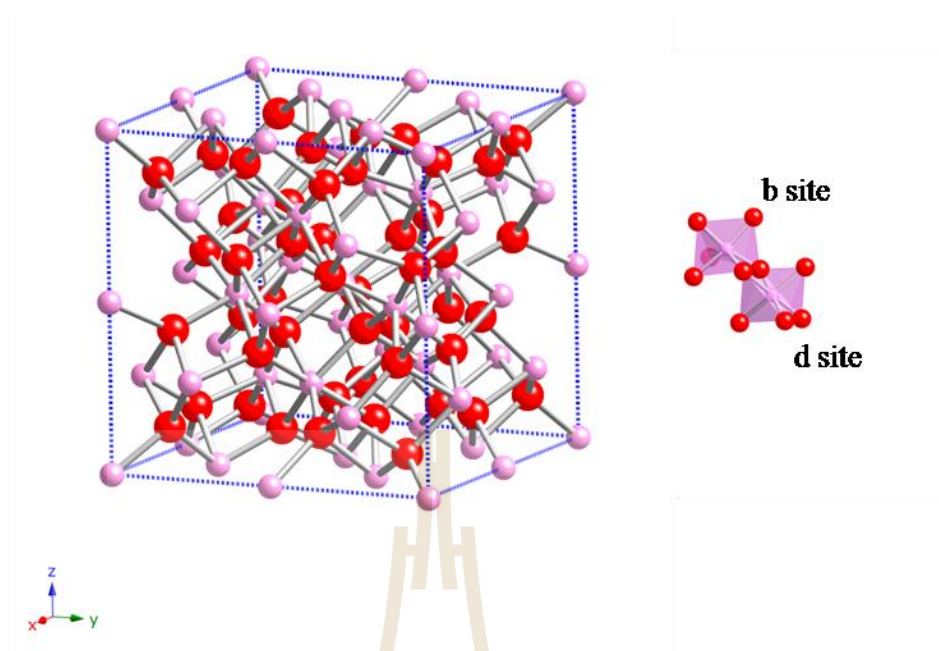


**Figure 2.1**   In$_2$O$_3$ crystal structure and two non-equivalent sites of In atoms in In$_2$O$_3$ crystal. Atomic species are color coded as follows: In (pink) and O (red). Blue lines indicate the unit cell edges (Huang *et al.*, 2013).
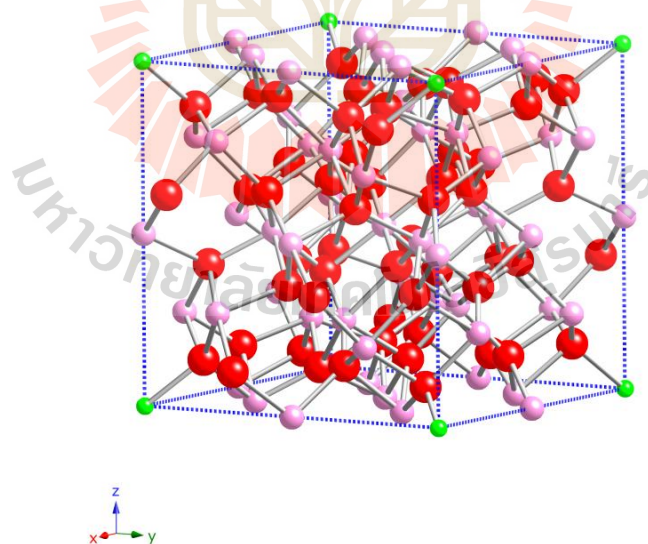


**Figure 2.2**   ITO crystal structure. Atomic species are color coded as follows: In (pink), O (red), and Sn (green). Blue lines indicate the unit cell edges (Huang *et al.*, 2013).

### 2.1.2    Electrical properties of ITO

ITO thin film is a highly degenerate n-type semiconductor with a large band gap of about 4 eV (Gupta *et al.*, 1989). The high conductivity of the ITO is due to the electrons donated to the conduction band. Because of the high carrier density, the conductivity approaches the level of metallic conduction.

The most commonly used parameters for demonstration of the electrical properties of ITO thin films are electrical conductivity ($\sigma$), mobility of charge carriers ($\mu$), and carrier density ($N$) as follows:

$$\sigma = N \times \mu \times e \tag{2.1}$$

where $e$ is the electron charge. In order to obtain films with high conductivity, high carrier concentration and mobility should be simultaneously realized. The low resistivity value of ITO film is due to a high charge carrier concentration, as the resistivity ($\rho$) is given by

$$\sigma = \frac{1}{\rho} \tag{2.2}$$

and

$$R_s = \frac{\rho}{t} \tag{2.3}$$

where $R_s$ is the sheet resistance of ITO thin films and $t$ is the thickness of the films. It means that the high charge carrier depends on the low of sheet resistance of ITO thin films.

The free charge carrier concentration of $In_2O_3$ has been reported to be in the range $10^{19}$-$10^{20}$ cm$^{-3}$. Extrinsic doping can vary the electrical properties of indium oxide significantly. The doping level is critical for electrical properties. Figure 2.3 shows the carrier concentration as a function of tin doping level. The doping level is typically chosen to be 8-10% to obtain conductivity of more than $10^3$ohm$^{-1}$cm$^{-1}$ The highest carrier concentration, which corresponds to the lowest resistivity, occurs when the tin doping level is about 10%. ITO has metal like electrical properties because the carrier density is typically in the range of $10^{20}$-$10^{21}$ cm$^{-3}$.
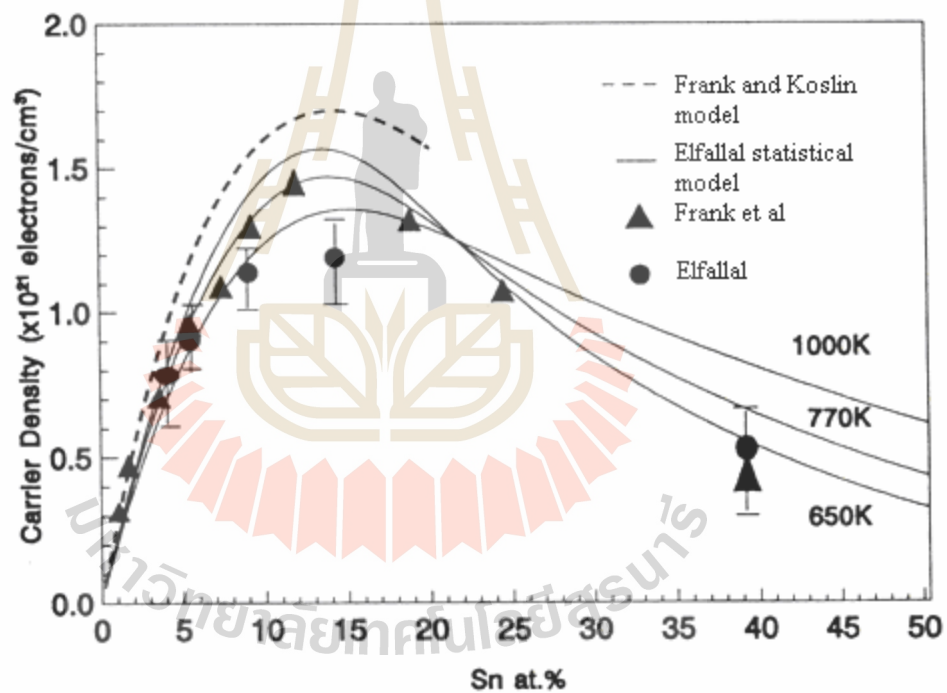


**Figure 2.3**     Illustration of the experimental and calculation of the carrier concentration as function of the tin doping level (Elfallal *et al.*, 1993).

### 2.1.3    Optical properties of ITO

The optical properties of ITO thin films are known to depend strongly on the deposition parameters, microstructures, levels of impurities and growth techniques. The variations of reflection (R) and transmission (T) characteristics of ITO films with its sheet resistance, thickness, Sn concentration have been discussed with detail as well (Bender *et al.*, 1999).

Figure 2.4 shows the optical transmission (T) and reflection (R) spectra for a typical ITO film. The ITO film shows high transmission in visible and near-IR regions of the electromagnetic spectrum as well as high reflectance to thermal infrared radiation. The high optical transmittance of these films is a direct consequence of their being a wide bandgap semiconductor. The effect of tin doping in $In_2O_3$ is generally to increase the bandgap which results in a high transmission. The transmission and reflection properties exhibited by ITO thin film have been widely put to good use in the field of sensor fabrications and applications.
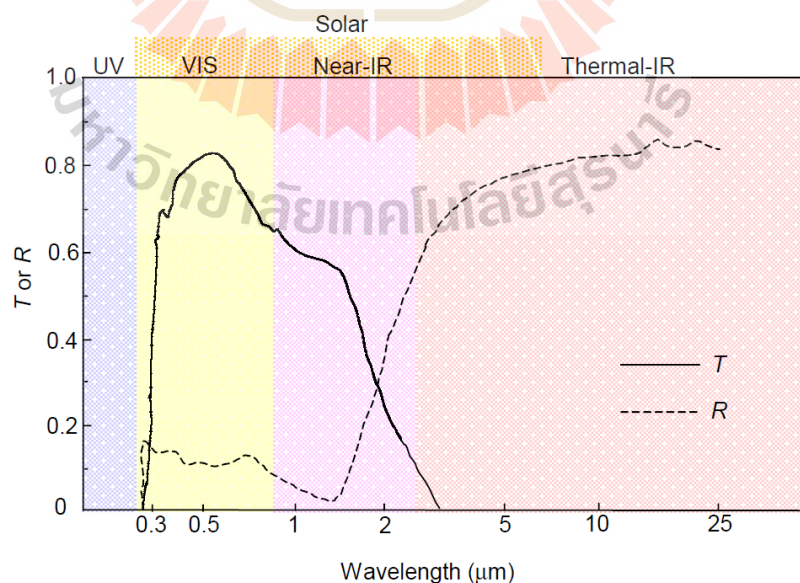


**Figure 2.4**    Typical transmission (T) and reflection (R) for ITO thin film (Hartnagel, 1995).

## 2.2    Deposition Techniques of ITO films

ITO films can be prepared by various techniques such as thermal evaporation (Paine *et al.*, 1999), sputtering deposition (Choong Hoon *et al.*, 1995; Meng and dos Santos, 1996), chemical vapor deposition (CVD) (Kane *et al.*, 1975), and spray pyrolysis (Kodigala Subba *et al.*, 2000) etc.

It is well-known that different deposition techniques usually produce ITO films with different properties. The choice of deposition techniques is determined by various factors such as quality and reproducibility of the films, the cost and complexity of the equipment, and specific disadvantage of each technique.

### 2.2.1    Thermal Evaporation Technique

Thermal evaporation involves evaporating a solid by heating the material to sufficiently high temperatures. The condensation of the vapor onto a cooler substrate yields thin solid films. The high temperature can be achieved directly or indirectly (via a support) by variety of physical methods. Such as resistively heating or by firing an electron or ion beam at the boat containing the material to be evaporated.

The reactive thermal evaporation is achieved by introducing oxygen into the chamber during deposition and is one of the most widely and successfully used techniques for good quality ITO depositions. For ITO deposition, the typical source is a 95% In - 5% Sn alloy (by weight). This technique has several advantages: it is capable of yielding films which do not contain significant amount of uncontrollable contaminations; it is relatively easy to operate; it involves a minimum of critical process parameters; and it does not cause radiation damage to the substrate (George and Menon, 2000).

Film properties strongly depend on oxygen partial pressure and film thickness, deposition rate, substrate temperature and tin concentration (Ali *et al.*, 2005). Evaporation rate is the most important parameter for the film quality. In order to obtain reproducible results and high-quality coatings it was necessary to carefully control the amount of oxygen. However, the substrate temperature is another crucial parameter. The temperature also affects the crystalline of the film. It was found that the substrate temperatures shall be raised from 300°C up to 450°C during evaporation in order to enhance conductivity and transmittance are available in the literature.

### 2.2.2 Spray Pyrolysis Technique

The spray hydrolysis method has been used for the preparation of TCO films for many years because it is relatively simple and cheap. Pyrolysis refers to the thermal decomposition of gaseous species at a heated substrate. It is sprayed by the spray nozzle with the help of a filtered carrier gas onto a preheated substrate under normal atmosphere conditions or controlled atmosphere. The ITO spray is obtained from an alcoholic solution of anhydrous indium chloride ($InCl_3$) and tin chloride ($SnCl_2$ $2H_2O$) with nitrogen acting as the carrier gas. It has been reported the resistivity of $1\times10^{-3}$ $\Omega$-cm for ITO film with transmission greater than 90% at 550 nm. However, many important control parameters are position of the substrate, the gas and solution flow rates and the chemical composition of the spray solution (Ashok *et al.*, 1980).

### 2.2.3 Screen Printing Technique

This technique is suitable for large scale non-device orientated applications where relatively thick layers of ITO are required such as in liquid crystal displays, black wall contacts and anti-reflection coatings for solar cells. Typically, the

deposited thickness varies in the range 10 to 30 μm and the post deposition crystallization temperature can be as high as 600°C for a period exceeding an hour. Although the resistivity ($>4\times10^{-4}$ Ω-cm) of the ITO film is reported to be comparable to those obtained by other deposition techniques, its transparency is markedly lower (< 80%) (Bessais *et al.*, 1993).

### 2.2.4 Chemical vapor deposition Technique

Chemical vapor deposition (CVD) is a process in which a chemical reaction involving gaseous reacting species takes place on, or in the vicinity of, a heated substrate surface.

This technique shows its merits in large-scale applications, simplicity (it may not require high or ultra-high vacuum), reproducibility and relatively low cost. However, it has not been fully exploited in growing ITO films. The technique involves a reaction of one or more gaseous reactive species on a solid surface (substrate). ITO films are generally grown by the vaporization of suitable organ metallic compounds, such as indium and tin acetyl acetonates, indium 2-ethyl hexanoate and tin chloride. The vapor containing the condensate material generated in the evaporation zone is transported to a substrate located in the reaction zone usually by an inert $N_2$ or Ar gas. The deposition parameters are the substrate temperature, substrate material, gas flow rate and the geometry of the deposition system, were found directly to influence the electrical properties greatly. Variation in the morphology of the films deposited by CVD results typically from the nature of the chemical reaction involved (Maruyama and Fukui, 1991).

### 2.2.5   Sputtering Technique

The sputtering phenomenon has been known since 1852 and exploited for deposition of various films (Wolf, 1965). Sputtering involves knocking atoms or molecules out of a target material by accelerated ions from an excited plasma and condensing it on the substrate either in its original or in a modified form. The sputtering method is one of the most extensively used techniques for the deposition of ITO films. The sputtered ITO films have been deposited by either DC or RF power. In general, most ITO sputter sources consist of hot pressed 90% $In_2O_3$ : 10% $SnO_2$ compound targets (Thøgersen *et al.*, 2011).

The quality of these films depends strongly on sputtering parameters such as sputtering rate, substrate temperature, gas composition and partial pressure in the chamber, etc (Thøgersen *et al.*, 2011). Precise control and monitoring of variations of the film qualities with these parameters are important for production of ITO films for different purposes.

## 2.3   Work function

Since the reports of ITO have shown good efficiency for transparent conductors, interest in the measurement of WF of ITO has rapidly increased. Wu *et al.* reported the WF of $O_2$ plasma treated ITO was increased (Wu *et al.*, 1997). Berntsen *et al*. also reported that WF increased by $O_2$ plasma treatment (Berntsen *et al.*, 1997). However, the difference behaviors of WF of ITO can be observed by Park *et al.* It was found that WF of $O_2$ plasma treated ITO is 4.40 eV. The WF obtained that is lower than commonly value of about 4.7 eV. This suggests that the low WF of ITO due to the adsorption of carbon contamination during storage in a vacuum before

the measurement of WF (Park *et al.*, 1996). The discrepancies of the values of WF of ITO that might be introduced when measuring in different conditions. Thus, it is important to measure absolute values of the WF of ITO so that ones can be explained the mechanism behind the variation of the WF.

It has long been known that WF of ITO can be modified by various methods of surface treatment. It was suggested that the physical or chemical changes to the surface which also have the impact on the change of the WF.

Nuesch *et al*. employed UPS to investigate the WF of ITO with acid and bases surface treatments. The ITO samples were cleaned in ultrasonic bath with chemicals solvent such as ethanol, acetone, de-ionized (DI) water followed by water solution of detergent. After that, the samples were cleaned by plasma treatment under an atmosphere of $O_2$ or $Ar_2$ with substrate temperature about 50°C for 5 minutes. Finally, each ITO was dipped with different acid or bases solutions. Figure 2.5 shows the cutoff spectra of the electron energy distribution curves of ITO with different treatments. It was found that all of the WF of ITO could be increased by acid treatment. By using $H_3PO_4$ solution, the WF could be increased about 0.7 eV, comparing to the untreated ITO. On the other hand, cleaning in the bases solution yields a decrease of WF. With the $N(C_4H_3)_4OH$ solution, the obtained of WF of ITO was about 0.5 eV smaller than the untreated ITO. It was suggested that the significant change of WF was not a result from changes in the bulk of ITO, but from the formation of a layer of ions on the surface of ITO, known as a surface dipole layer (Nuesch *et al.*, 1999).
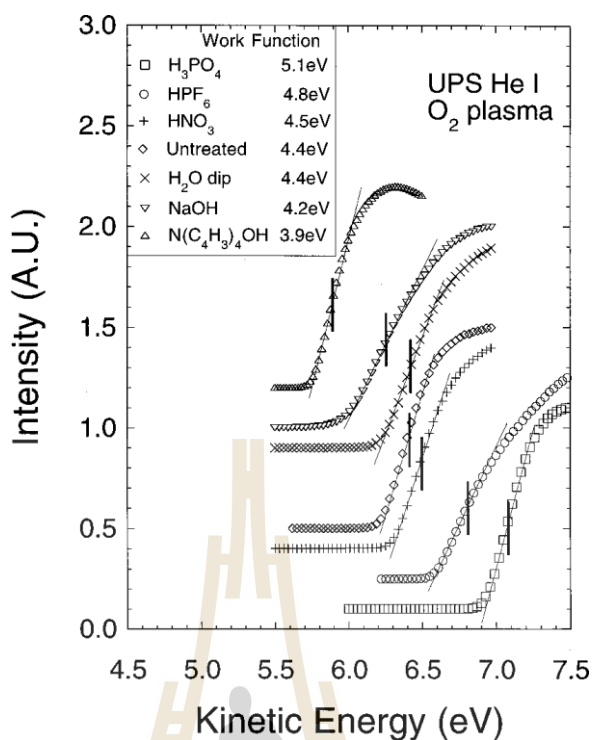
**Figure 2.5**     The cutoff spectra of the electron energy distribution curves of acid and base treatment (Nuesch *et al.*, 1999).

Sugiyama *et al*. studied the WF and chemical composition at the surface of ITO with the removal of carbon contamination by UV-ozone and by argon sputtering. The WF was measured by using UPS with He I radiation as the excitation photons and chemical composition was measured by using XPS with Mg $K_\alpha$ (1253.6 eV) as the excitation photons. Before ITO samples were treated either with UV-ozone or $Ar^+$ sputtering, the samples were cleaned in an ultrasonic bath with acetone and exposed to ipropanol vapor. UV-ozone cleaning was carried out in air for 30-15 minutes. The $Ar^+$ sputtering was done at $3\times10^{-7}$ Torr of Ar pressure with 2-keV Ar ions for 10 minutes. The experimental results showed that the UV-ozone treatment increases WF of ITO from 4.5 eV (untreated) to 4.7 eV. It was found that WF of the ITO samples cleaned by $Ar^+$ sputtering decreased to 4.3 eV. The surface chemical composition and

WF investigated in this work are given in Table 2.1. It suggested that $Ar^+$ sputtering does not only remove carbon contamination but also oxygen in the bulk. This is in contrast to the UV-ozone treatment that could remove carbon contamination but did not change the chemical composition of the ITO surface. This work suggested that both surface compositions of ITO (In:Sn:O ratio) and C-containing contaminants affect the WF of ITO (Sugiyama *et al.*, 2000).

**Table 2.1**    Chemical composition and WF of ITO with different treatment (Sugiyama *et al.*, 2000).

| Treatment | Chemical composition in at. % [a] | | | | Ratio | | Work function/ eV [b] |
|---|---|---|---|---|---|---|---|
| | O | In | Sn | C | In/Sn | O/In | |
| Acetone/i-PrOH | 46.0 | 31.5 | 3.5 | 19.0 | 9.0 | 1.46 | 4.5±0.1 |
| | (56.8) | (38.9) | (4.3) | - | | | |
| UV-ozone | 51.6 | 35.7 | 4.2 | 8.5 | 8.5 | 1.45 | 4.75±0.1 |
| | (56.4) | (39.0) | (4.6) | - | | | |
| $Ar^+$ sputtering | 50.4 | 37.5 | 4.0 | 8.1 | 9.4 | 1.34 | 4.3±0.1 |
| | (54.9) | (40.8) | (4.3) | - | | | |

[a]Estimated by XPS. The values in ( ) are the ratio without carbon.

[b]Estimated by UPS with a retarding-field type analyzer.

The effect of *in situ* $O_2$ plasma treatment and annealing on WF of ITO were also explored by Ding *et al*. (Ding *et al.*, 2000). UPS with He I radiation was used in this work for determining the WF. This work emphasized the *in situ* treatment

avoiding exposure to air prior to UPS measurements. Various schemes of sample treatment and the measured WF are summarized in Table 2.2. It was found that WF of ITO treated with *in situ* oxygen plasma.

**Table 2.2**   WF and hole injection barrier of ITO with different treatments (Ding *et al.*, 2000).

| Treatment | WF (eV) | $E_F$-HOMO (eV) |
|---|---|---|
| As-loaded or vaccum annealing | 4.4 | 1.2 |
| Ex situ ozone exposure | 4.6 | 1.0 |
| Ozone exposure + annealing | 4.5 | 1.1 |
| In situ oxygen plasma exposure | 5.2 | 0.7 |
| Oxygen plasma exposure + annealing | 4.4 | 1.2 |

Song *et al*. employed Angular-dependent XPS (ADXPS, Al Kα at 1486.6 eV) and UPS with He I radiation to study the surface chemical composition, the chemical states and WF of ITO surface treated with solvent cleaning, oxygen, argon, nitrogen plasma treatment and $Ar^+$ sputtering (Song *et al.*, 2001). Initially, the ITO sample were cleaned with detergent in distilled water and then followed by solution of ethanol and acetone in an ultrasonic bath for 15 minutes. The samples were subsequently treated with plasma treatment under oxygen, argon, or nitrogen atmosphere. ADXPS measurements were done with different take-off angles aiming to obtain the information within different depths. The results suggested that all methods employed caused changes only at ITO surface. The $O_2$ plasma was found to be more effective for increasing the WF than solvent. The increase of WF was found

when carbon contamination was reduced and the O/In ratio was increased. On the other hand, $Ar^+$ sputtering led to the decrease of WF by 0.5 eV. The O/In ratio was also found to be decreased.

Accurate determination of WF is thus important. Photoemission spectroscopy (PES) has long been as one of a few techniques for measuring the WF of ITO. It is well known that WF of ITO could be altered to lower values during PES measurements. The reduction of the WF up to ~0.5 eV has been first reported when UV light (21.2 eV) was used in PES measurements (Schlaf *et al.*, 2001).

Systematic investigation on the influence of UV and soft X-ray (SX, 1.4 keV Al $K_\alpha$) irradiation on the change of WF of ITO also showed that the WF of ITO decreases with increasing fluence of UV and SX irradiation (Yi *et al.*, 2006). It was clear that standard UPS measurements induce the reduction of the WF of ITO within a second or less. XPS measurements also shows that a more gradual WF change over the course of hundreds of seconds. The reduction of WF was not observed when using low flux Al-$K_\alpha$ excitation. The reduction of the WF was suggested to be caused by photo-induced chemical interaction on the surface. So far, no clear evidences have been confirmed.

In comparison, Kelvin probe WF measurements *in situ* confirmed this artifact, and also demonstrated that low intensity X-ray photoemission (LIXPS) of WF measurements do not result in a WF reduction (Beerbom *et al.*, 2006). The Kelvin probe is a non-contact and non-destructive of the sample. The WF can be defined by measuring the flow of charge which has difference of the average WF between a sample and vibrating plate (tip) (Dieter, 2001). Thus, Kelvin probe (KP) WF values are often higher than those measured by UPS. KP integrates over the size of the

samples; although it relies on measuring a current, it has been shown that it correctly maps the surface potential also for poor conducting surfaces. Whereas UPS measures the lowest WF patch on the surface, even if it is only a small fraction of the surface area and thus UPS is very surface sensitive. The vacuum level (VL) shift relative to the substrate $E_F$ (dipole formation), or the ionization potential (IP) can be determined (Kim *et al.*, 2000).

It is well known that one of the difficulties to improve the performance of OLEDs is to find an optically transparent anode electrode with sufficiently high WF. The low WF of ITO led to the problem of hole injection which has a large energy barrier for hole injection at the interface between ITO surface and hole transport materials (HTMs). The mismatch of the energy level affects the performance of OLEDs. This results in low efficiency devices, requiring high operating voltage (Milliron *et al.*, 2000). Many efforts to modify ITO surface to obtain the required WF are summarized below.

More effective method to increase the WF of ITO was experimented by modifying ITO surface with solution of iodine, bromine and bromine vapor evaporation (Sun *et al.*, 2003). UPS with He I radiation was used in this work for determining the WF. Prior to surface modifications, the ITO samples were cleaned by detergent and DI water in ultrasonic bath and UV ozone treated for 20 minutes. After that the samples were treated in $I_2$ solution (with concentration 0.15 M), $Br_2$ solution (with concentration 0.15 M) or $Br_2$ vapor evaporation (with concentration 2.0 M). The WF of the ITO samples studied in this work is given in Table 2.3. The increase of WF of 0.9 eV could be achieved by using treating ITO in $Br_2$ vapor. The increase of WF was explained by the formation of surface dipole layer which the negative charge of

iodine and bromine acts as a barrier for electrons to escape out from the surface. This leads to the increase of WF. This work also demonstrated the improved performance of OLED with ITO modified by bromine. The increase in WF and reduce in hole injection barrier of modified surface of ITO yield higher efficiency of OLED, which has high current density and luminescence and low drive voltage. Figure 2.6 shows current density and luminescence as a function of operating voltage of OLEDs that employed bromine-modified-surface ITO and untreated ITO as an anode electrode.

**Table 2.3**    WF and hole injection barrier of ITO with different surface modifications (Sun *et al.*, 2003).

| Treatment | Work function (eV) | $E_F$-HOMO (eV) |
|---|---|---|
| Non-treated ITO | 4.4 | 1.2 |
| *Ex situ* ozone exposure | 4.5 | 1.1 |
| *In situ* oxygen plasma exposure | 5.2 | 0.7 |
| $I_2$ solution (0.15 M) | 5.2 | 0.5 |
| $Br_2$ solution (1.2 x $10^{-3}$ M) | 5.3 | 0.6 |
| $Br_2$ vapor (2.0 M) | 5.4 | 0.4 |
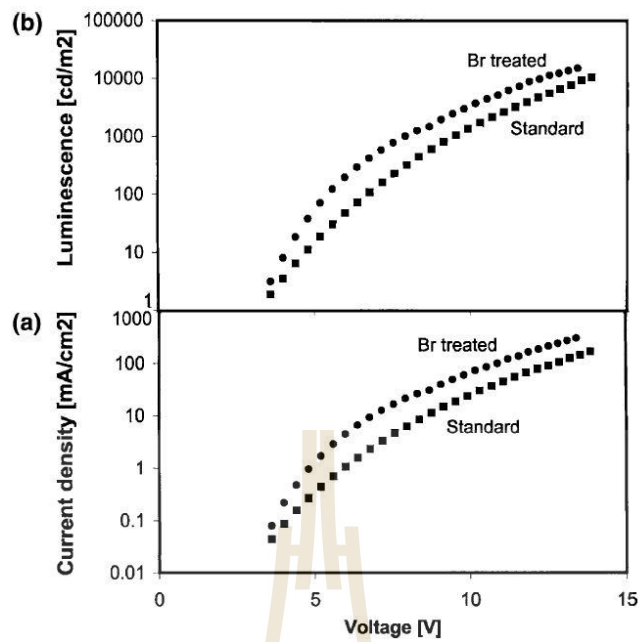
**Figure 2.6**   Current density (b) Luminescence versus voltage of OLED with bromine-vapor treated ITO and standard ITO (Sun *et al.*, 2003).

Recently, there has been report of a systematic investigation of the thermal decomposition of $C_{60}F_{36}$ thin films on ITO (Mao *et al.*, 2013). The WF of ITO can be enhanced by introducing a surface dipole layer, results in the increase of the WF of ITO to 5.62 eV at annealing of 120°C. By using XPS It was found that F atoms are chemically bonded onto the ITO surface after annealing. The schematic illustration of the increased of WF of ITO after annealing is shown in Figure 2.7.
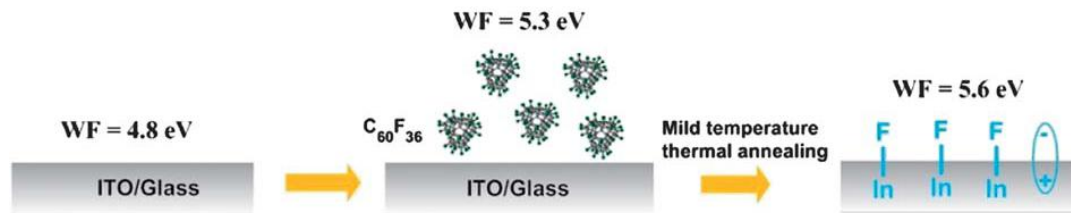
**Figure 2.7**    Schematic diagram showing the effect of polar In–F bonds on the substrate WF (Mao *et al.*, 2013).


A systematic study of the enhancement of WF of ITO by chlorination and the effects on device performance was recently reported by Helander *et al*. (Helander *et al.*, 2011). It was found that WF of ITO could be tuned between 6.1-4.7 eV by the degree of surface chlorination, or the amount of chlorine atom chemically bound to the surface of ITO. Before chlorinating process, the ITO samples were cleaned with alconox, acetone, and methanol in an ultrasonic bath and followed by exposing to UV-ozone for 15 minutes. Surface chlorination of ITO was performed in a closed Pyrex reaction vessel with o-dichlorobenzene under UV radiation with different exposure times between 0-10 minutes. Figure 2.8A shows that the secondary electron cut-off spectra of chlorinated ITO (Cl-ITO) with different exposure times. The cut-off spectra were shifted from the higher to lower binding energy with increasing exposure time, indicating an increase in WF. The intensity of the Cl 2p was also found to increase with exposure time, as shown in Figure 2.8B. Figure 2.8C shows an increase in the intensity of the Cl 2p core level at the low take-off angles. This indicates that Cl atoms were confined to the surface of Cl-ITO and also shows that the surface of the Cl is only one monolayer. Figure 2.8D shows the WF of chlorinated-ITO as a linear function of Cl surface coverage. This work also demonstrated the surface stability of

Cl-ITO samples, which are more stable than untreated ITO surface, as shown in Figure 2.8E. It was suggested that the increase of WF was caused by Cl atoms on the surface inducing the dipole surface which is equivalent to the induced of dipoles layer. This surface dipole increases charge on the external surface, preventing electrons to be removed from the surface.
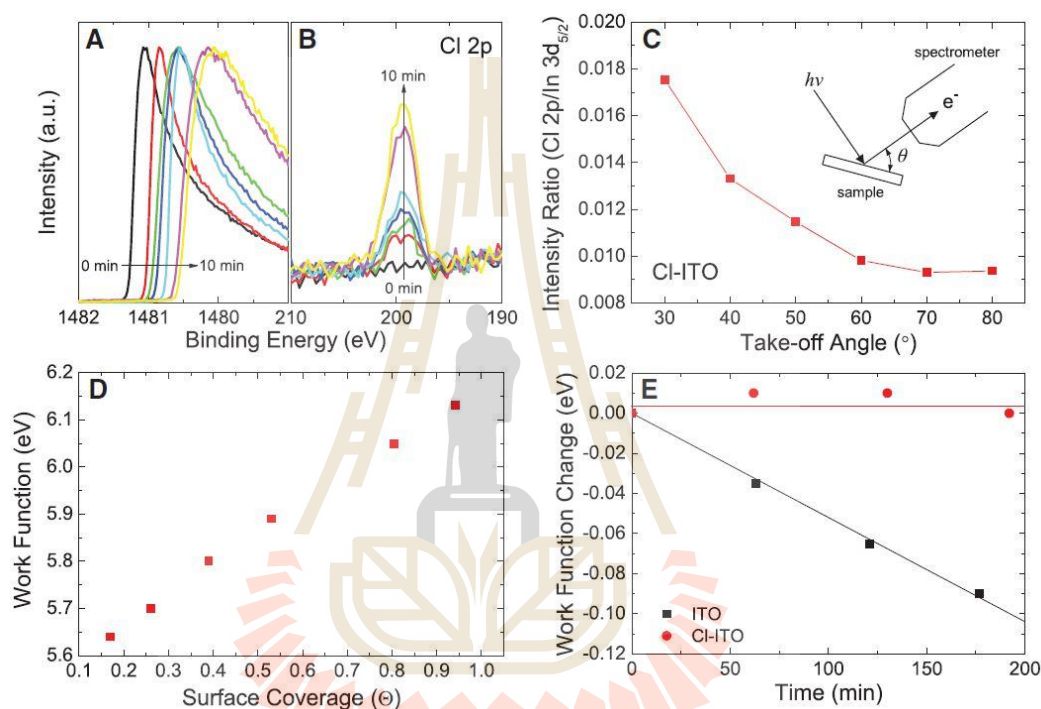


**Figure 2.8** (A) Secondary electron cut-off energy, (B) Cl 2p peak in function of treatment time. (C) Take-off angle of Cl 2p. (D) WF of Cl-ITO with Cl surface converage. (E) The change of WF CL-ITO and ITO over time (Helander *et al.*, 2011).

Figure 2.9A shows a schematic energy-level diagram of the OLED with Cl-ITO anode. The reduction of the barrier height when coating with 4,4'-N, N-dicarbazole-biphenyl (CBP) on the Cl-ITO with different the WF. The hole injection barrier can be reduced about 0.7 eV (Figure 2.9B), which is due to the increase of the

WF and that the operating voltage of the OLED could be reduced significantly because of the reduction of the hole injection barrier (Figure 2.8C).
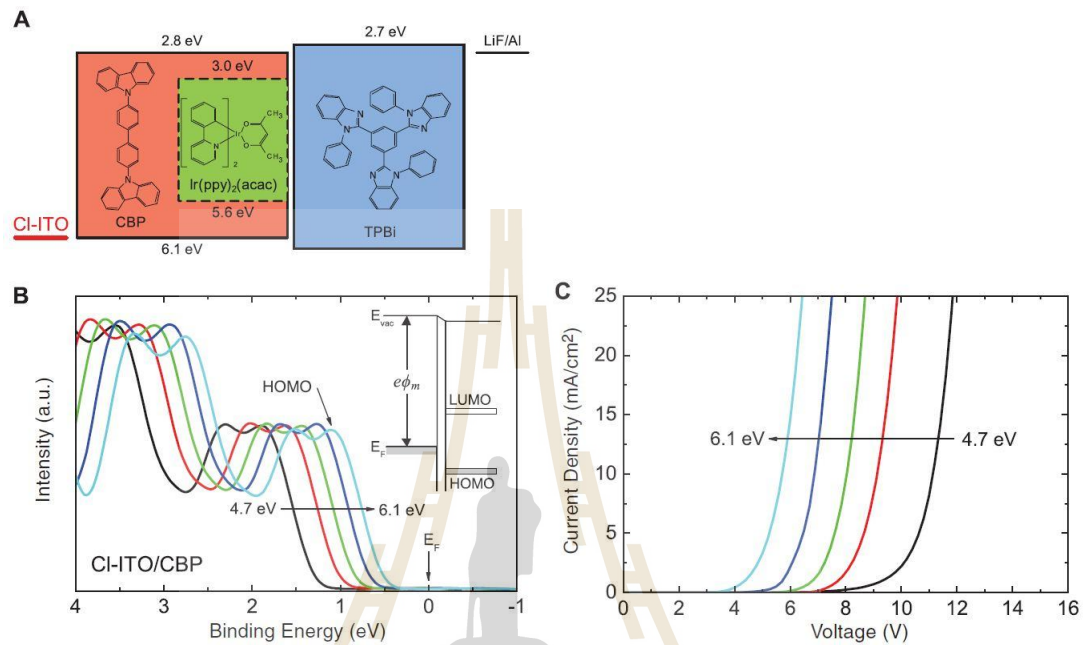


**Figure 2.9**    (A) Schematic energy-level diagram of the OLED with Cl-ITO anode. (B) UPS measurement of the hole injection barrier, (C) current density versus voltage with different WF (Helander *et al.*, 2011).

## 2.4    Energy level alignment

The mechanism of operation of organic devices, for example OLED, is the following (Grobosch, 2011):

- The injection of charge carriers of different polarities from cathode and anode, respectively, into the organic multilayer (metal-organic interface).

- The transfer of charge carriers from one organic layer to another (organic-organic interface).

- The electron-hole recombination and emission of radiation.

The properties of the interface between the organic layers and the electrodes are determinant for the efficiency of the devices. Therefore a good understanding of the interface between the organic layers and the electrodes is crucial to achieve good organic optoelectronic devices. Often, the WF of the sample is obtained from the measurement of the contact potential on a reference material, whose WF is well-known as the minimum energy required to remove an electron from the sample.

Energy level alignment at organic material/electrode interfaces is one of the main fundamental issues about the optoelectronic devices. The simple Schottky-Mott model has been often applied to organic contacts.

Figure 2.10 shows the Schottky-Mott model when an organic semiconductor is put in contact with an electrode. The Schottky-Mott model assumes an alignment of the vacuum level and a band bending in the space charge layer (SCL) to achieve alignment of the bulk Fermi levels. Therefore the barrier height for hole extraction $\Phi_B$ corresponds to:

$$\Phi_B = \Phi_M - \Phi_S \qquad (2.4)$$

where $\Phi_M$ is the WF of the metal and $\Phi_S$ is the WF of the organic semiconductor.

In case of the vacuum level does not align at the interface. This interface dipole (ID) induces vacuum level shift $\Delta$ as shown in Figure 2.5(a). Therefore the Mott-Schottky barrier height should be modified by the amount of $\Delta$:

$$\Phi_B = \Phi_M - \Phi_S - \Delta \qquad (2.5)$$

The $\Delta$ depends on the nature of the contact. It has been shown that localized energy levels of the organic material are shifted depending on the distance to the metal interface, until depletion region thickness is reached. This dipole can increase or

decrease the potential barrier present at the interface. However, this dipole is only one contribution to the interface barrier, the difference between the WF of the electrode (anode-cathode) and the energy level (HOMO-LUMO) of the organic material is another significant contribution, which allows predicting, at least roughly, the behavior of the contact.
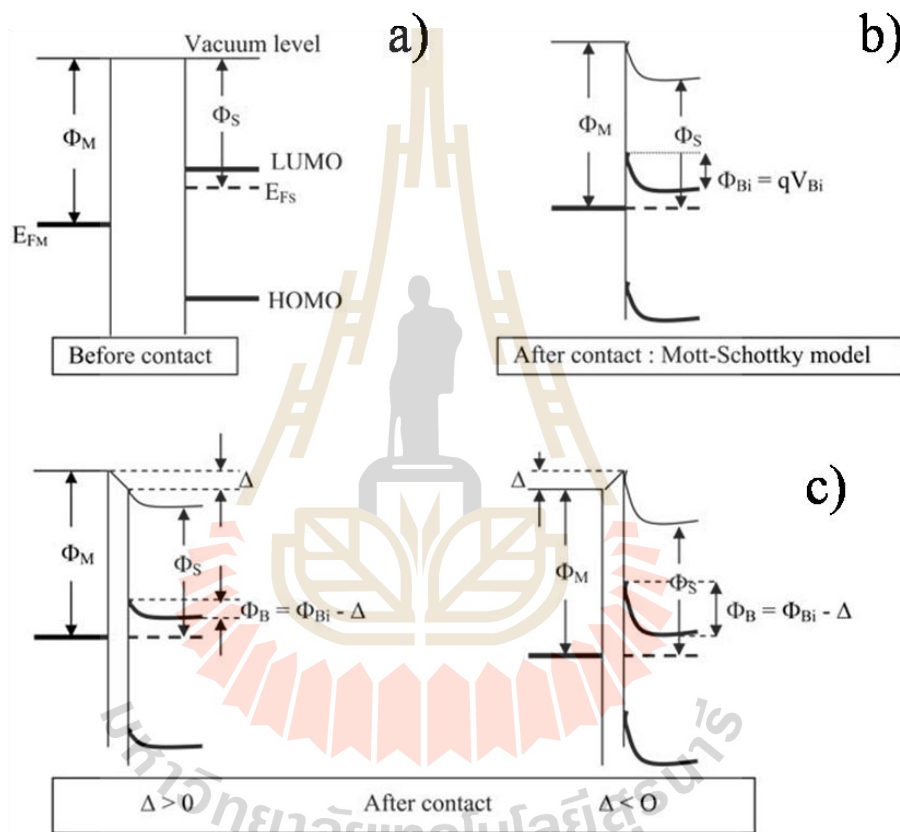


**Figure 2.10**    Interface band alignments, a) before contact, b) after contact without and c) after contact with an interface dipole (Grobosch, 2011).

Most of the experimental publications that have been reported in the past decades regarding the energy level alignment at organic material/electrode interfaces. It has been obtained by photoemission spectroscopy (PES). For the investigation of the chemistry and electronic properties of interfaces X-ray photoelectron spectroscopy (XPS) and ultraviolet photoelectron spectroscopy (UPS) are often used. UPS has been extensively used to study the energy level alignment at the interfaces. The UPS spectra give information about the electronic structure of the material and its WF. The energies of several important molecular levels can be directly obtained from the UPS spectrum by simple analysis, including the vacuum level, the Fermi level (for metallic surfaces) and the HOMO or valence band maximum (for semiconducting surfaces) as shown in Figure 2.11. It also measures the change Δ of WF that can be tracked by remeasuring the $E_{cutoff}$ after deposition of an organic monolayer.
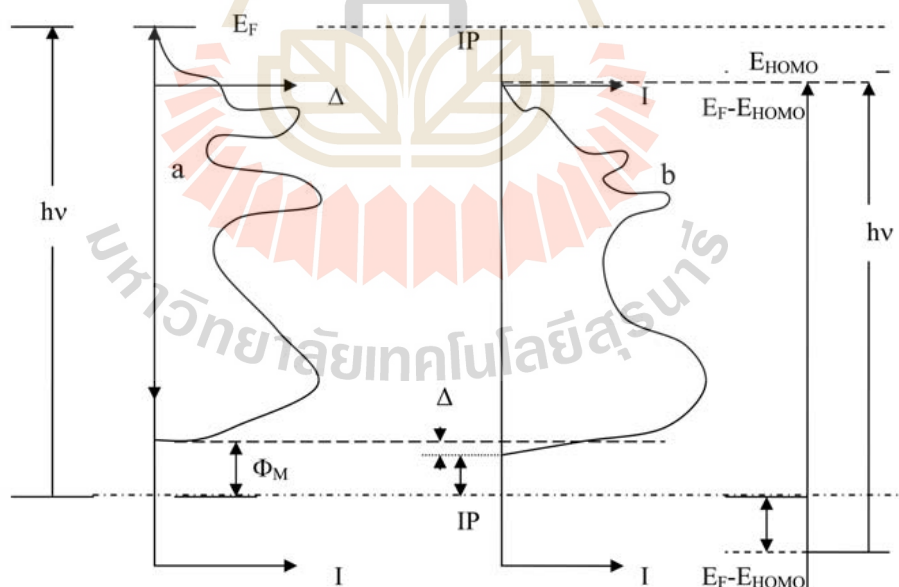


**Figure 2.11** Schematic of determination of the interface parameters at organic material/electrode interfaces using ultraviolet photoemission spectroscopy (Grobosch, 2011).

## 2.5    References

Ali, H. M., Mohamed, H. A. and Mohamed, S. H. (2005). Enhancement of the optical and electrical properties of ITO thin films deposited by electron beam evaporation technique. **European Physical Journal Applied Physics.** 31: 87.

Ashok, S., Sharma, P. P. and Fonash, S. J. (1980). Spray-deposited ITO—Silicon SIS heterojunction solar cells. **IEEE Transactions on Electron Devices** 27: 725.

Beerbom, M. M., Lägel, B., Cascio, A. J., Doran, B. V. and Schlaf, R. (2006). Direct comparison of photoemission spectroscopy and in situ Kelvin probe work function measurements on indium tin oxide films. **Journal of Electron Spectroscopy and Related Phenomena** 152: 12.

Bender, M., Trube, J. and Stollenwerk, J. (1999). Deposition of transparent and conducting indium-tin-oxide films by the r.f.-superimposed DC sputtering technology. **Thin Solid Films** 354: 100.

Berntsen, A. J. M., Croonen, Y., Cuijpers, R., Habets, B., Liedenbaum, C. T. H. F., Schoo, H. F. M., Visser, R. J., Vleggaar, J. J. M. and van de Weijer, P. (1997) Polymer light-emitting diodes: from materials to devices. Vol. 3148, pp. 264.

Bessais, B., Ezzaouia, H. and Bennaceur, R. (1993). Electrical behaviour and optical properties of screen-printed ITO thin films. **Semiconductor Science and Technology** 8: 1671.

Choong Hoon, Y., Yuzo, S., Itaru, Y. and Satoru, T. (1995). Microstructure of Low-Resistivity Tin-Doped Indium Oxide Films Deposited at 150~200 °C. **Japanese Journal of Applied Physics** 34: L244.

Dieter, K. S. (2001). Surface voltage and surface photovoltage: history, theory and applications. **Measurement Science and Technology** 12: R16.

Ding, X. M., Hung, L. M., Cheng, L. F., Deng, Z. B., Hou, X. Y., Lee, C. S. and Lee, S. T. (2000). Modification of the hole injection barrier in organic light-emitting devices studied by ultraviolet photoelectron spectroscopy. **Applied Physics Letters** 76: 2704.

Elfallal, I., Pilkington, R. D. and Hill, A. E. (1993). Formulation of a statistical thermodynamic model for the electron concentration in heavily doped metal oxide semiconductors applied to the tin-doped indium oxide system. **Thin Solid Films** 223: 303.

George, J. and Menon, C. S. (2000). Electrical and optical properties of electron beam evaporated ITO thin films. **Surface and Coatings Technology** 132: 45.

Grobosch, M. (2011). Electronic Properties of Organic Semiconductor/Electrode Interfaces: The Influence of Contact Contaminations on the Interface Energetic. **The Open Applied Physics Journal** 4: 8.

Gupta, L., Mansingh, A. and Srivastava, P. K. (1989). Band gap narrowing and the band structure of tin-doped indium oxide films. **Thin Solid Films** 176: 33.

Hartnagel, H. (1995). **Semiconducting Transparent Thin Films**. Taylor & Francis.

Helander, M. G., Wang, Z. B., Qiu, J., Greiner, M. T., Puzzo, D. P., Liu, Z. W. and Lu, Z. H. (2011). Chlorinated Indium Tin Oxide Electrodes with High Work Function for Organic Device Compatibility. **Science** 332: 944.

Huang, P.-R., He, Y., Cao, C. and Lu, Z.-H. (2013). The origin of the high work function of chlorinated indium tin oxide. **NPG Asia Mater** 5: e57.

Kane, J., Schweizer, H. P. and Kern, W. (1975). Chemical vapor deposition of transparent electrically conducting layers of indium oxide doped with tin. **Thin Solid Films** 29: 155.

Kim, H., Gilmore, C. M., Piqué, A., Horwitz, J. S., Mattoussi, H., Murata, H., Kafafi, Z. H. and Chrisey, D. B. (1999). Electrical, optical, and structural properties of indium–tin–oxide thin films for organic light-emitting devices. **Journal of Applied Physics** 86: 6451.

Kim, J. S., Lägel, B., Moons, E., Johansson, N., Baikie, I. D., Salaneck, W. R., Friend, R. H. and Cacialli, F. (2000). Kelvin probe and ultraviolet photoemission measurements of indium tin oxide work function: a comparison. **Synthetic Metals** 111–112: 311.

Kodigala Subba, R., Raja, V. S., Bhatnagar, A. K., Tomlinson, R. D., Pilkington, R. D., Hill, A. E., Chang, S. J., Su, Y. K. and Juang, F. S. (2000). Optical, structural and electrical properties of tin doped indium oxide thin films prepared by spray-pyrolysis technique. **Semiconductor Science and Technology** 15: 676.

Ma, H. L., Zhang, D. H., Ma, P., Win, S. Z. and Li, S. Y. (1995). Preparation and properties of transparent conducting indium tin oxide films deposited by reactive evaporation. **Thin Solid Films** 263: 105.

Mao, H. Y., Wang, R., Zhong, J. Q., Zhong, S., Lin, J. D., Wang, X. Z., Chen, Z. K. and Chen, W. (2013). A high work function anode interfacial layer via mild temperature thermal decomposition of a C60F36 thin film on ITO. **Journal of Materials Chemistry C** 1: 1491.

Maruyama, T. and Fukui, K. (1991). Indium tin oxide thin films prepared by chemical vapour deposition. **Thin Solid Films** 203: 297.

Meng, L.-J. and dos Santos, M. P. (1996). Structure effect on electrical properties of ITO films prepared by RF reactive magnetron sputtering. **Thin Solid Films** 289: 65.

Milliron, D. J., Hill, I. G., Shen, C., Kahn, A. and Schwartz, J. (2000). Surface oxidation activates indium tin oxide for hole injection. **Journal of Applied Physics** 87: 572.

Nuesch, F., Rothberg, L. J., Forsythe, E. W., Toan Le, Q. and Gao, Y. (1999). A photoelectron spectroscopy study on the indium tin oxide treatment by acids and bases. **Applied Physics Letters** 74: 880.

Paine, D. C., Whitson, T., Janiac, D., Beresford, R., Yang, C. O. and Lewis, B. (1999). A study of low temperature crystallization of amorphous thin film indium–tin–oxide. **Journal of Applied Physics** 85: 8445.

Park, Y., Choong, V., Gao, Y., Hsieh, B. R. and Tang, C. W. (1996). Work function of indium tin oxide transparent conductor measured by photoelectron spectroscopy. **Applied Physics Letters** 68: 2699.

Schlaf, R., Murata, H. and Kafafi, Z. H. (2001). Work function measurements on indium tin oxide films. **Journal of Electron Spectroscopy and Related Phenomena** 120: 149.

Song, W., So, S. K. and Cao, L. (2001). Angular-dependent photoemission studies of indium tin oxide surfaces. **Appl Phys A** 72: 361.

Sugiyama, K., Ishii, H., Ouchi, Y. and Seki, K. (2000). Dependence of indium--tin--oxide work function on surface cleaning method as studied by ultraviolet and x-ray photoemission spectroscopies. **Journal of Applied Physics** 87: 295.

Sun, X. H., Cheng, L. F., Liu, M. W., Liao, L. S., Wong, N. B., Lee, C. S. and Lee, S. T. (2003). Photoelectron spectroscopic study of iodine- and bromine-treated indium tin oxides and their interfaces with organic films. **Chemical Physics Letters** 370: 425.

Thøgersen, A., Rein, M., Monakhov, E., Mayandi, J. and Diplas, S. (2011). Elemental distribution and oxygen deficiency of magnetron sputtered indium tin oxide films. **Journal of Applied Physics** 109: 113532.

Wolf, E. (1965). **Progress in Optics**. Elsevier Science.

Wu, C. C., Wu, C. I., Sturm, J. C. and Kahn, A. (1997). Surface modification of indium tin oxide by plasma treatment: An effective method to improve the efficiency, brightness, and reliability of organic light emitting devices. **Applied Physics Letters** 70: 1348.

Yi, Y., Lyon, J. E., Beerbom, M. M. and Schlaf, R. (2006). Characterization of indium tin oxide surfaces and interfaces using low intensity x-ray photoemission spectroscopy. **Journal of Applied Physics** 100: 093719.

# CHAPTER III

# EXPERIMENTAL TECHNIQUES AND

# EXPERIMENTAL SETUP

This chapter describes the background of photoemission spectroscopy and experimental set up. The PES experiment was carried out at the photoemission beamline (BL3.2Ua) at the Synchrotron Light Research Institute (SLRI). Thus the synchrotron radiation source and the beamline instrument setup for using photoemission spectroscopy measurements are described. Moreover, the preparation of the samples and experiment parameters are also included in this chapter.

## 3.1    Photoemission spectroscopy (PES)

Photoemission Spectroscopy (PES) is a widely used technique to investigate electronic structure and chemical analysis of atoms, molecules, solids, gases and liquid. The technique based on the photoelectric effect was first observed by Hertz since 1887 and then described by Albert Einstein in 1905 (Einstein, 1905; Hertz, 1887). The concept of photons was used to explain the ejection of electrons from a metallic surface as shown in Figure 3.1.
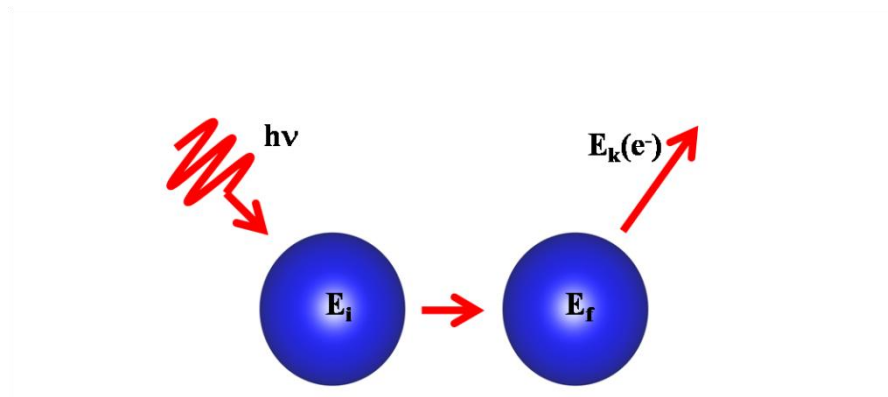
**Figure 3.1**    Schematic drawing illustrating the process of photo-ionization.

When the photons with sufficient energy interact with atoms in a sample, photoelectrons are emitted from the sample. The kinetic energy ($E_{kin}$) of the photoelectrons is measured by an electron energy analyzer. The experimental technique has been developed in the mid-1950's by Kai Siegbahn and his research group at the Uppsala University in Sweden, known as Electron Spectroscopy for Chemical Analysis (ESCA) (Hagström *et al.*, 1964).

In the energy consideration, the photoemission process is governed by the conservation of energy. Before the photon interact with the target atom ($A$), the equation can be written as

$$hv + A = A^+ + e^-  \qquad (3.1)$$

The total energy of the initial state is defined by the summation of the photon energy ($hv$) and the energy of the target atom ($E_i$). For final state, the ionized atom ($A^+$) in final state can absorb the energy of the photon into the energy of final state ($E_f$) and then emitting a photoelectron ($e^-$) from the target atom with the kinetic energy $E_{kin}$ ,

$$hv + E_i = E_f + E_{kin} \tag{3.2}$$

The kinetic energy ($E_{kin}$) of the photoelectron is given by

$$E_{kin} = hv - E_B \tag{3.3}$$

where $E_B$ ($E_f - E_i$) is the binding energy difference in energy between the ionized and neutral atoms. The binding energy in solids is normally defined with respect to the Fermi level ($E_F$) at the top of the occupied state in metals, which is separated from the vacuum level by the sample work function ($WF$ or $\Phi_s$) as shown in Figure 3.2. WF is the minimum energy required to remove an electron from the solid, then the equation becomes.

$$E_{kin} = hv - E_B - \Phi_s \tag{3.4}$$

Figure 3.2 shows the energy distribution of electrons exited by photons. The photoelectrons originate from the occupied energy levels, including the valence band and core level. For the binding energy of core levels, each element has a characteristic of electronic states that are different for all elements. Besides, the spectrum of the valence bands that is made up of electrons forming bonds provides information for investigations of the electronic structure of solids.
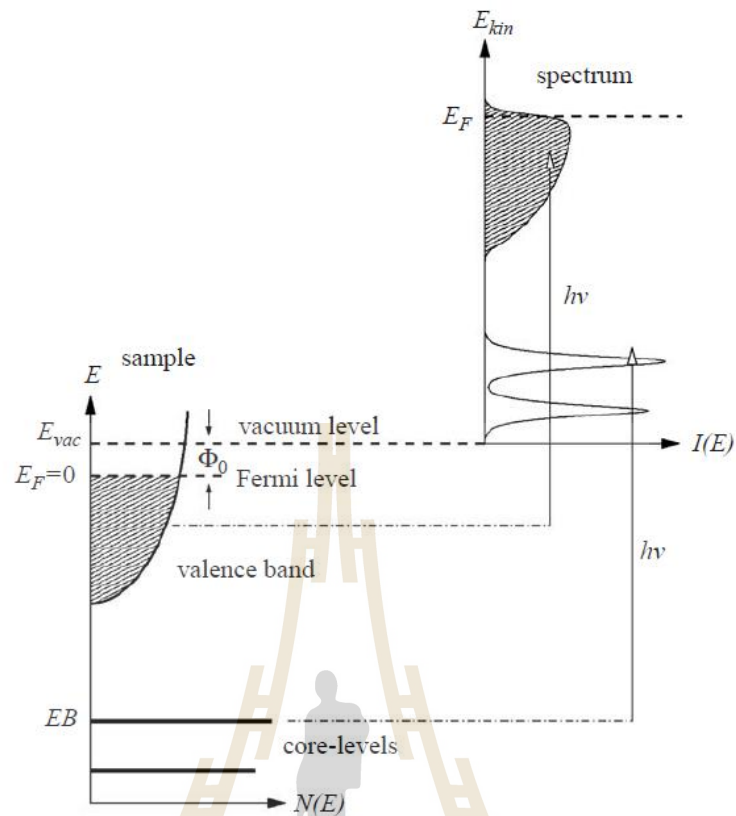
**Figure 3.2** Schematic view of the photoemission illustrating the excitation to the ionization of various energy levels, divided into core level and valence level (Hüfner *et al.*, 2005).

Photoemission of solids may be explained within the frame of the three-step model and the free-electron final state approximation (Hüfner *et al.*, 2005). The three-step model is a phenomenological approach that splits the photoemission process into three steps. First, the electron is excited by a photon from an initial state into a final state, then it travels through the sample to the surface and finally it escapes through the surface into the vacuum, where it is detected by the analyzer. The three step model is illustrated in Figure 3.3.
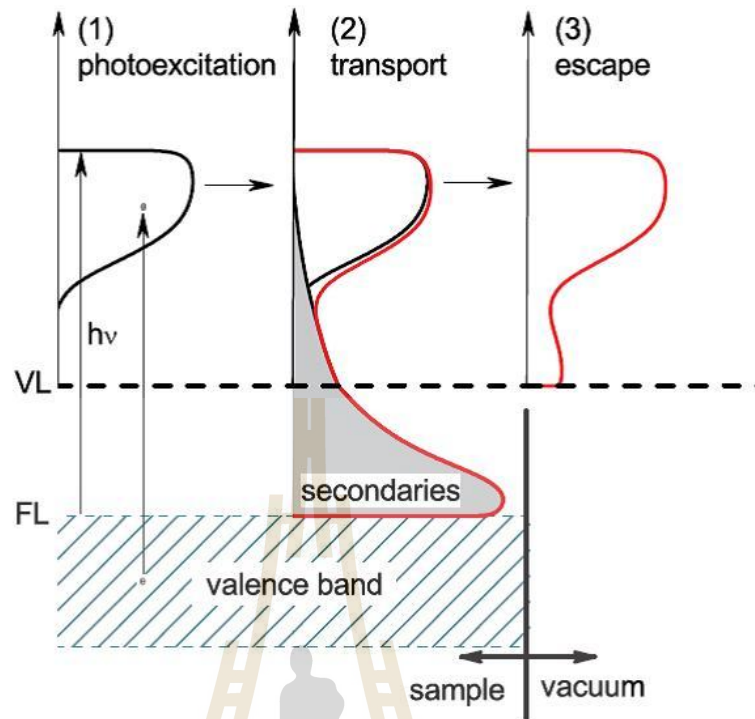
**Figure 3.3**    The three-step model for photoemission: (1) excitation of the electron, (2) electron travel to the surface, and (3) finally escapement (Hüfner *et al.*, 2005)

Generally, PES spectra are measured inside the spectrometer as demonstrated in Figure 3.4. When the sample is electrically contracted with the spectrometer. The Fermi level of the sample and the spectrometer align to be equal. The initial kinetic energy $E_{kin}^{'}$ at the surface of the sample can be written in term of the electron kinetic energy $E_{kin}$ in the spectrometer

$$E_{kin} = E_{kin}^{'} + \Phi_s - \Phi_{spec} \tag{3.5}$$

Where $\Phi_{spec}$ is the WF of the spectrometer. The measured value is the kinetic energy of the electron inside the spectrometer becomes.

$$E_{kin}^{'} = hv - E_B - \Phi_{spec} \tag{3.6}$$
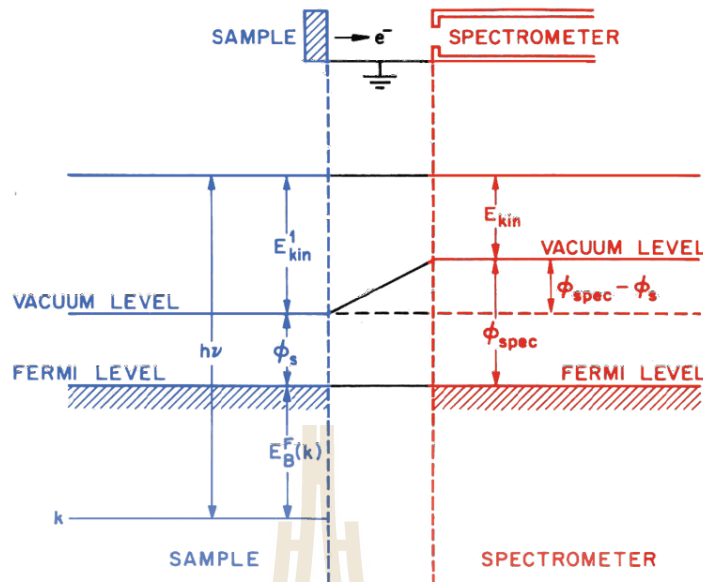
**Figure 3.4**    Schematic energy level diagram for a sample is in electric equilibrium

with the spectrometer (Fadley, 1978).

In addition, the kinetic energy of photoelectron can also be emitted as a

function of emission angle $(\theta, \emptyset)$, the electron spin orientation $(\sigma)$, or the photon-

energy or polarization, the basic process is illustrated in Figure 3.5. These momentum

of the photoelectrons can also be measured in addition to the kinetic energy $(E_{kin})$

band structure of the single crystal material. Angle-resolved photoemission

spectroscopy (ARPES) provides information about the electron structure of crystals

and the energy band dispersion can then be obtained as equation follows;

$$E_{kin} = \frac{p^2}{2m},  \qquad (3.7)$$

$$p = |\vec{p}| = \sqrt{2mE_{kin}}  \qquad (3.8)$$

Where the relation between energy and momentum $(\vec{p})$ can be obtained from the

emission angle $(\theta, \emptyset)$, which the components of parallel $(p_{\parallel})$ and perpendicular $(p_{\perp})$ to

the surface.
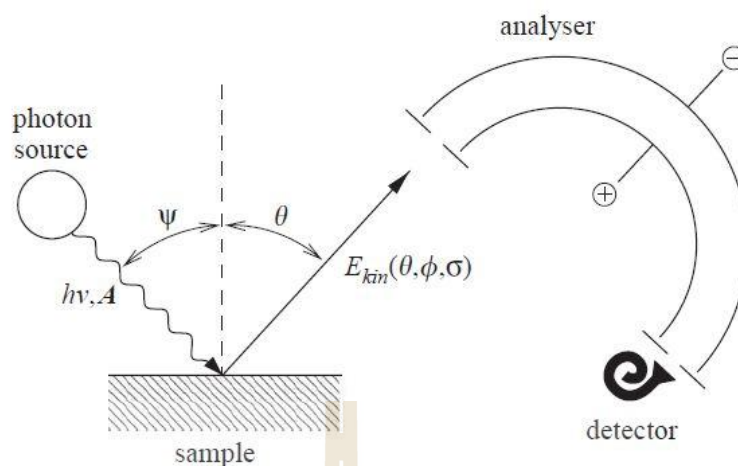
**Figure 3.5** The modern diagram of PES experiment. (Hüfner *et al.*, 2005)

Figure 3.5 is a diagram of PES experiment indicating technical basis of the experiment consisting of main components for performing PES measurements. This consists of a photon source, a sample and an electron energy analyzer. The equipment is in ultrahigh vacuum (UHV). UHV will be discussed in more details in the next section.

### 3.1.1 X-ray Photoelectron Spectroscopy (XPS)

Photoelectron spectroscopy for chemical analysis is often known as X-ray photoelectron spectroscopy (XPS). XPS is capable of probing the core-level electrons, whose binding energies depend on the elements from which the photoelectrons originate. The binding energy of a specific element will be affected by chemical state and electronic state of the elements within a material. Both composition and the chemical state of surface constituents may be determined by XPS. An example spectrum of binding energies are characteristic for specific electron orbitals in specific

atoms that can be seen in Figure 3.6. The atomic shell from which the electrons are ejected label as O1s, C1s, In3d and Sn3d.
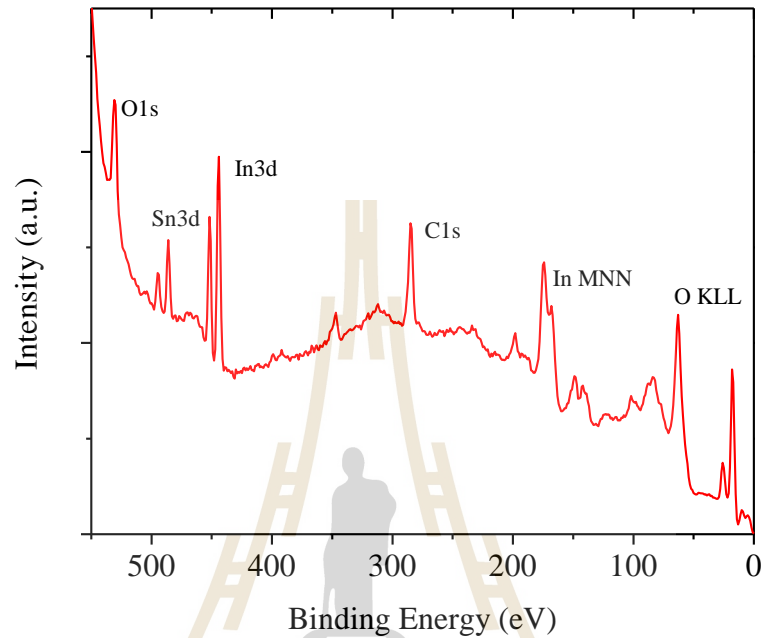


**Figure 3.6**     Example of an XPS spectrum taken from a ITO thin film.

In addition to photoelectrons, Auger electrons may also be generated during the decay process. The Auger electron emission was described by an empty core electron hole (an electronic level with a missing electron), an electron from a higher energy level may fall into the empty level and fill that hole. The created core-hole can be filled by several processes that are schematically shown in Figure 3.7. The consequence is that a hole now exists in the higher energy level. This hole may de-excite itself by imparting energy to another electron in an electronic level with similar binding energy. When this happens, the excess energy can either be emitted as a photon (fluorescent decay) or can cause an Auger decay. Because of this dependence upon three energy levels, the Auger electron peaks are broader than the photoelectron

peaks in a spectrum of electrons emitted from a material when it is irradiated by x-rays. Auger electrons therefore have a constant kinetic energy when varying the photon energy, while photoelectrons have a constant binding energy (Briggs and Seah, 1990).

Further, the more detailed XPS analysis involves the studies of small chemical shifts. The binding energies of the core-level electrons are very sensitive to any changes in the chemical environment. Such changes can be revealed by small chemical shift of the core-level peaks for a given element.
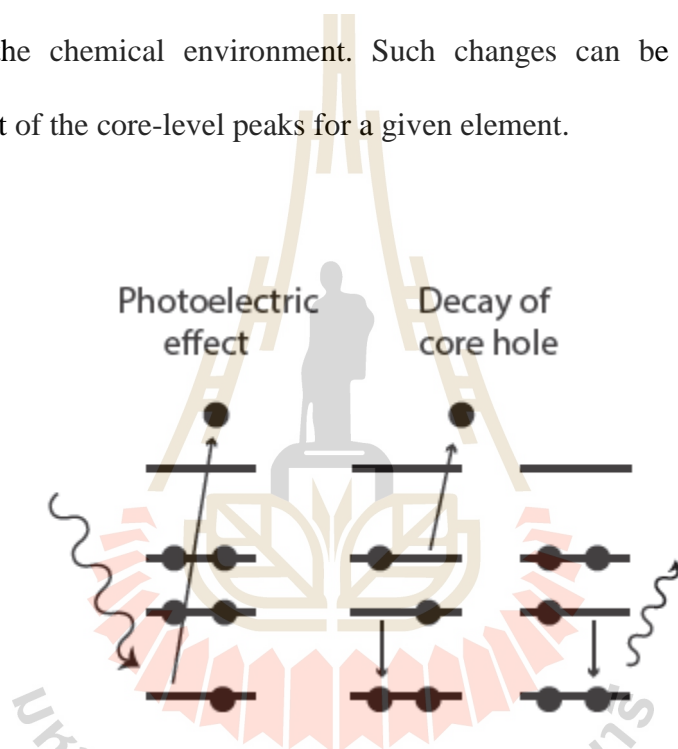


**Figure 3.7** Schematic diagram of the AES process in basic steps, fluorescent decay, and Auger decay (Briggs and Seah, 1990).

### 3.1.1.1 Chemical shift

Chemical shift is dependable on the oxidation state and chemical environment of the atoms (such as oxidation state, electro-negativity of neighboring atoms, number of surrounding atoms). In this sense, a major advantage of the Gelius model is that it allows the binding energy difference, $\Delta E_{A,B}$ , of a particular core-level

c for a given element in two different chemical environments, A and B. In consideration of the first order approximation, the energy of an electron in a core-level depends on the Coulomb interaction between core electron and nucleus screened by valence electron charge. A change in a particular atom will cause a spatial rearrangement of the charges, thus the potential around the atom was described by follows

$$\Delta E_{A,B} \; = \; K_c(q_A - q_B) + (V_A - V_B) \tag{3.9}$$

is become

$$\Delta E_{A,B} \; = \; K_c q_i + \sum_{j \neq 1}(q_j / r_{ij}) \tag{3.10}$$

The first term describes the difference in the electron-electron interaction between core orbital c and the valence charges $q_A$ and $q_B$, respectively. $K_c$ is the coupling constant between core and valence electrons and $q_i$ charge on atom i.

The second term has the character of a Madelung potential (approximation), where the sum is over potentials arising from all the other ionic charges $q_j$ centered at positions $r_{ij}$ relative to the atom i in the material. This equation is on the order of 10 eV. As a result, the observed chemical shifts in solids are usually on the order of a few eV or less.

### 3.1.1.2 Spin-orbit splitting

When an electron with relativistic velocity moves in an electrical field, it will experience an effective magnetic field. The magnetic moment of the electron, can couple to this magnetic field, causing a perturbation of the energy levels of the atom. Spin-orbit splitting is also observed in the spectra and it may be considered as a final state effect, which appears for all core levels besides s-subshells. It arises from a

magnetic interaction between spin of the electron (up or down) and its orbital angular momentum. Most obviously 3p and 3d, the spectrum shows that emission does not give rise to a single photoemission peak, but a closely spaced doublet as follow this equation

$$j = l \pm s \tag{3.11}$$

when $j$ is define the total angular momentum, $l$ is angular momentum and the electrons' magnetic moment is proportional to the spin $s$.

Figure 3.8 show the In 3d core level in ITO thin film. It becomes more obvious if the spectrum was expanded in the region of the 3d emission. For example, a d-orbital can be either $d_{3/2}$ or $d_{5/2}$. The intensity ratio of the two spin-orbit components is dictated by the ratio of there spective multiplicities as:

$$g = 2j + 1 \tag{3.12}$$

For example, the ratio of the degeneracy of $In3d_{3/2}$ and $In_{5/2}$ is 4:6, $In2p_{1/2}$ and $In2p_{3/2}$ is 2:4.
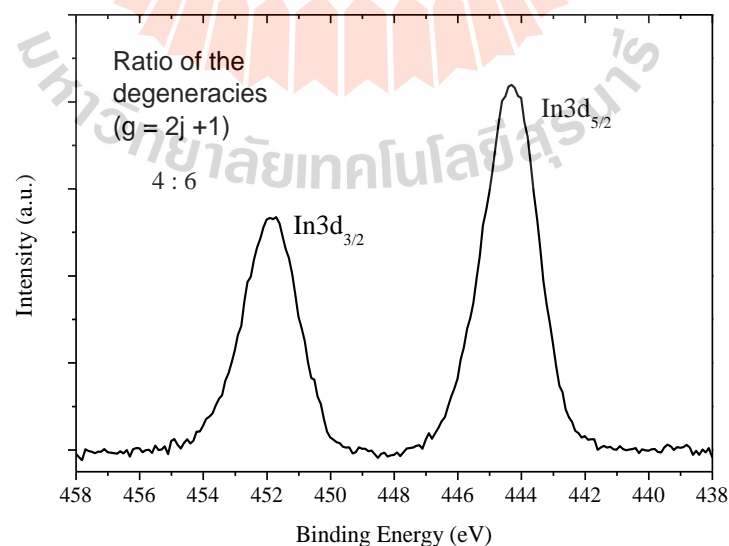


**Figure 3.8**    Spin-orbit coupling leads to a splitting of the 3d photoemission of Indium into a doublet.

### 3.1.2    Ultraviolet Photoelectron Spectroscopy (UPS)

Although in principle, XPS can also be used to investigate the electronic structure of the valence region of a solid (Figure 3.6 the spectrum can also be covered the valence region). But the most severe problem is that the photoionization cross section for the valence electrons is much lower than that of the core electrons, when using high photon energy for the excitation. The structure in the valence band is best achieved at lower photon energies because of both the superior energy and momentum resolution, which has a high cross section for the electrons in the valence region. This technique is common to study the electronic structure of the valence region using ultraviolet light known as UPS.

Figure 3.9 shows an UPS spectrum of a ITO thin film. This energy is measured with respect to the Fermi energy at $E_F = 0$ eV. The Fermi level of the whole system should be aligned under the thermal equilibrium conditions when all parts are in electrical contact. It is important to note here that the Fermi level position obtained from the metallic (using Fermi edge of gold) surface remains fixed and can be used for semiconducting samples. It is clearly shown that the binding energy is located about 18 and 26 eV it is the structure 4d band for In and Sn, respectively.

In additional, UPS has been extensively used to study the energy level alignment at the interfaces. The energies of several important molecular levels can be directly obtained from the UPS spectrum by simple analysis, including the vacuum level, the low cutoff energy, the Fermi level and the HOMO or valence band maximum. This part will be discussed in more details in the next section.
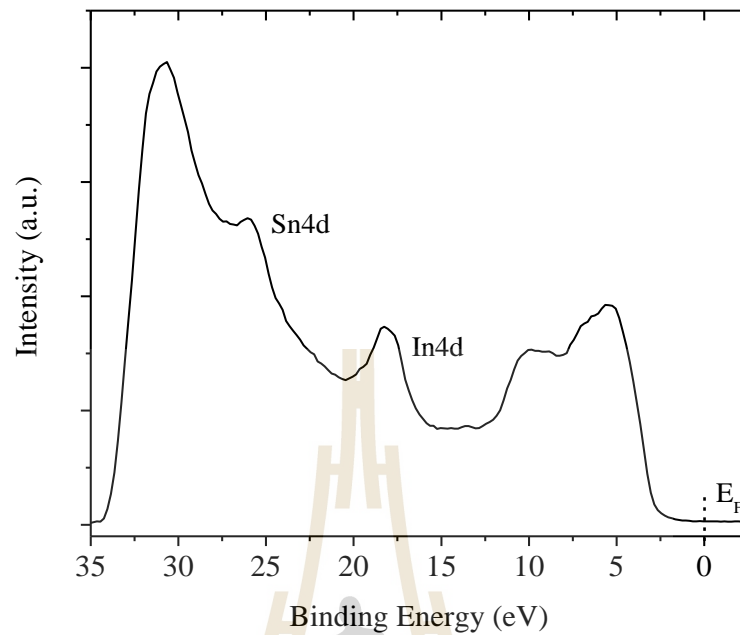
**Figure 3.9**    Example of an UPS spectrum measured from an ITO thin film.

## 3.2    Inelastic mean free path (IMFP) and surface sensitivity

The inelastic mean free path (IMFT or λ) of an electron travelling within a solid can be defined as the average distance of an electron without losing its energy by inelastic scattering. The IMFP is not only dependent on the material structure but is also on the kinetic energy of the photoelectrons emitted. Figure 3.10 shows the mean free path of electron as a function of the electron kinetic energy. It can be seen that the minimum of IMFP about 2-5 Å at kinetic energy of 50-100 eV (range of UPS). The kinetic energy between 100-1000 eV (range of XPS), the IMFP is increase up to 20 Å. This means that the escape depth of electron with energy of about 10-1000 eV in solids is rather short, and thus photoemission technique is a very surface

sensitive technique because only electrons from the top few atomic layers can escape without loss of energy.
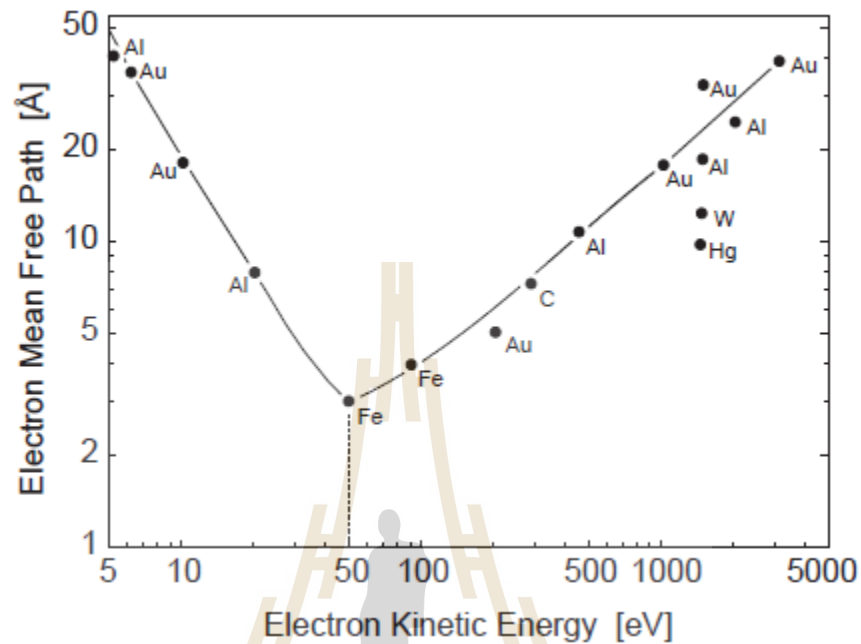


**Figure 3.10**    The mean free path of electron as a function of the electron kinetic energy (Hüfner *et al.*, 2005).

The IMFP is actually defined by the following equation which gives the probability of the electron travelling a distance, $d$, is given by

$$P_{(d)} = \exp\left(-d/\lambda\right) \tag{3.13}$$

where $\lambda$ is the IMFP for the photoelectron with kinetic energy $E_k$. The probability for an electron from a depth $d$ to escape without inelastic scattering $P(d)$, is shown as a graph in Figure 3.11. Figure 3.11 shows a graph of the probability that a photoelectron is emitted to vacuum without being inelastically scattered as a function of depth, its probability decays exponentially to zero for a distance $d > 5\lambda$. For $\theta = 90°$, $1\lambda$ corresponds to 63% of elastically emitted photoelectrons, $2\lambda$ to 86% and $3\lambda$ to

95%. It means that the electrons (>95%) detected mainly are from the depth within $3\lambda$ of the surface.
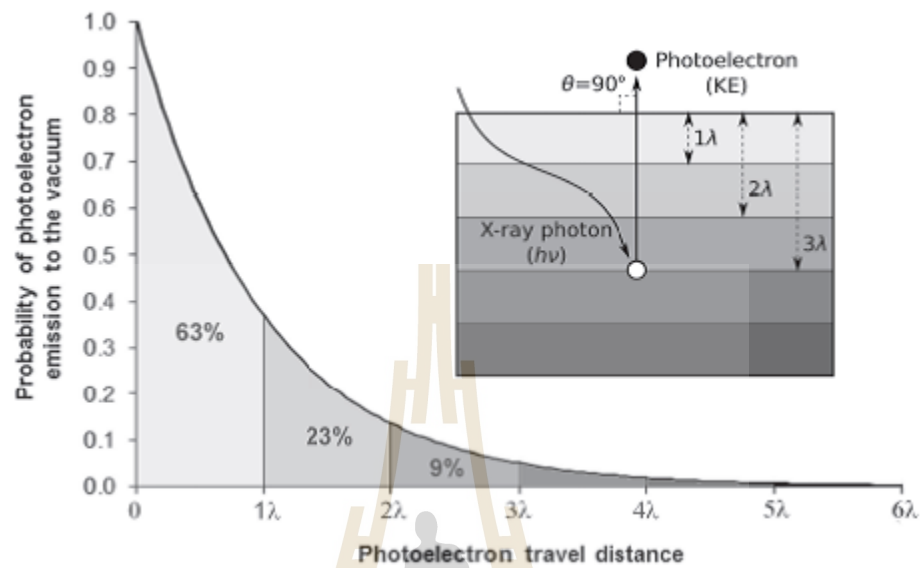


**Figure 3.11** Schematic picture of the probability that a photoelectron is emitted to vacuum without being inelastically scattered as a function of travel distance of photoelectron in solids (Hüfner *et al.*, 2005).

For flat and homogenous samples, the surface sensitivity can also be used to determine the thickness of surface film. The intensity from the substrate decreases exponentially due to inelastic scattering process of photoelectrons with the increased thickness of upper layer, as shown in equation

$$I_d = I_0 \exp\left(-d/\lambda\right) \tag{3.14}$$

where, $I_0$ is the intensity from depth $d$ in the substrate, $I_d$ is the intensity form the over-layer at the surface and $\lambda$ is the IMFP.

For quantitative consideration, the core levels of each element can be used to gives the surface information on the chemical state of the composition (Lee and

Flynn, 2006). This expression may be used for all homogenous samples. The atomic concentration ($C_x$) of element can be determined from the following equation.

$$C_x = \frac{n_x}{\sum_i n_i} = \frac{I_x/S_x}{\sum_i I_i/S_i} \qquad (3.15)$$

Where $I_x$ is the relative peak area of photoelectrons from element x, $n_x$ is the number of atoms of the element x per volume area of the surface, $S_x$ is the atomic sensitivity factor that depends on the probability to detect the photoelectron and a particular photoemission event to occur.

Finally, the other important aspect about PES measurement is its surface sensitivity. PES turns out to be one of the best surface analytical tools. This limitation is governed by the fact that photoelectrons emitted from the greater depths suffer energy loss by inelastic scattering processes, leading to a relatively short escape depth and IMFP extending ~30-50 Å maximum.

## 3.3    Ultrahigh vacuum (UHV)

In order to detect the photoelectrons that escape from the surface of solids, PES experiments require a high vacuum condition because of the IMFP of photoelectrons needs to be travel longer than distance the sample surface and analyzer without intermediate collisions.

Vacuum technology is the science of the removal of all (or nearly all) gases from a chamber, the measurement and manipulation of the vacuum environment. The definition of vacuum is related to molecular density, mean free path and the time constant to form a monolayer (Weston, 2013). The levels of vacuum can be classified into 3 regions as shown in Figure 3.12. Those ranges are separated at the pressure in

the range of $10^{-3}$ Torr and $10^{-7}$ Torr with the molecule density in the range of $4\times10^{13}$ and $4\times10^9$ molecule/cm$^3$, respectively. As there are lots of molecules even in vacuum, ultrahigh vacuum (UHV) is the vacuum regime characterised by pressures lower than about $10^{-7}$ Pa or 100 nanoPa (below $10^{-9}$ mbar, $\sim10^{-9}$ Torr). There are several units used for measuring vacuum pressure. The conversion from the most common unit, Torr (or millimeters of mercury, mmHg) and others units, i.e., Pascal (SI unit, 1 Pa = 1 N/m$^2$) and mbar (1 mbar = 100 Pa) is

$$
\begin{aligned}
1 \text{ mbar} &= 100 && \text{Pa}, \\
1 \text{ mbar} &= 1 && \text{Torr} \\
1 \text{ Pa} &= 7.5\times10^{-3} && \text{Torr}, \\
1 \text{ Torr} &= 1.33 && \text{mbar}, \\
&= 133 && \text{Pa}.
\end{aligned}
$$
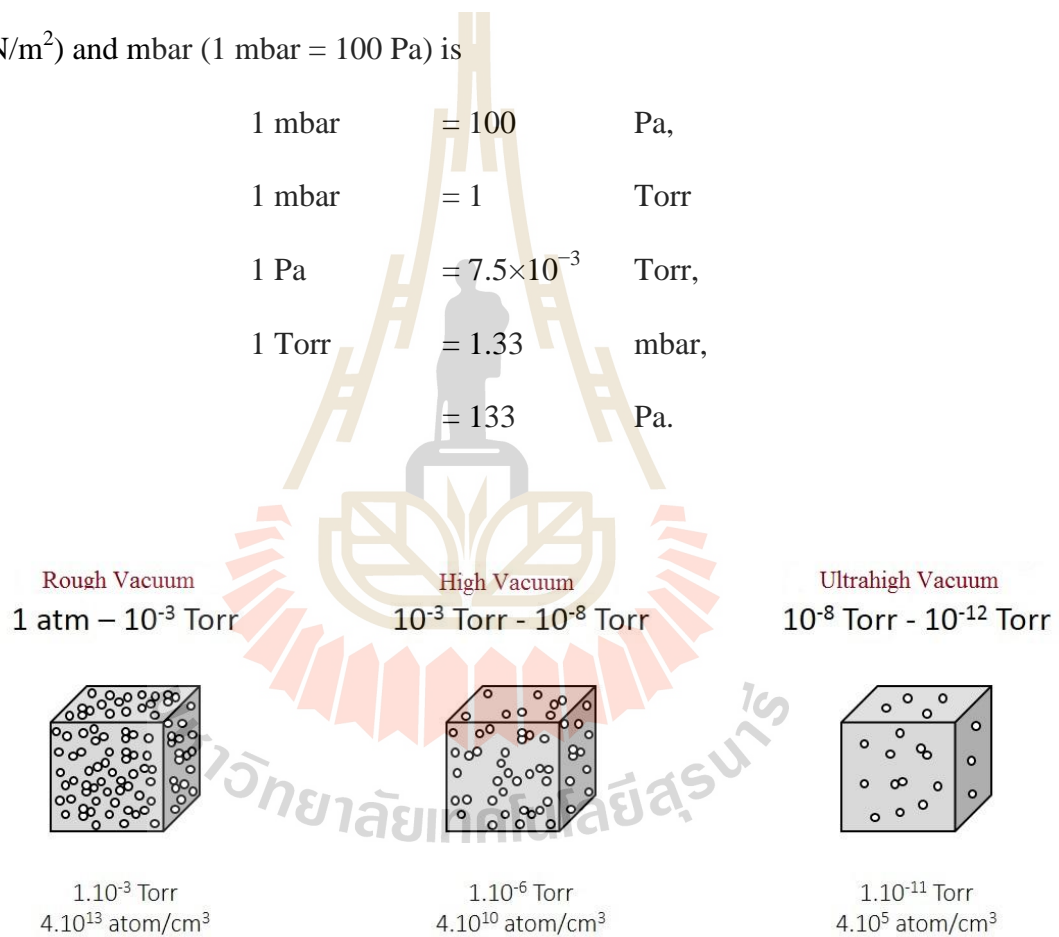


**Figure 3.12** Vacuum particle density comparison schematic (Weston, 2013).

### 3.3.1 The kinetic theory of a vacuum.

A vacuum environment is gas at reduced pressure and thus any theory of vacuum must account for laws which have been shown by

$$PV = nk_BT \tag{3.16}$$

where $P$ is the pressure, $V$ is the volume, $n$ is the molecular density, $T$ is the temperature and $k_B$ is Boltzmann's constant. Thus one obtains the rate of incidence of molecules ($I$) on the surface when $m$ is mass of a molecule follow by

$$I = \frac{P}{\sqrt{2\pi mk_BT}} \tag{3.17}$$

To investigate the physical properties of gas in terms of the motions of the molecules, we are to consider "mean free path" of all the molecules under the same conditions of temperature and pressure. The mean free path between molecular collisions in the gas phase can be defined in equation follow

$$\lambda = \frac{1}{n\pi d^2\sqrt{2}} \tag{3.18}$$

where $d$ is the diameter of the sphere representing the molecule. As the pressure or density of the gas is reduced, the mean free path increases.

Table 3.1 is the example case of nitrogen molecule at room temperature (T = 293 K) to illustrate how their values vary with the pressure. It can be seen that a time constant to form a monolayer during experiments in UHV condition is important to keep in mind because only low pressure can maintain a clean surface long enough to perform the experiments. When $n_0$ is the number of atoms in a monolayer, the "time constant" to form a monolayer can be written as

$$\tau = \frac{n_0}{I} \tag{3.19}$$

In general, a monolayer can be formed in the order of one or two seconds under the pressure of $10^{-6}$ Torr as there are lots of molecules even in vacuum. Therefore, detailed surface studies require a highly controlled environment with a pressure in the range of $10^{-10}$ Torr, in order to ensure the surface cleanness throughout the reasonable measurement time (few hours) and exclude any possible interactions between the adsorption and the sample surface.

Normally for safety of the experiment, PES experiments require the base pressure is about $1\times10^{-6}$ Torr. However, the pressure must be below $1\times10^{-9}$ Torr (ultrahigh vacuum) to protect the surface without contamination during the measurement. UHV conditions are necessary because only low pressure can maintain a clean surface (Briggs and Seah, 1990).
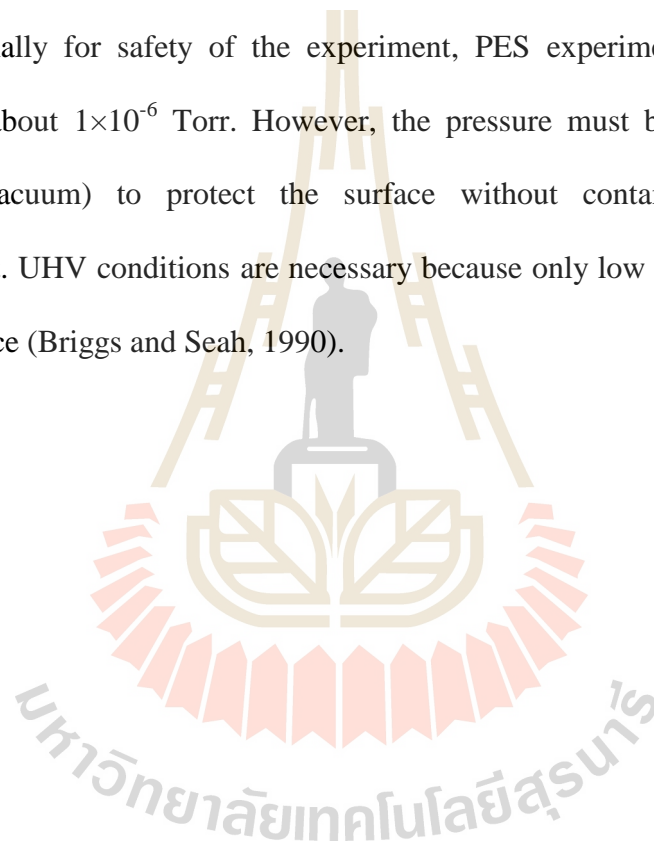
**Table 3.1**   Molecular density $n$, rate of incidence of molecular $I$, mean free path $\lambda$, and the time constant $\tau$ to form a monolayer for $N_2$ at room temperature by assumed the sticking coefficient to be unity. Defined the density of one monatomic layer $n_0 = 10^{15}$ cm$^{-2}$ (Weston, 2013).

| Pressure (Torr) | Molecular density, n (cm$^{-3}$) | Number of molecules incident I (cm$^{-2}$s$^{-1}$) | Mean free path, $\lambda$ | Monolayer to form time, $\tau$ |
|---|---|---|---|---|
| 760 | $2 \times 10^{19}$ | $3 \times 10^{23}$ | 700 Å | 3 ns |
| 1 | $3 \times 10^{16}$ | $4 \times 10^{20}$ | 50 $\mu m$ | 2 $\mu s$ |
| $10^{-3}$ | $3 \times 10^{13}$ | $4 \times 10^{17}$ | 5 cm | 2 ms |
| $10^{-6}$ | $3 \times 10^{10}$ | $4 \times 10^{14}$ | 50 m | 2 s |
| $10^{-9}$ | $3 \times 10^{7}$ | $4 \times 10^{11}$ | 50 km | 37 min |
| $10^{-12}$ | $3 \times 10^{4}$ | $4 \times 10^{8}$ | 50000 km | 25.5 days |

### 3.4    Hemispherical electron energy analyzer

A schematic diagram of a hemispherical electron energy analyzer is shown in Figure 3.13. Hemispherical analyzers are most initially used for PES system (Fadley, 1978). The idea of the analyzer is to let the photoelectron pass between the two hemispherical surfaces of inner radius $R_1$ and out radius $R_2$ which is maintained at a potential applied electric field via the application of suitable voltages to the hemispheres and a micro-channel plate (MCP) detector at the end of the trajectory. The inner sphere is held at a positive potential while the outer spheres is negative. The entrance and exit slit lie on the medium radius $R_0$. The energy resolution of this analyzer can be simply described in an equation below

$$\Delta E = E_{pass} \left[ \frac{w}{2R_0} + \frac{\alpha^2}{4} \right] \tag{3.20}$$

where, $E_{pass}$ is a pass energy, $w$ is slit width, $\alpha$ is acceptance angle. The pass energy is a function of potential difference applied in between the inner and outer spheres. From the equation, the resolution depends on diameter of the analyzer; the larger diameter is higher resolution. The smaller pass energy results in the higher energy resolution as well. However, the pass energy is set to a specific value during the measurement, the acceptance angle is also to achieve the high resolution. The energy scan is obtained by varying the retardation voltage in front of the entrance slit.
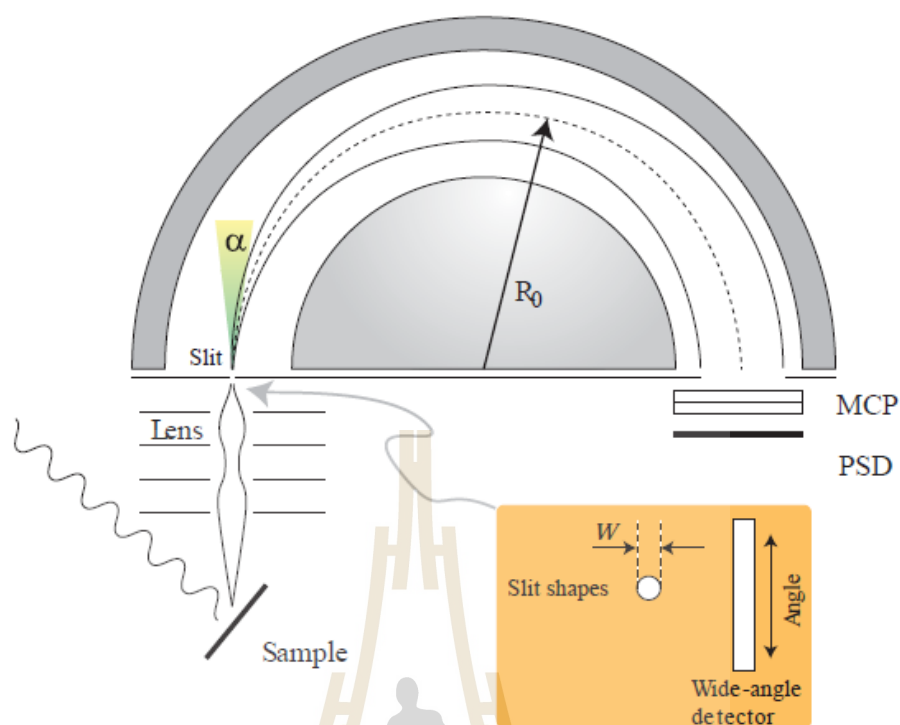
**Figure 3.13** A schematic diagram of the hemispherical electron energy analyzer.

## 3.5 Photon source

In PES experiments, photons with various energies are used as for excitation. Thus, PES can be categorized into several classes, according to the light source used to generate photoelectrons. The common light sources include x-ray, ultraviolet and synchrotron radiation. The field of photoelectron spectroscopy can be divided in two regions depending on the type of photon source used.

For the investigation of core-level states, called X-ray photoemission spectroscopy (XPS). The X-ray gun thermally emitted electrons are accelerated toward anode. The principle of X-ray generation is the following: a tungsten filament (cathode) is heated up and produces electrons by thermionic emission. When the

electron hit the anode, they create holes in the core of the anode material, resulting in de-excitation from higher energy levels and hence emission of X-ray radiation. The most X-ray sources are from Al and Mg anode tubes emitting Al $K_\alpha$ and Mg $K_\alpha$ radiation at 1486.6 eV and 1253.6 eV, respectively. The illustration of X-ray gun is shown in Figure 3.14.

For the investigation of valence band states, called ultraviolet photoemission spectroscopy (UPS). Helium discharge lamb is usually used as a light source contain helium gas kept in an enclosure and when applying an electric field the gas becomes ionized. Upon relaxation of ionized (exited) atoms in the gas which emits He I and He II radiation of energy 21.23 eV and 40.82 eV, respectively, (Barr, 1994; Hüfner, 2003).

Recently, in order to improve the energy and spatial resolution, the x-ray source can be further monochromatized through specially-designed quartz crystal. X-ray radiation are then monochromatized and focused on the sample using quartz crystal monochromator in a specific geometry as shown in Figure 3.15. The large surface area of the crystals define a large solid angle and hence a high X-ray flux. The crystals are also optimized for high energy resolution.

However, Synchrotron light sources provide great flexibility for photon energy because of the energy of Synchrotron light typically covers a large range of the photon energy continuously from UV to soft X-ray or hard X-ray region. The energy of the photon can be tuned to suit a specific PES experiment. Other characteristics of synchrotron radiation include high photon flux, brilliance (brightness) and polarized light.
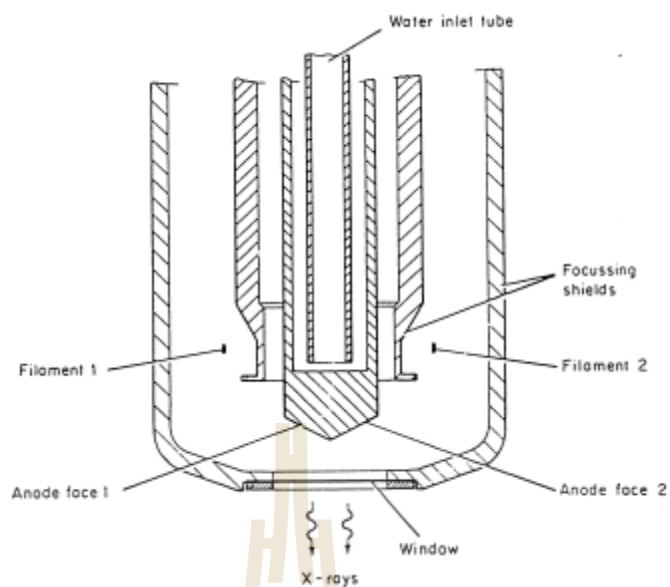
**Figure 3.14** Illustration of X-ray gun using Al and Mg anode tubes emitting Al $K_\alpha$

and Mg $K_\alpha$ radiation (Hofmann, 2012).
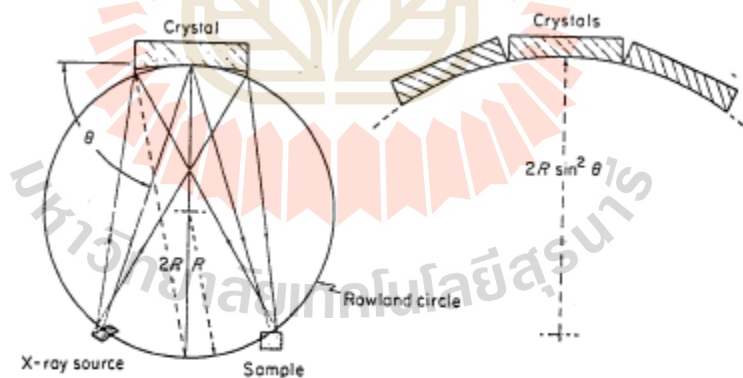


**Figure 3.15** Illustration of the modern of X-ray monochromatized using quartz

crystal (Hofmann, 2012).

### 3.5.1 Synchrotron light

Synchrotron light is the radiation emitted by a charge particle moving in a circular motion with the speed close to the speed of light, as shown in Figure 3.16. Most synchrotron light sources use an electron as the charge particle. The moving electrons pass to the bending magnets, undulators and wigglers. Under changed direction by the Lorentz force, the electrons lose energy by emission of electromagnetic radiation which is the synchrotron light. The synchrotron light is delivered pass through the beamline to experimental station which selected the photon energy by a monochromator (Duke, 2008).

In general, the salient properties of synchrotron radiation are summarized below:

- Continuous spectrum: wide tunability in photon energy or wavelength is cover from the infrared to X-rays.

- High brilliance and high flux: many orders of magnitude higher than that with the conventional X-ray tubes.

- Highly collimated: a small radiation angular divergence angle inversely proportions to electron beam energy (1/gamma).

- High level of polarizations: both linear and circular or elliptical.
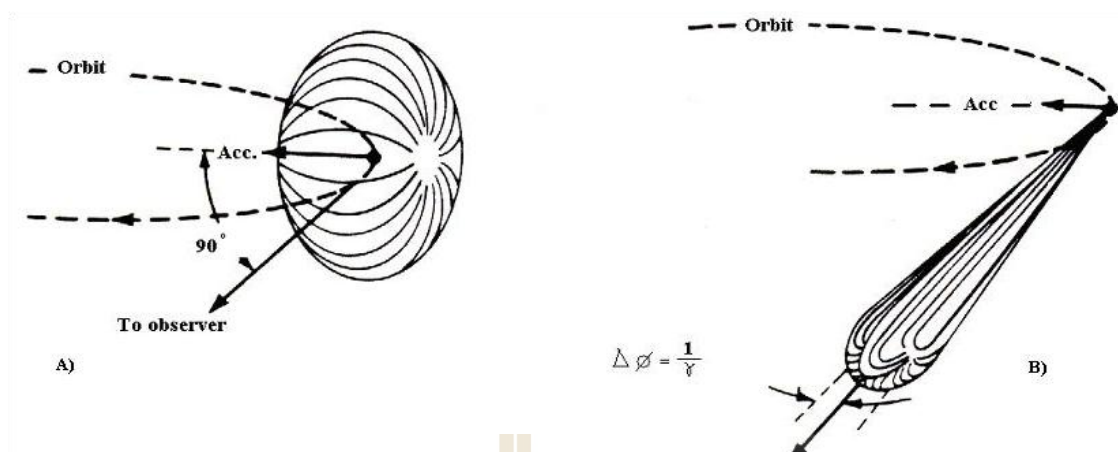
**Figure 3.16**    Angular distributions of radiation emitted by a charged particle moving

along a circular orbit with (a) in the electron's frame and (b) after

transformation into the lab frame. In the last case the light is called

"synchrotron radiation" (Winick and Doniach, 2012).

## 3.6    BL3.2Ua PES beamline

### 3.6.1    The Siam Photon Source

Synchrotron Light Research Institute (SLRI) is the first and only synchrotron

radiation research facility in Thailand (Kengkan *et al.*, 1998). The layout of the light

source of the SLRI is shown in Figure 3.17. The linear accelerator (LINAC) is used to

generate an electron accelerator of a 40 MeV. The 40 MeV electrons are transported

to the booster synchrotron (SYN) and accelerated to 1.2 GeV. Then, the electrons are

transported and stored in the storage ring (STR) (Pairsuwan, 2007; Songsiriritthigul *et

al.*, 2010).

There are many different techniques at SLRI that can be used to reveal

information of materials with atomic scale such as X-ray Absorption Spectroscopy

(XAS), X-ray Fluorescence (XRF), Small Angle X-ray Scattering (SAXS), Deep X-

ray Lithography (DXL), Macromolecular Crystallography (MX), Infra Red Spectroscopy (IR) and Photoemission Spectroscopy (PES).
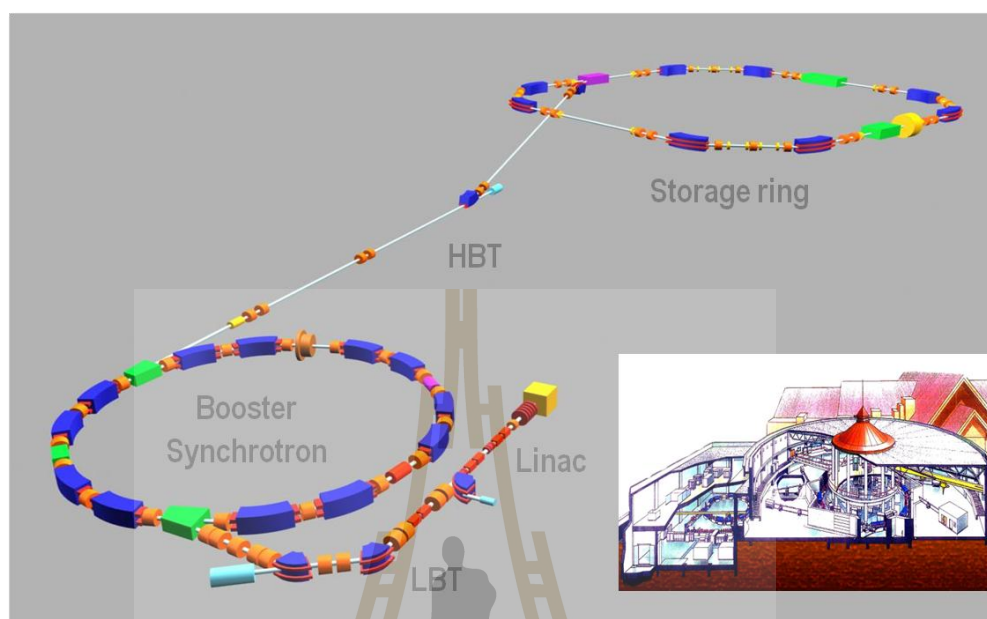


**Figure 3.17** Artistic impression of the light source at SLRI. The inset is the accelerator complex at SLRI.

The beamline 3 (BL3) consists of two branch lines for PEEM and PES experimental stations, as shown in Figure 3.18. This thesis work was carried out at the BL3.2Ua beamline. The BL3.2Ua employs a varied-line spacing plane grating monochromator and utilizes synchrotron light from the insertion device, namely an undulator. Photons with energy between 40-160 and 240-1040 eV can be delivered to a sample in the PES experimental station (Nakajima *et al.*, 2013; Songsiriritthigul *et al.*, 2001). The radiation is produced from the undulator which provides high flux of soft x-rays from coherent electron motions along the periodic magnets. The undulator radiation shows harmonic peaks in specific photon energies, the flux at a harmonic

peak is much higher than production from the bending magnet source as shown in Figure 3.19.
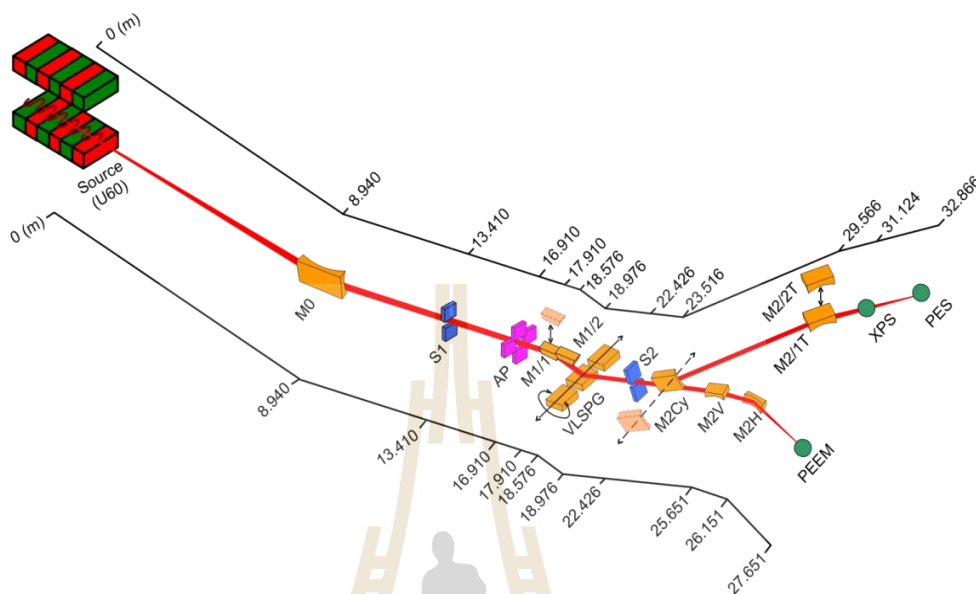


**Figure 3.18**    The optical layout of the BL3 beamline (Songsiriritthigul *et al.*, 2007).
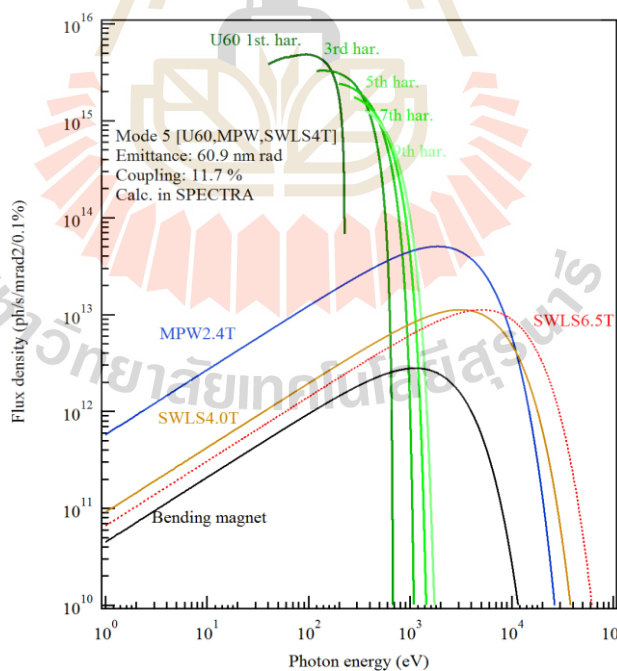


**Figure 3.19**    Calculated spectra of synchrotron light at SLRI generated from bending magnet, undulator, multipole wiggler and wavelength shifter magnet (Songsiriritthigul *et al.*, 2007).

The PES experimental station is equipped with the photoemission system with different sample preparation systems. The system is connected to the molecular beam epitaxial system (MBE) and a R2P2 radial transporter with a load lock chamber, as shown in Figure 3.20. The samples prepared in the preparation systems can be transferred to the PES analysis chamber via the linear and rotary sample transport systems, allowing various *in situ* experiments to be performed at BL3.2Ua. Two different electron energy analyzers are available at the BL3.2Ua; i.e. a 135-degree-sector CLAM2 analyzer is located in front of the PES station and a hemispherical SCIENTA R4000 analyzer is located the PES station (The hemispherical Alpha110 energy analyzer was also used for this work before R4000 setup). Both systems were supplied by the Thermo VG Scientific. The experimental station chamber is shown in Figure 3.21.

In addition, the analysis chamber is equipped with a hemispherical SCIENTA R4000 analyzer, Low-energy electron spectroscopy (LEED) is used for determining surface crystal structures of samples, a 5 kV electron gun is used for a surface sensitive Auger electron spectroscopy (AES) and Ar ion sputtering of 3 keV is used for ion bombardment on the surface.
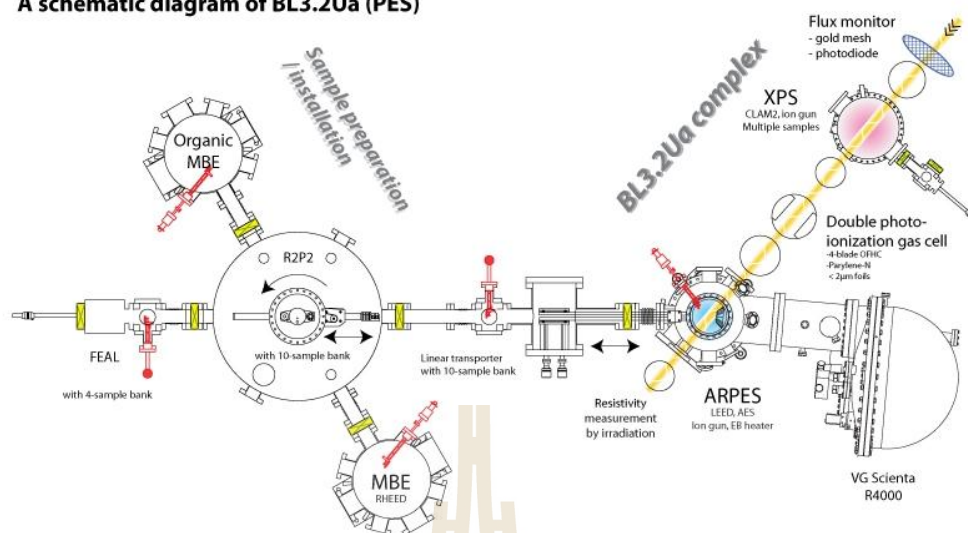
**Figure 3.20**    The schematic diagram of the PES experimental end station of BL3.2Ua.
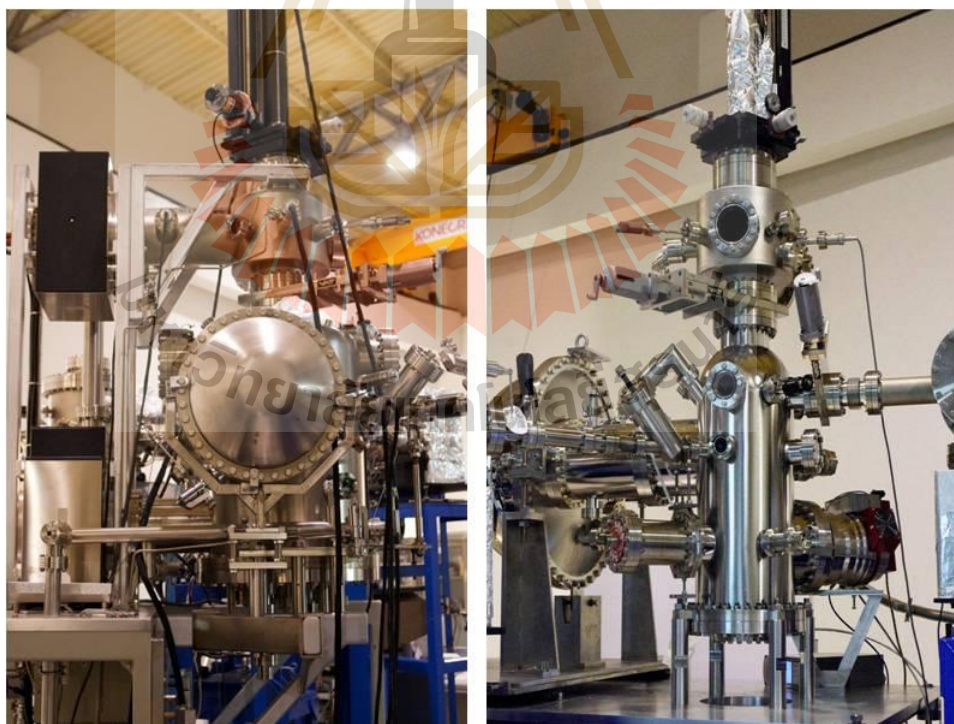


**Figure 3.21**    Experimental station at the BL3.2Ua with the Alpha110 analyzer and R4000 analyzer.

### 3.6.2 Alpha110 energy analyzer

The Alpla110 energy analyzer is a 180° hemispherical electron energy analyzer. The energy resolution can be selected by selecting the width of the entrance slit of the analyzer <5 meV, small area XPS capability down to 100μm and angle resolved XPS capability with an angular resolution of ±1°. The mean radius is 110 mm. It has a rather wide gap between the two hemispheres. The detector is a multi-channeltron array; it has 7 channeltrons. Figure 3.22 shows the analyzer cross-section and the position of the Alpha-plates. The electron-emitting angle is 50degrees with respect to the incoming beam of synchrotron light. The Alpha110 energy analyzer installed at the photoemission experimental station of BL3.2Ua is also shown in Figure 3.21.
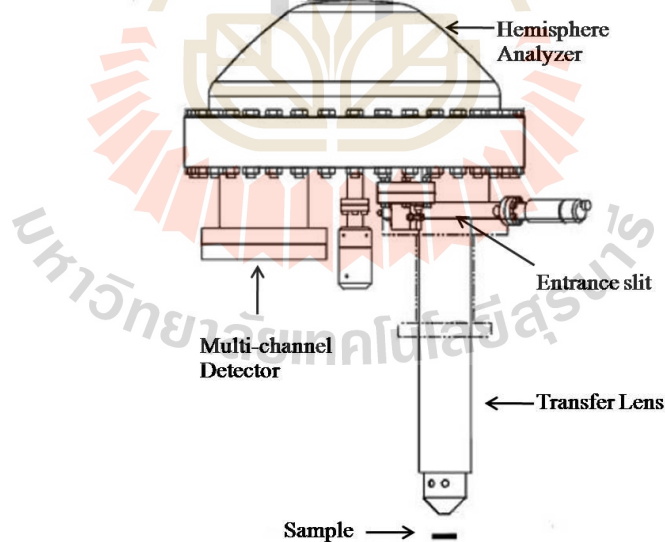


**Figure 3.22**    Side view of the Alpha110 analyzer.

### 3.6.3    SCIENTA R4000 energy analyzer

The SCIENTA R4000 energy analyzer is one of high-resolution hemispherical electron energy analyzers with a mean radius is 200 mm. It consists of the electron spectrometer supporting high voltage power supply cabinet and personal computer for instrument control, read-out and data management. The detector is a standard multichannel panel (MCP)/phosphor screen with a charge coupled device (CCD) camera.

One of the outstanding features of this analyzer is its high energy resolution that reaches the sub-meV region. Another unique feature of the R4000 analyzer lies in its 2-dimensional detection scheme that can measure the intensity of photoelectrons over a wide angle range simultaneously. The lens in R4000 can provide two different operation modes: transmission mode and angular mode that can be operated an acceptance angle of +/-15 degrees. This R4000 has an acceptance angle that can cover 30 degrees, 14 degrees and 7 degrees is particularly useful for covering large momentum space at the same time. The energy resolution of the analyzer is determined by pass energy and analyzer entrance slit. There are analyzer lens tables for 1, 2, 5, 10, 20, 100 and 200 eV pass energies, and 9 slits (straight and curved) from 0.1 to 4 mm. The analyzer is installed with the lens aligned 55 degree with respect to the optical axis of the synchrotron light, as shown in Figure 3.21.

### 3.6.4   Sample holder

The samples holders are made of tantalum. The sample is placed and hold by clip as shown in Figure 3.23. For insulating sample or substrate, carbon tape or aluminum sheet is need to allow the conductivity. The sample holder can be transferred from the load-lock chamber to the PES analysis chamber by mammal handing. Figure 3.23 shows the sample mounted on the sample holder in the analysis chamber.
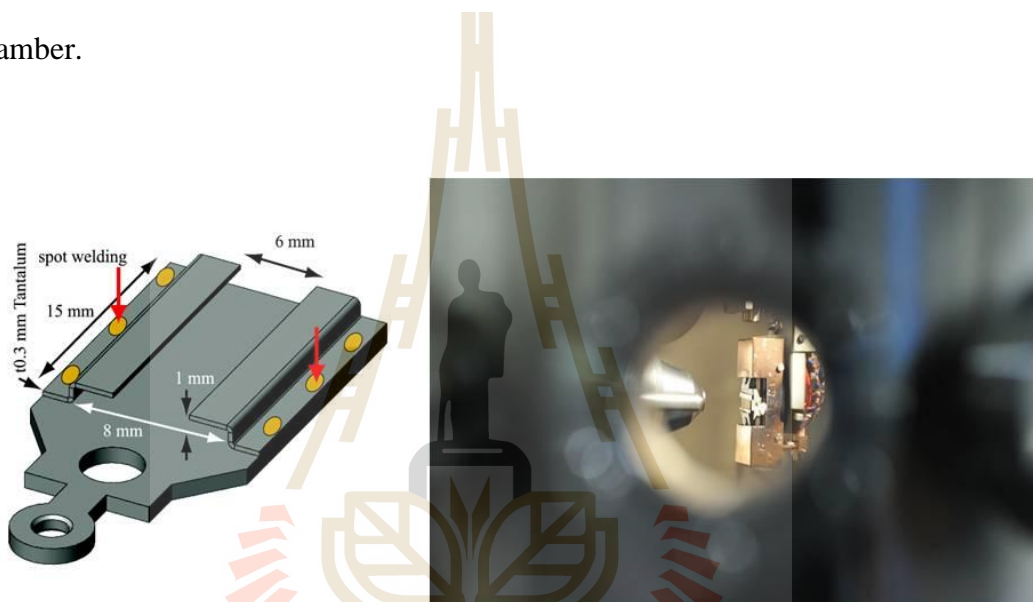


**Figure 3.23**    The sample holder used for PES measurements at the BL3.2Ua.

## 3.7   Determination of work function by PES

Figure 3.24 shows photoelectron spectra illustrating a method to determine a WF of solids. In the measurements, the sample was negatively biased. The negative bias push all secondary electron out from the surface of solids (Schlaf *et al.*, 2001). Thus the cut-off at low energy region of the photoelectron spectra can be easily observed. The WF of the sample $\Phi_s$ , can be determined from the following relation:

$$\Phi_s = hv - E_{cutoff} - E_F \qquad (3.21)$$

where $hv$ is the photon energy of the excitation, $E_F$ is the Fermi energy level and $E_{cutoff}$ is low kinetic energy cutoff (Grobosch, 2011). If the sample is semiconductor, the Fermi level may be determined from a photoelectron spectrum of metals. Normally the Fermi edge of gold is used to find $E_F$ when the sample is electrically contacted with the gold. The bias voltage of about -3 volts is good enough for measuring the WF of ITO.
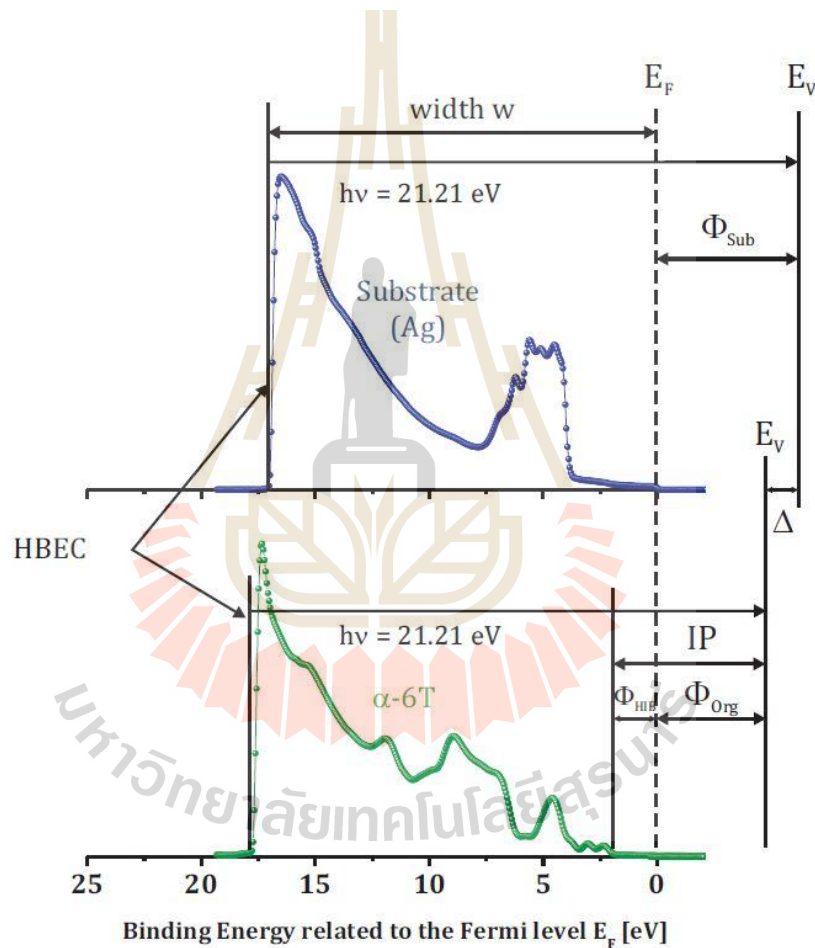


**Figure 3.24**    Schematic of UPS spectrum after apply negative bias voltage (Grobosch, 2011).

Figure 3.25 shows typical valence band spectra of ITO which were taken with the sample non bias and -3.2 V bias. The spectrum with the bias voltage to the

higher kinetic energy with high intensity and shape peak. The shift to high kinetic energy results in a high secondary electron background. Also shown inelastic cutoff and Fermi edge (refer to Au sample) are also shown. The relation between spectrum width, photon energy, and WF of the ITO sample is given in the following equation 3.21 (Park *et al.*, 1996).
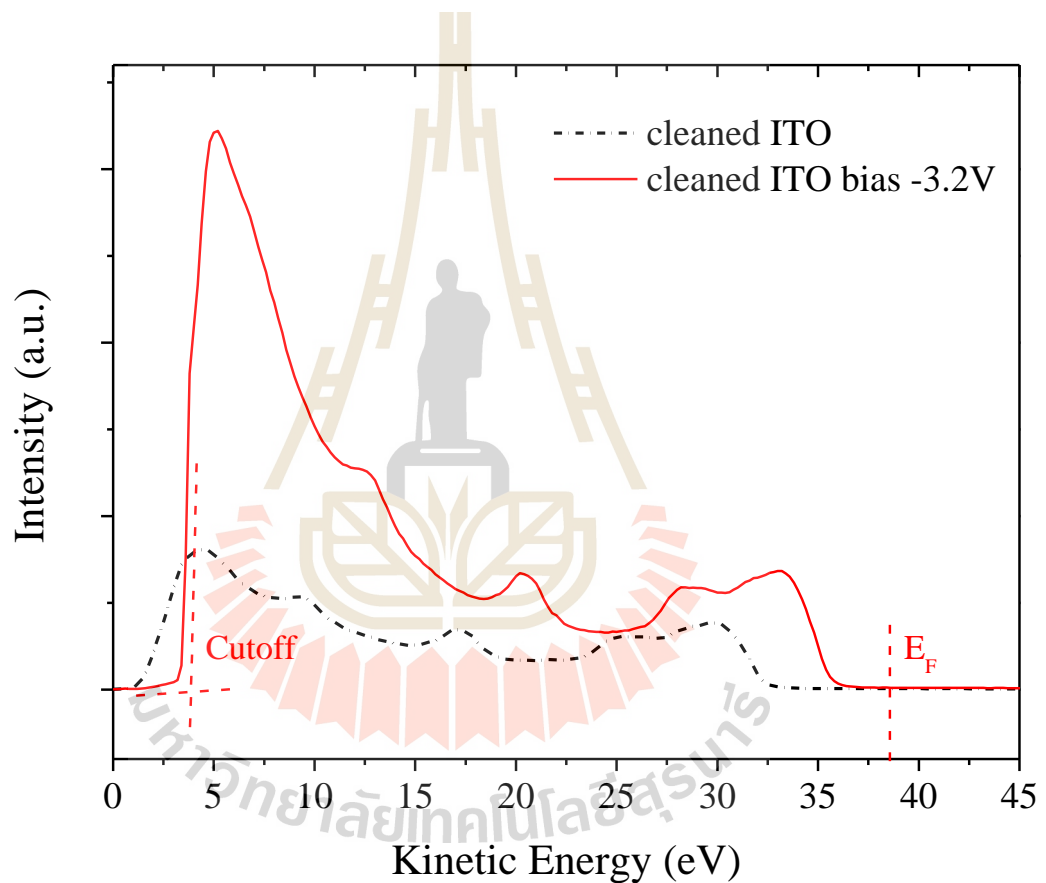


**Figure 3.25** Typical UPS spectra of ITO taken with normal spectrum and -3.2 V bias applied to the sample.

## 3.8 Photon fluence

Photon fluence is defined as the number of photons, $dN$, that enter an imaginary space of cross-sectional area $dA$, which is given as

$$\varphi = \frac{dN}{dA} \qquad (3.22)$$

According to the definition, the photon fluence can be calculated by the multiplication of the number of photons impacting to the unit area of the sample and the irradiation time.

$$\varphi = Dt \qquad (3.23)$$

where $D$ is photon flux density is number of incident photons per area in 1 second $(cm^{-2})$ and $t$ is the irradiation time (s).

### 3.8.1 Photon flux density

The photon flux is used to calculated the photon flux density ($D$) defined as

$$D = {^P}/_A \qquad (3.24)$$

Where $A$ is the exposed areas of the sample at the irradiation chamber and $P$ is the photon flux. In the measurement, the photon flux can be obtained as the photoelectrons per unit time per the quantum efficiency of the photodiodes.

$$P = \frac{I_s}{eQ_s} \qquad (3.25)$$

Where $e$ is the electric charges ($1.6 \times 10^{-19}$ C), $I_s$ is photodiodes current and $Q_s$ is the quantum efficiency of the photodiodes at a given photon energy. $Q_s$ also depends on the photon energy used.

### 3.8.2   Photon fluence at BL3.2Ua measurement

The photon flux ($P$) can be obtained by measuring the current of the photodiode ($I_s$). Figure 3.25 shows a set up for measuring the photon current in the real-time monitoring during PES. The gold mesh photocurrent ($I_p$) for monitoring the number of photons. The photon flux can be obtained based on $Q_s$, $I_s$ and $I_p$ as the follow.

$$P = \frac{I_s}{eQ_s} = \frac{I_p}{(0.65)eQ_g} \tag{3.26}$$

Where $Q_s$ is the quantum efficiency of the photodiodes and $Q_g$ is the quantum efficiency of the gold mesh. However, the beam cannot pass to the sample position if photodiode was used to monitor the number of photons. By the way, the quantum efficiency of photodiode is used to convert the generated the number of photons with known $I_p$ when the photons irradiate the sample and can be used $Q_g$ to determine the photon flux ($P$).
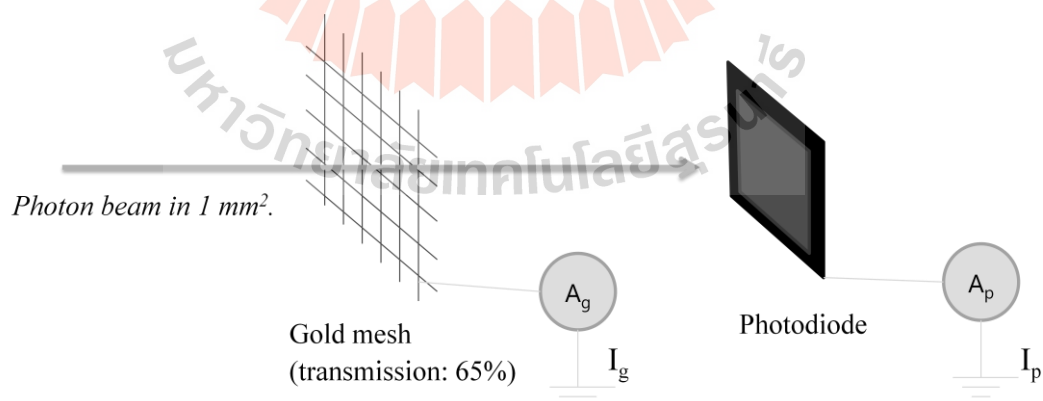


**Figure 3.26**   Set up for measuring the photon current.

## 3.9    Experimental parameters

**3.9.1 Synchrotron exposure experiments :** The WF changes of ITO surface caused by synchrotron was investigated by monochromatic VUV light and polychromatic light (zero-order light) were used for irradiation to observe the change of WF.

- VUV irradiation : It is a to revisit phenomena related to the reduction of the WF of ITO induced by UV irradiation (photon energy 21.21 eV). For explaining this effect, the ITO samples were exposed to the photons with energy of 40, 60 or 80 eV and repeatedly measured to obtain the WF (as a function of increasing the number of scan or exposure time). XPS was used to check in the surface chemical composition before and after irradiation.

- Zero-order light irradiation : This is for the investigations of the changes in WF of ITO induced by zero-order light. The samples were irradiated for 10, 20 and 30 minutes. XPS was performed to check the surface chemical composition before and after irradiation.

**3.9.2 Modification of the surface ITO experiments :**    The WF of ITO was investigated after the surface of ITO is modified by chlorine functionalized ITO, cesium-fluoride functionalized. Gas and oxygen exposures were also experimented.

- This experiment was to find out how external factors such as carbon contamination and Ar ion sputtering could affect the F, CsF and Cl functionalized ITO and also cleaned ITO. XPS was used to fine out the chemical composition of the treated ITO.

## 3.10 Sample preparation

The samples used in this work are ITO thin films deposited on glass slides. The samples were supplied by Nanocs Inc. The surface resistance is lower than 5 ohms/square and the optical transparency is more than 90%. The thickness of ITO film on a glass slide is about 60 nm. ITO samples were first cleaned by using chemical solvents following the process given below. Then cleaned ITO was surface treated with various treatment parameters such as cesium-fluoride functionalization ITO (CsF-ITO) and chlorination ITO (Cl-ITO). Finally, the samples is placed on the sample holder as shown in Figure 3.26.

### *Preparation of cleaned ITO (Note, 1995)*

There are two important steps which are used to clean the surface of ITO.

The first step is called standard wash for grease and solvent removal. The washing procedures can be summarized as follows:

- Immerse in boiling trichloroethylene (TCE) and acetone, each for about 1 minute.
- Ultrasonicate in isopropyl alcohol (2-propanol) for 1 minute.
- Wash with flowing DI water for 1 minute.
- Dry the sample in a high purity nitrogen stream.

The second one is for removing residual organic/ionic contaminations. The procedures are:

- Immerse in a (5:1:1) solution of $H_2O$ : $NH_4OH$ : $H_2O_2$ that is maintained at $75 - 80°C$ for 10 seconds.
- Immediately quench the solution under running DI water for 1 minute.

- Wash in DI water for 5 minutes.

- Dry the sample in a high purity nitrogen stream.

### *Preparation of chlorinated ITO*

ITO is cleaned by using chemical solvent, then its surface is modified using chlorine by following steps :

- Before chlorinated ITO preparation, the substrates were exposed to UV generated for an additional 3 min.

- ITO is dipped with o-dichlorobenzene (Aldrich) in a closed Pyrex Petri dish that is treated by UV treatment under air atmosphere which difference of time such for 2, 4, 6, 8 and 10 min.

- After treatment with UV radiation, the substrates were exposed to UV-generated for an additional 3 min to fully oxidize any residual chloro-carbon fragments on the surface.

- Finally the substrates were died using compressed $N_2$.

### *Preparation of Caesium-Fluoride ITO*

ITO is cleaned by using chemical solvent, then its surface is modified using Caesium-Fluoride by following steps :

- CsF was dissolved in DI water at different concentrations and was then spin coated onto the substrates at 5000 rpm for 30 s. CsF concentrations of 0.04, 0.1, 0.25, 0.5, 1, 2, 5, 10, 15, 20, 25, 30 and 50 mg ml$^{-1}$

- The samples were then immediately baked in a $N_2$ environment for 10 min at 150°C.

- Finally, the substrates were rinsed with DI water in order to remove the residual cesium and fluorine and then dried using compressed $N_2$.



**Figure 3.27** The ITO sample was spot welded on the molybdenum sample holder.

## 3.11 References

Barr, T. L. (1994). **Modern ESCAThe Principles and Practice of X-Ray Photoelectron Spectroscopy**. Taylor & Francis.

Briggs, D. and Seah, M. P. (1990). **Practical Surface Analysis: Auger and X-ray photoelectron spectroscopy**. Wiley.

Duke, P. (2008). **Synchrotron Radiation: Production and Properties**. OUP Oxford.

Einstein, A. (1905). Über einen die Erzeugung und Verwandlung des Lichtes betreffenden heuristischen Gesichtspunkt. **Annalen der Physik** 322: 132.

Fadley, C. (1978). Basic concepts of X-ray photoelectron spectroscopy. **Electron spectroscopy: theory, techniques and applications** 2: 1.

Grobosch, M. (2011). Electronic Properties of Organic Semiconductor/Electrode Interfaces: The Influence of Contact Contaminations on the Interface Energetic. **The Open Applied Physics Journal** 4: 8.

Hagström, S., Nordling, C. and Siegbahn, K. (1964). Electron spectroscopy for chemical analyses. **Physics Letters** 9: 235.

Hertz, H. (1887). Ueber einen Einfluss des ultravioletten Lichtes auf die electrische Entladung. **Annalen der Physik** 267: 983.

Hofmann, S. (2012). **Auger- and X-Ray Photoelectron Spectroscopy in Materials Science: A User-Oriented Guide**. Springer Berlin Heidelberg.

Hüfner, S. (2003). **Photoelectron Spectroscopy: Principles and Applications**. Springer.

Hüfner, S., Schmidt, S. and Reinert, F. (2005). Photoelectron spectroscopy—An overview. **Nuclear Instruments and Methods in Physics Research Section**

**A: Accelerators, Spectrometers, Detectors and Associated Equipment**
547: 8.

Kengkan, P., Pairsuwan, W., Isoyama, G., Yamakawa, T. and Ishii, T. (1998). Magnet lattice for the Siam Photon Source. **Journal of Synchrotron Radiation** 5: 348.

Lee, H.-L. and Flynn, N. T. (2006) X-RAY PHOTOELECTRON SPECTROSCOPY. In Handbook of Applied Solid State Spectroscopy(Ed, Vij, R. D.) Springer US, Boston, MA, pp. 485.

Nakajima, H., Tong-on, A., Sumano, N., Sittisard, K., Rattanasuporn, S., Euaruksakul, C., Supruangnet, R., Jearanaikoon, N., Photongkam, P., Chanlek, N. and Songsiriritthigul, P. (2013). Photoemission Spectroscopy and Photoemission Electron Microscopy Beamline at the Siam Photon Laboratory. **Journal of Physics: Conference Series** 425: 132020.

Note, A. A. A. (1995). Cleaning and Surface Activation of Microfabricated Interdigitated Microsensor Electrodes (IMEs), Planar Metal Electrodes (PMEs), Independently Addressable Microband Electrodes (IAMEs), and E'Chem "Cell-On-A-Chip".

Pairsuwan, W. (2007) The SIAM photon source. In AIP Conference Proceedings, Vol. 879, pp. 214.

Park, Y., Choong, V., Gao, Y., Hsieh, B. R. and Tang, C. W. (1996). Work function of indium tin oxide transparent conductor measured by photoelectron spectroscopy. **Applied Physics Letters** 68: 2699.

Schlaf, R., Murata, H. and Kafafi, Z. H. (2001). Work function measurements on indium tin oxide films. **Journal of Electron Spectroscopy and Related Phenomena** 120: 149.

Songsiriritthigul, P., Kjornrattanawanich, B., Tong-on, A. and Nakajima, H. (2007). Design of the first undulator beamline for the Siam Photon Laboratory. **Nuclear Instruments and Methods in Physics Research Section A: Accelerators, Spectrometers, Detectors and Associated Equipment** 582: 100.

Songsiriritthigul, P., Klysubun, P., Duangnil, S. and Pairsuwan, W. (2010) Present status of the siam photon laboratory. **In AIP Conference Proceedings**, Vol. 1234, pp. 289.

Songsiriritthigul, P., Pairsuwan, W., Ishii, T. and Kakizaki, A. (2001). Photoemission Beamline at the Siam Photon Laboratory. **Surface Review and Letters** 08: 497.

Weston, G. F. (2013). **Ultrahigh Vacuum Practice**. Elsevier Science.

Winick, H. and Doniach, S. (2012). **Synchrotron Radiation Research**. Springer US.

# CHAPTER IV

# RESULTS AND DISCUSSIONS

This chapter presents the experimental results and discussions of PES experiments for determination of work function (WF) of ITO. The experiments were carried out at BL3.2Ua of the Synchrotron Light Research Institute (SLRI), and thus the spectrum of synchrotron light from the beamline was characterized and given in the first part of this chapter. The second part focuses on the change in WF of ITO induced by synchrotron light irradiation. The last part is related to the changes in WF of ITO after modifying the ITO surface.

## 4.1    Synchrotron light at BL3.2Ua

It is noted that the light source at SLRI is operated in a decay mode; i.e. the electron current in the storage ring decreases with time. Consequently, the photon flux of all beamlines at SLRI simultaneously reduces with the electron beam current. At BL3.2Ua, a real-time monitoring system is implemented to follow the change in the photon flux. As mentioned in the previous chapter, a gold mesh is installed between the last optical element and the sample. The drain current from the mesh ($I_p$) is, in fact, sufficient to be used as a signal for normalization of the photoelectron spectra. During the course of this thesis work, the undulator, the light source of BL3.2Ua, was operated with a fixed gap of 26.5mm and the photon energy for the excitation and exposures was chosen by the monochromator. Figure 4.1 is the drain current of the

gold mesh ($I_p$) showing the variation of the photon flux generated by the undulator with the 26.5mm gap. The peaks at 40, 80, 120 and 160 eV correspond to the 1st, 2nd, 3rd and 4th harmonic radiations, respectively.
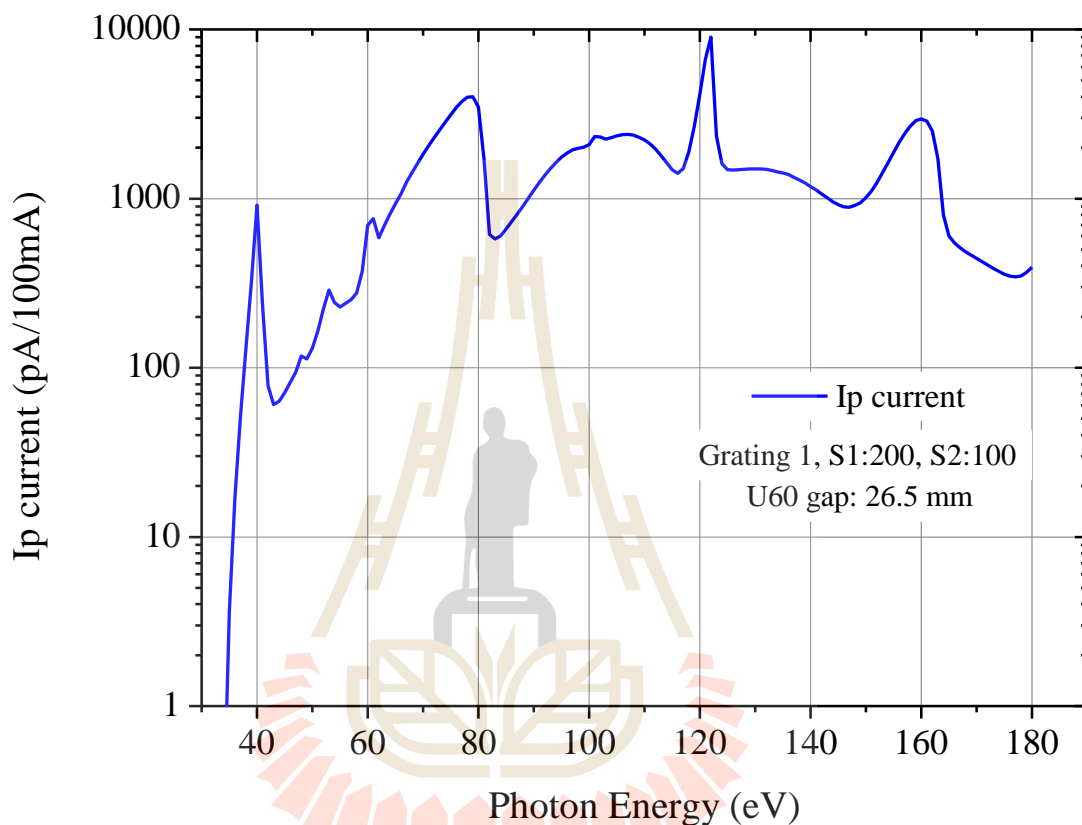


**Figure 4.1**    The drain current measured from the gold mesh located in front of the PES experimental station.

However, in this thesis work, absolute values of the photon flux are required in order to calculate the photon fluence irradiated on samples. Thus, a photodiode is used for measuring the absolute photon flux. The gold mesh and the photodiode are installed on the same linear motion drive so that both can be moved into the optical

axis of the beamline. The calibration curve to provide the actual photon flux is shown

in Figure 4.2.
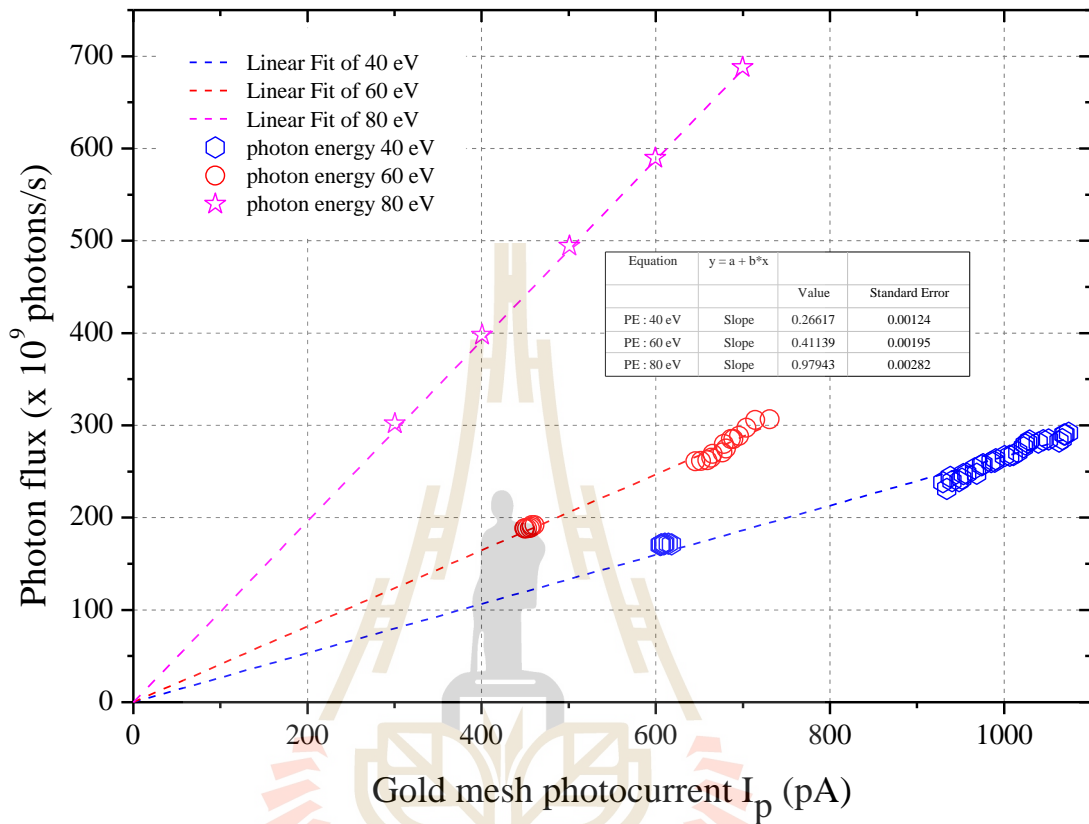


**Figure 4.2** The calibration curve to provide the photon flux for photon energy of 40, 60 and 80 eV at BL3.2Ua.

The number of photons irradiating on a unit area, photon fluence ($\varphi$), can be

obtained from the following relation:

$$\varphi = \int_{t=0}^{t} \frac{P_{(t)}}{A} \, dt$$

where $A$ is the irradiated areas ($cm^2$) of the sample at the irradiation chamber (0.3 mm

horizontal $\times$ 0.1 mm vertical at the sample position) and $P(t)$ is photon flux

(photons/s) and t is time (s).

With the calibration curve above, the quantum of efficiency of gold ($Q_g$) can be obtained. Figure 4.3 shows a linear fit of the average quantum efficiency of gold with the number of scans for each photon energy of 40, 60 and 80 eV. With a known quantum efficiency of gold, the photon fluence can directly be calculated from the drain current of the gold mesh, which is given by

$$\varphi = \int_{t=0}^{t} \frac{I_{p(t)}}{(0.65)eAQ_g} dt$$

It is noted again that the transmission of the gold mesh is 65%.
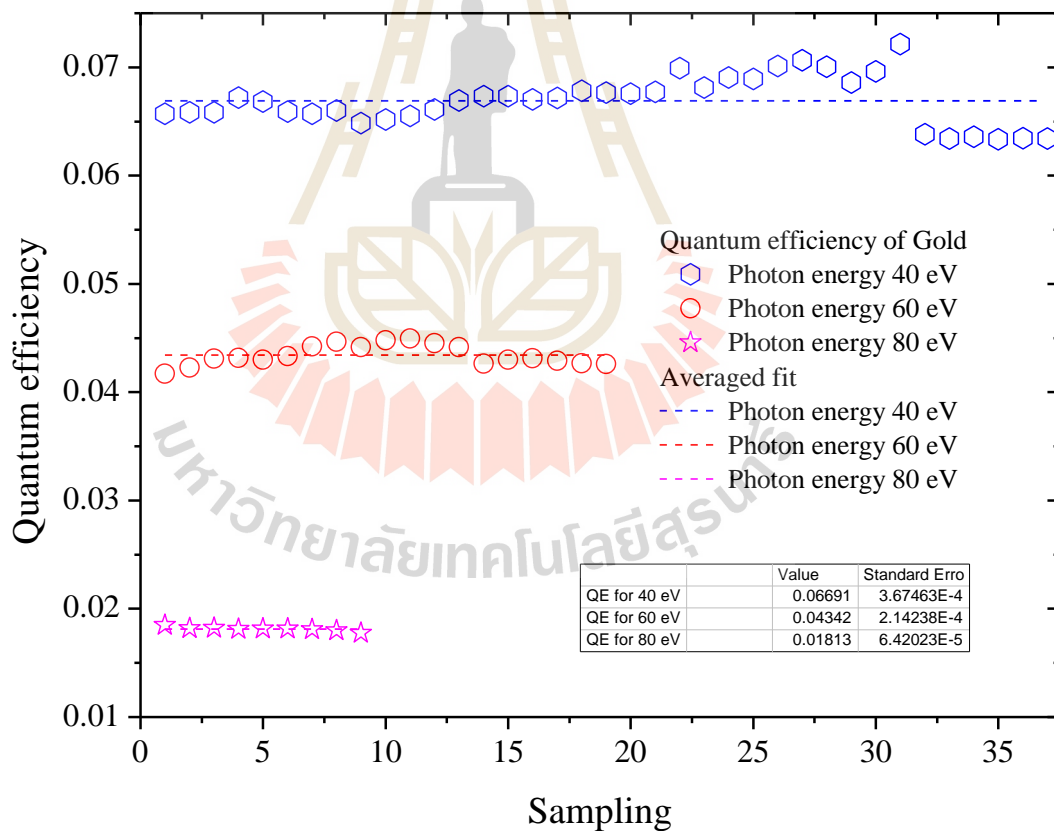


**Figure 4.3**    Quantum efficiency of gold for photon energy of 40, 60 and 80 eV.

## 4.2    Effect of synchrotron VUV irradiation on WF of ITO

The objective of this part is to study the changes in WF of ITO induced by synchrotron light irradiation. WF was measured by two exposure conditions; i.e. exposed with monochromatic light (VUV irradiation) and with polychromatic light (zero-order light irradiation).

### 4.2.1    Monochromatic light irradiation

Initially, *ex-situ* chemically cleaned ITO samples were measured at the photon energy of 600 eV before irradiation to investigate the surface chemical composition. Then ITO was exposed to synchrotron light under the different exposure conditions. After each exposure step, the surface chemical composition samples were checked by core level electron spectroscopy again. For VUV irradiation, the ITO samples were exposed to VUV with photon energies of 40, 60 and 80 eV and repeatedly measured the WF (as a function of increasing the number of scan or exposure time).

Figure 4.4 shows a series of secondary electron spectra which were taken from an *ex-situ* chemically cleaned ITO by exciting with 40, 60 and 80 eV monochromatized light. The determination of the cut-off of low kinetic energy secondary electrons is illustrated for the first scan of the measurements. The spectrum of the first measurement results in the highest cut-off energy (about 3.85 eV). The successive measurements yield lower cut-off energy, indicating the reduction of the WF of ITO after exposing to 40, 60 and 80 eV light. To quantify the exposure of ITO, the number of photons illuminating on the ITO for every scan was calculated. Thus, a plot of the WF as a function of photon fluence was obtained and shown in Figure 4.5.
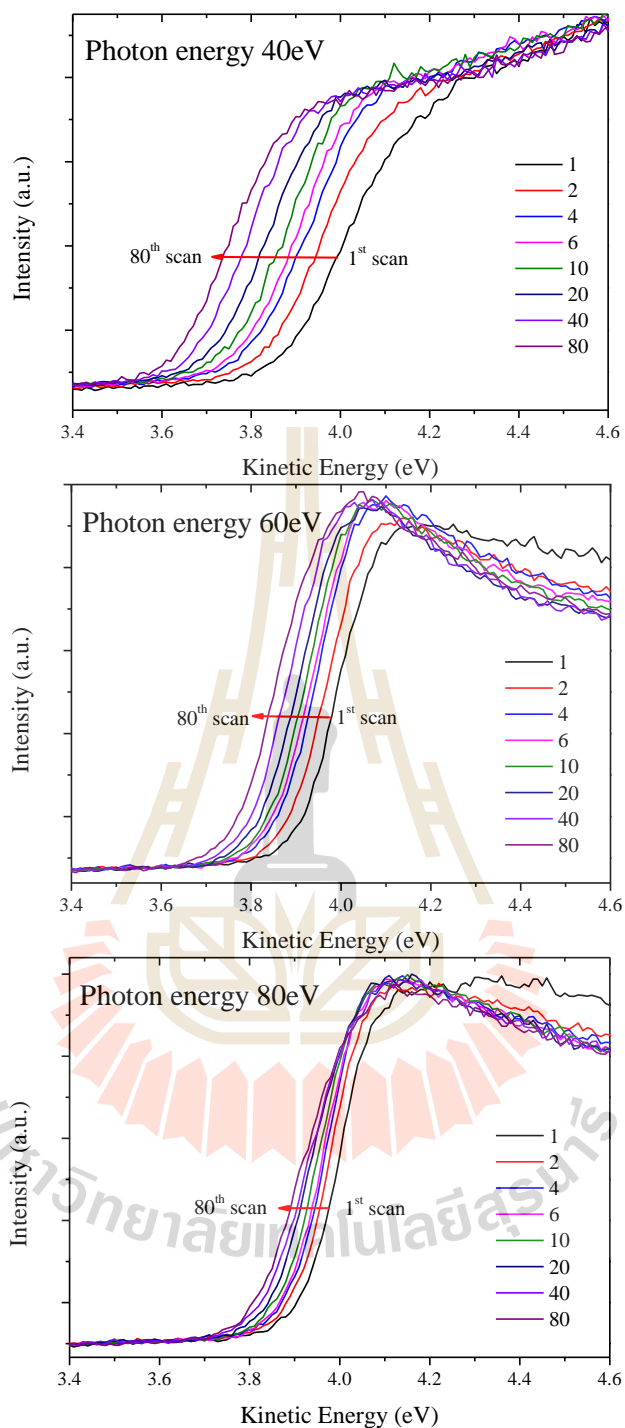
**Figure 4.4** Spectra of secondary electrons emitting from *ex-situ* chemically cleaned ITO samples when excited with 40, 60 and 80 eV monochromartized light, showing the shift of the spectra towards lower kinetic energy with increasing number of scans.
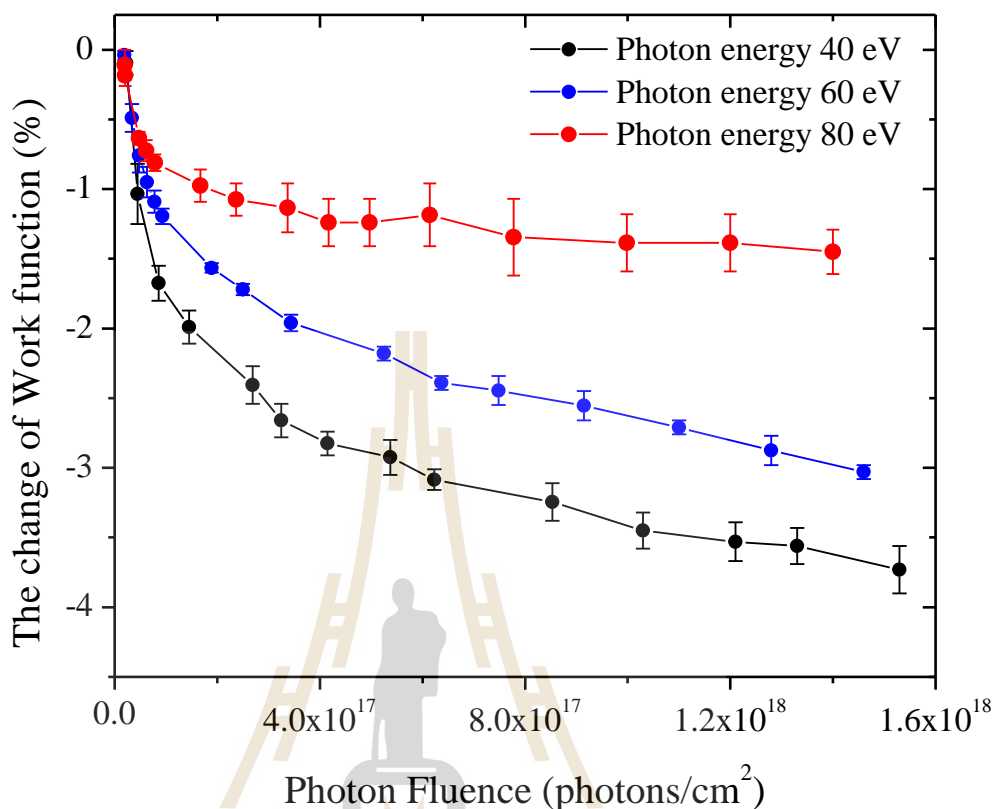
**Figure 4.5**    Plots of the change in work function of ITO versus photon fluence measured by using VUV light with photon energy of 40, 60 and 80 eV.

Figure 4.5 shows the plots of the change in WF of ITO versus photon fluence measured at photon energy of 40, 60 and 80 eV. The WF of ITO decreased with increasing exposure time or fluence of photons from the initial value of ITO WF, which is about 4.74 eV. After irradiation with the photon energy of 40, 60 and 80 eV, it was found that the WF was rapidly decreased and then a slowly decreased when the photon fluence increased. It can be observed that the changes in the WF of ITO might be related to the photon energy. The total shift of the WF excited by photon energy of 40, 60 and 80 eV at photon fluence of $1.5 \times 10^{18}$ photons/cm$^2$ is 3.5%, 3.0% and 1.5%,

respectively. The rate of the reduction is decreases when the photon energy increased. These results suggested that VUV with low photon energy induces more change in WF than VUV with high photon energy. This is in agreement that previously reported by Yi *et al.* (Yi *et al.*, 2006). According to the previously reported paper, the reduction was decreased about 12.13% in a few minutes in a UPS measurement (using He I 21.21 eV) and the reduction found in XPS and LIXPS (low intensity XPS) measurements were 6.36% and 3.81%, respectively (Beerbom *et al.*, 2006).

Figure 4.6 shows the PES spectra of C1s, O1s, In3d and Sn3d taken from a cleaned ITO sample before and after VUV irradiation. The PES measurements were performed by using light with photon energy of 600 eV. The spectra were normalized by the photon current ($I_p$) of the gold mesh for each scan and then the secondary electrons background of the spectra was subtracted using the shirley background algorithm (Shirley, 1972). This background algorithm was used in the spectral analysis and carried out throughout this thesis work. The binding energy in this thesis work was referred directly to the Fermi level at 0.0 eV. The binding energies C1s and O1s were 284.6 eV and 530 eV, respectively. The In3d and Sn3d peaks can be separated into spin-orbit splitting with the binding energy of In3d$_{5/2}$ at 444.3 eV and 3d$_{3/2}$ at 451.8 eV, the peak positions of Sn3d$_{5/2}$ was 486.3 eV and of Sn3d$_{3/2}$ was 494.8 eV. The difference in intensity of the different elements before and after VUV irradiation could be observed. C1s and O1s are reduced after VUV irradiation however In3d and Sn3d are increased, indicating that the surface contamination on ITO samples was reduced.
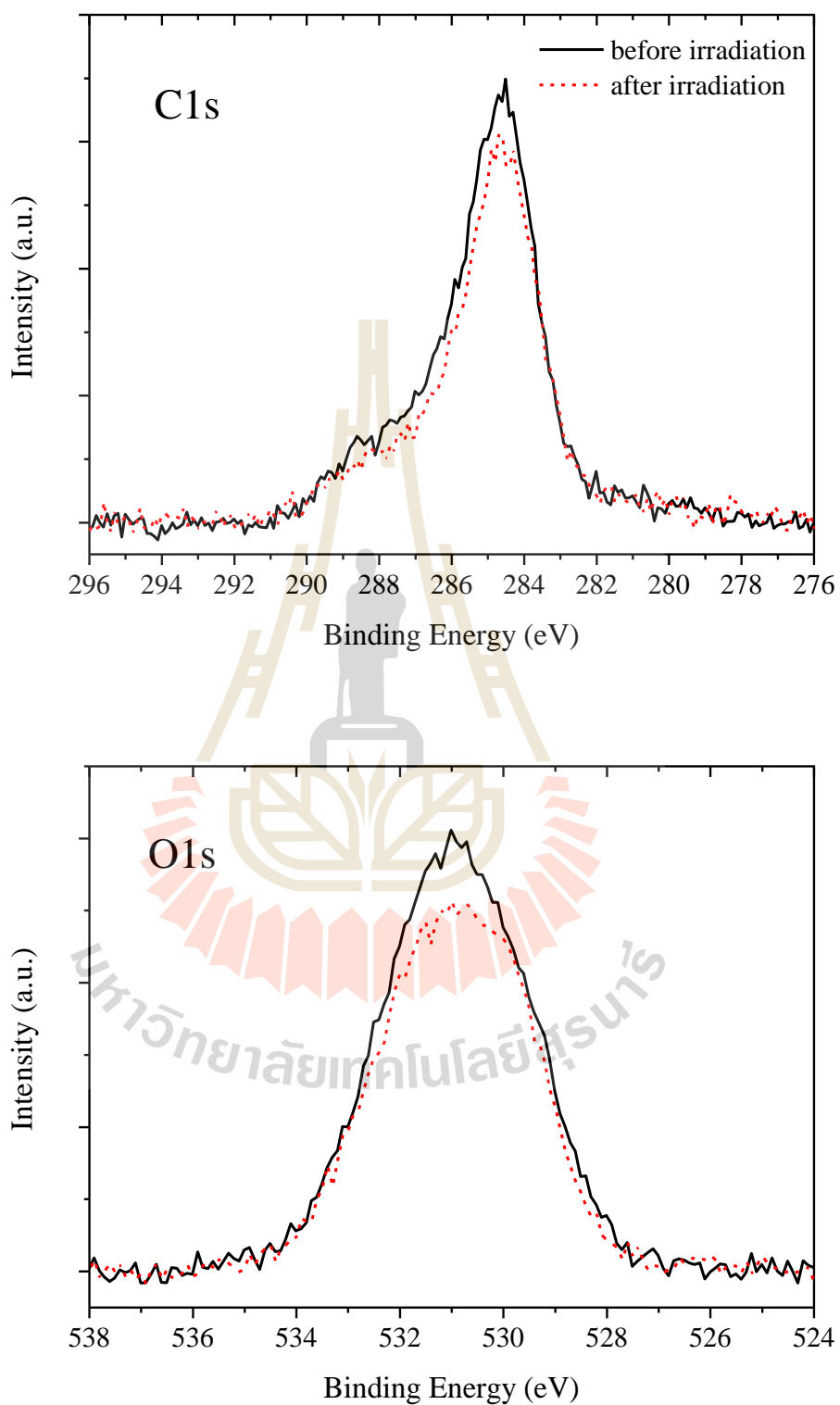
**Figure 4.6**    C1s, O1s, In3d and Sn3d spectra of ITO before and after VUV
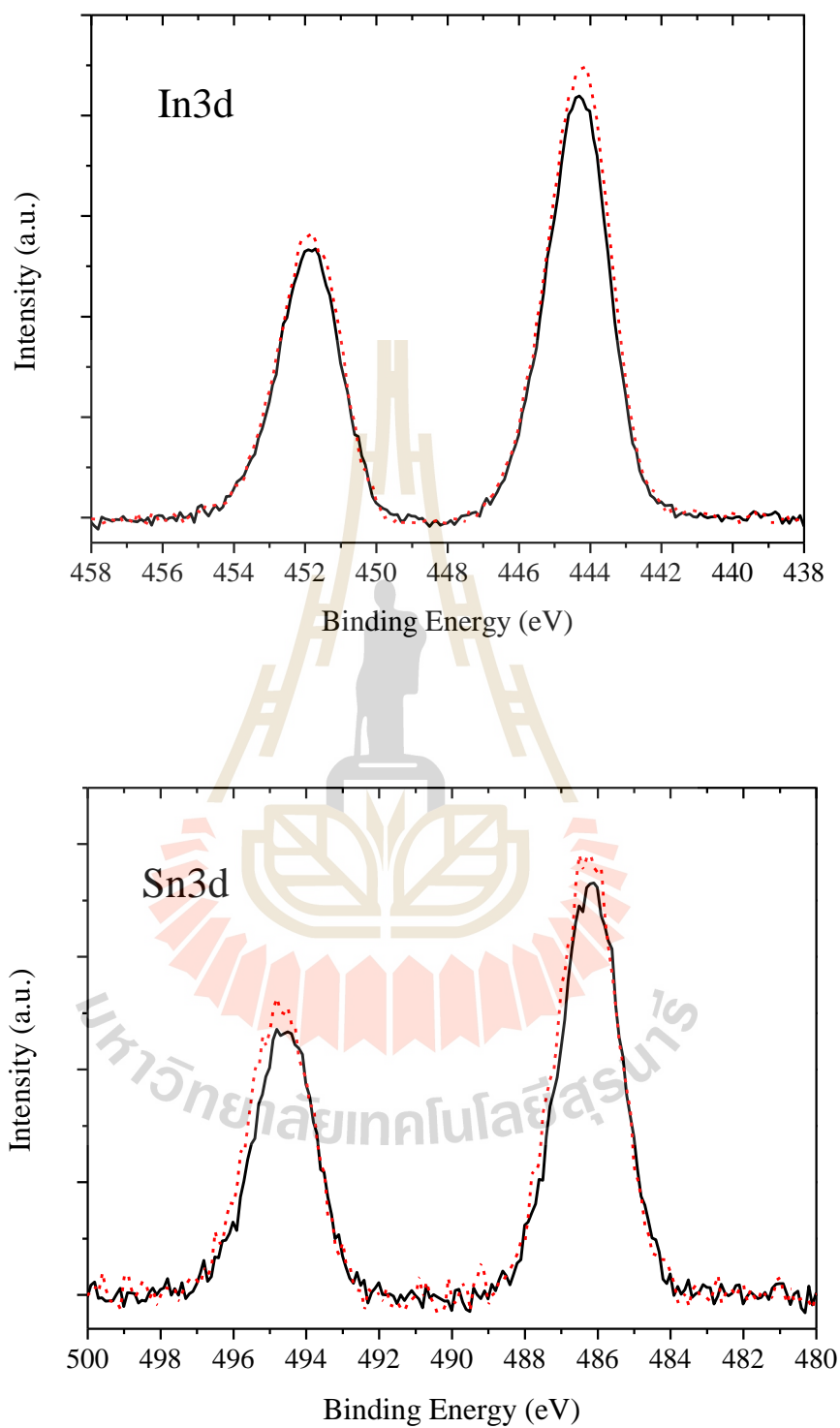
irradiation.

**Figure 4.6** C1s, O1s, In3d and Sn3d spectra of ITO before and after VUV
irradiation (Continued).

It is noted that the C1s peak is mainly from carbon contamination. However it is important to mention also that the O1s peak is originated from both oxygen contaminations and ITO. The curve-fitting was used to estimate the elemental composition. The curve-fitting results of the O1s on clean ITO before and after VUV irradiation during WF measurement are shown in Figure 4.7(a). Three oxygen species with peak positions at 530.3, 531.0 and 532.3 eV were considered (Wang *et al.*, 2004). The first peak at the lowest binding energy of 530.3 eV was assigned to oxygen in $In_2O_3$, the medium binding energy of 531.0 eV was assigned to oxygen in amorphous ITO or oxygen deficiency phases. The highest binding energy of 532.3 eV was assigned to oxygen in the surface contamination. Furthermore, a large difference of the O1s area before and after VUV irradiation was found in the ratio for each component. The oxygen surface contamination (peak at 532.3 eV) decreased from 28.3% to 16.5% after exposure to VUV irradiation. The peak area of lowest binding energy of the oxygen in the $In_2O_3$ increased from 28.4% to 64.8% and that of oxygen defect decreased from 43.3% to 18.7%. The significant decrease in the oxygen surface contamination (peak at 532.3 eV), it might be due to the environmental contamination (water, CO, $CO_2$, hydrocarbons) on the surface (Schlaf *et al.*, 2001).

In order to verify the effect of surface contamination, the sample was sputtered with Ar ions for 5 min at 3.0 keV to remove the contaminants from ITO surface. Figure 4.7(b) shows deconvolution of O1s peak for the sample after 5 min of sputtering before and after 40 eV VUV irradiation. The three species of oxygen are studied. The result shows that the amount of 3 species of oxygen did not change after prolonged VUV irradiation.

The XPS results on the composition of indium, tin and oxygen taken from the sputtered and cleaned ITO samples are given in table 4.1. For the cleaned sample, when irradiated with VUV the concentration of carbon contamination was decreased from 21.6to 19.8%. As a results. we could observe the increase of O, In and Sn from 64.4, 10.6 and 3.4 to 64.9, 11.7 and 3.6, respectively. It is interesting to note that during 40 eV VUV irradiation (PES measurements), the WF of the sputtered ITO does not change.
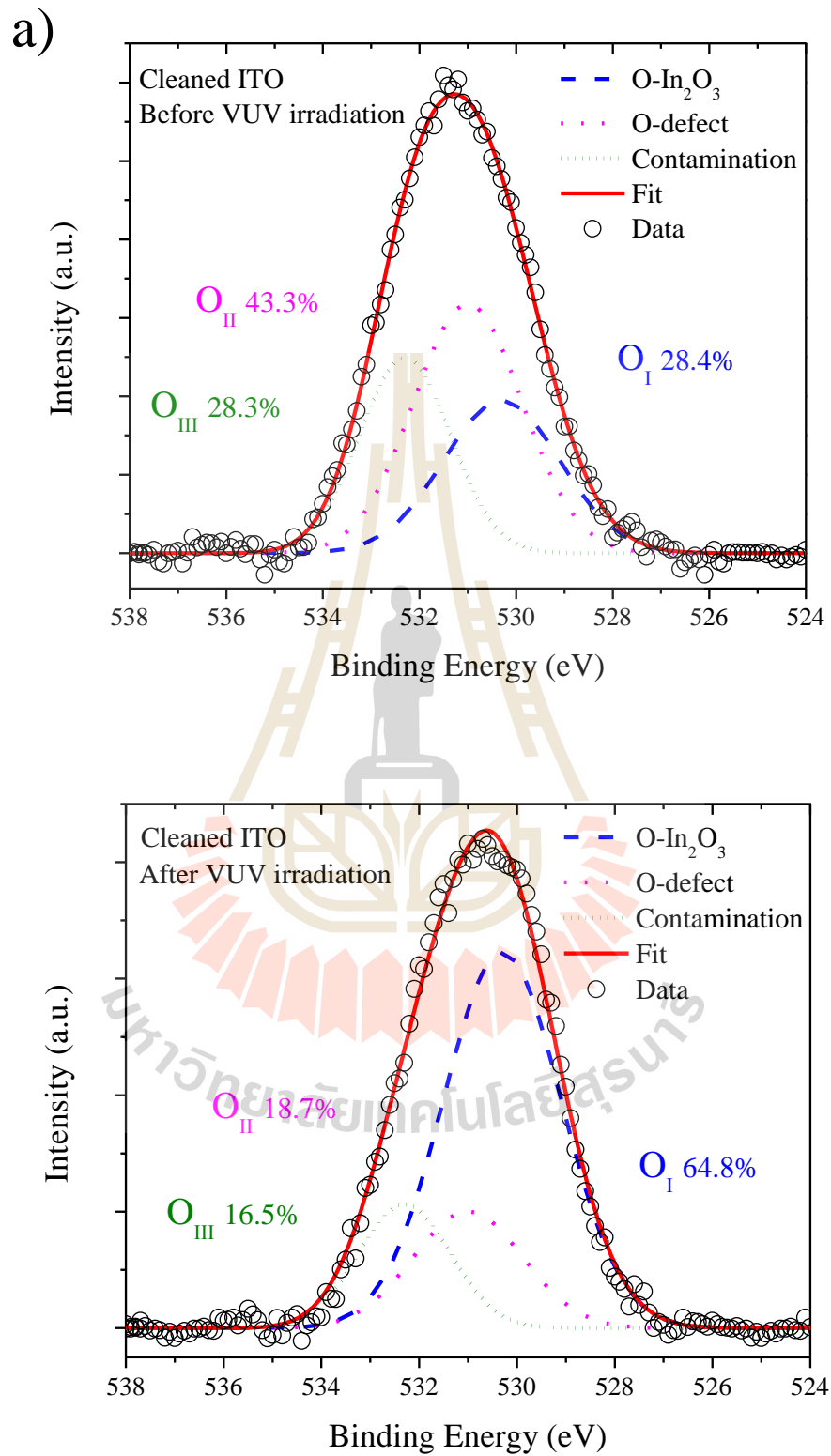
**Figure 4.7** The O1s spectra of ITO before and after treated with VUV irradiation.

a) Cleaned ITO b) sputtered ITO.
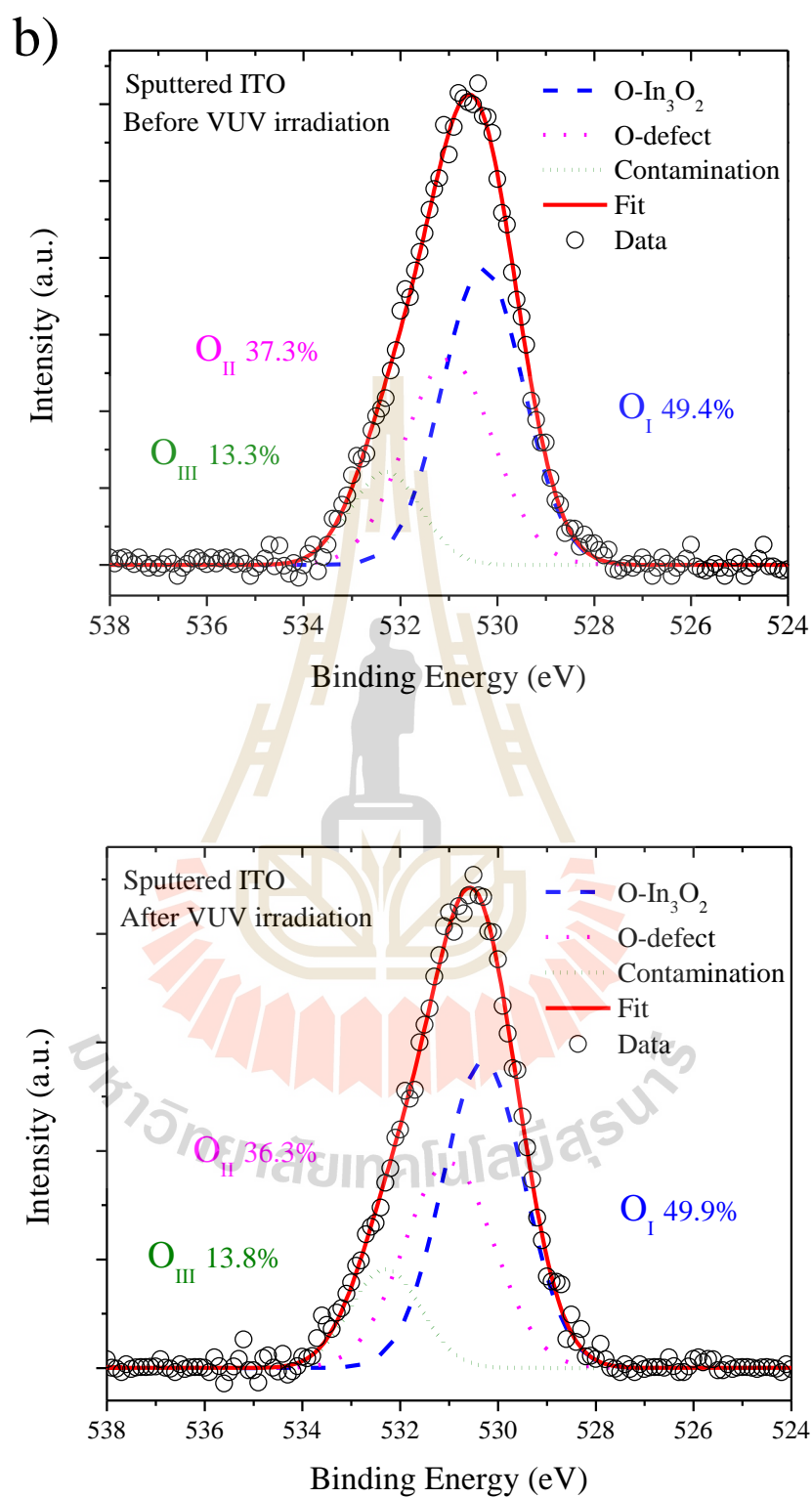
**Figure 4.7** The O1s spectra of ITO before and after treated with VUV irradiation.

a) Cleaned ITO b) sputtered ITO (Continued).

**Table 4.1**    Surface compositions of non-sputtered and sputtered samples before and after 40 eV VUV irradiation.

| Treatment | Chemical composition in at. % | | | |
|---|---|---|---|---|
| | O | In | Sn | C |
| Before irradiation | 64.4 | 10.6 | 3.4 | 21.6 |
| After VUV irradiation | 64.9 | 11.7 | 3.6 | 19.8 |
| $Ar^+$ sputtering 05 min | 60.8 | 29.0 | 10.2 | - |
| $Ar^+$ sputtering 05 min & After VUV irradiation | 60.7 | 29.3 | 10.0 | - |

To estimate the amount of light absorbed by contamination and ITO, mass absorption coefficients for ITO and surface contamination were calculated and are shown in Figure 4.8. The variation of the mass absorption coefficients between ITO and surface contamination as a function of photon energy can be observed at photon energy between 20-100 eV. High mass absorption coefficients indicates more photon absorption and also may introduce more interaction with the surface. It is obvious from the figure that the mass absorption coefficient for surface contamination at 21.2 eV (normally used in laboratory UPS measurements) is much higher than that at 40, 60, and 80 eV (used in this work). In UPS measurements, the reduction of WF is much higher than observed in this work when using 40, 60 and 80 eV photons. This suggests that the amount of energy absorbed by the contaminations layer related to the magnitude of the reduction of WF. In the opposite, the amount of energy absorbed by ITO shows no relation to the magnitude of the reduction of WF of ITO.
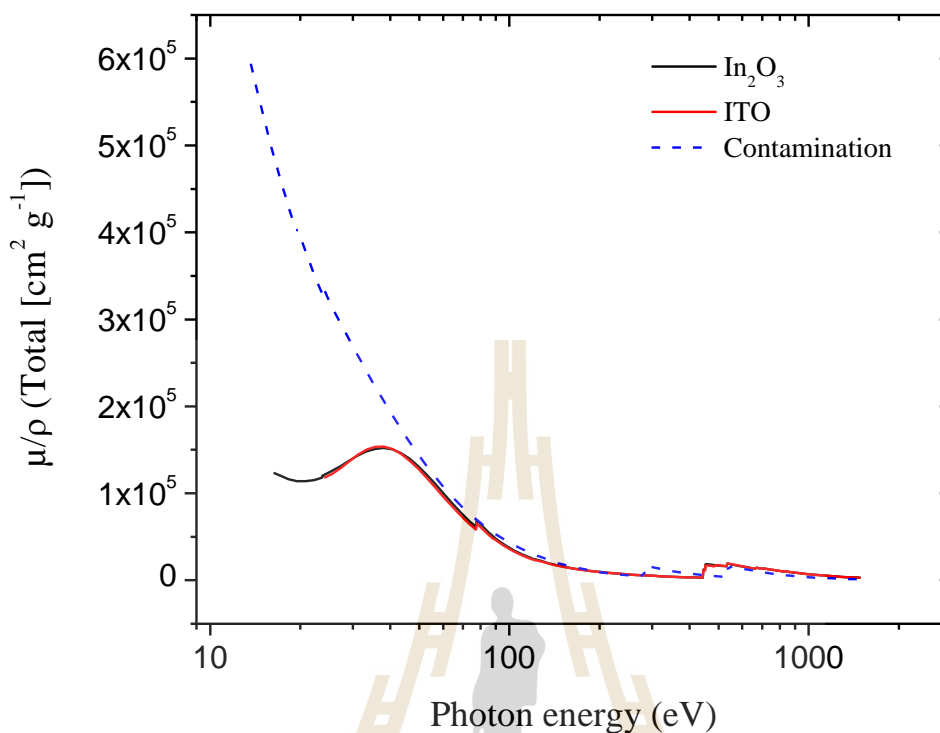
**Figure 4.8**   Calculated   mass   absorption   coefficients   of   hydro   carbon

contamination, ITO and $In_2O_3$.

### 4.2.2   Zero-order light irradiation

In addition to the VUV irradiation, ITO samples were also irradiated by using

polychromatic beam (zero-order light) that produced by the U60 undulator at a gap of

26.5 mm. Prior to the zero-order light irradiation, the spectra were measured to obtain

the WF of ITO by PES measurements with the photon energy of 40 eV. Then the ITO

samples were exposed to the zero-order light with different exposure times (10, 20

and 30 min) with $I_0$ current about 3 μA. After irradiation under zero-order light, the

WF of ITO spectra were measured again with the photon energy of 40 eV. In order to

observe the 40 eV of VUV irradiation effect during PES measurement, the WF was measured with a series of PES measurements.

Figure 4.9 shows the spectra of secondary electrons in the cut-off energy region for a cleaned ITO sample and after irradiation with the zero-order light for 10, 20 and 30 min. The secondary cut-off energy reveals a slightly shift toward higher kinetic energy with the exposure time. However, the shift of the secondary electron cut-off energy of the samples with and without treated by the zero-order irradiation are quite different when the number of scans was increased. For the sample without irradiation of the zero-order light, the secondary electron cut-off shifts toward a lower kinetic energy than that taken from the sample irradiated with the zero-order light. In summary, a plot of the WF as a function of photon fluence was obtained, and shown in Figure 4.10.
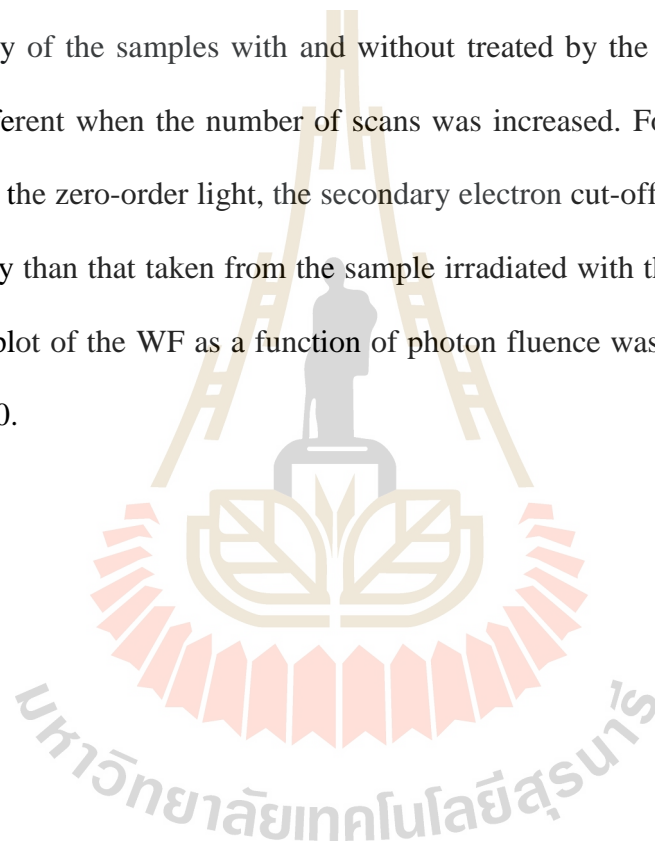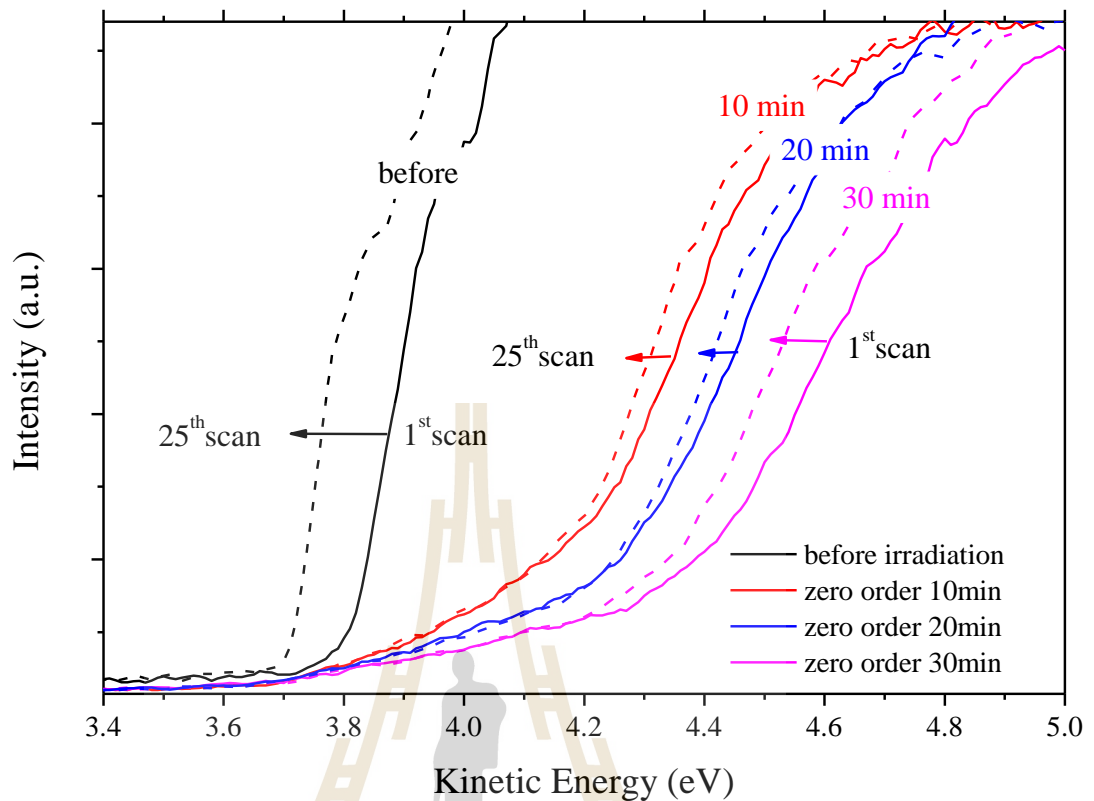
**Figure 4.9** The secondary electron cut-off energy of cleaned ITO irradiated with the zero order light for 10, 20 and 30 min. The spectra were measured by using the excitation with photons energy of 40 eV.

Figure 4.10 shows the change in WF of the ITO irradiated with the zero-order light for 10, 20 and 30 min. The WF was measured with 40 eV excitation photon energy. Conventional PES measurements were performed to observe the change in WF. This plot indicates that the initial WF of clean ITO can be increased to 10%, 12% and 14% when treated with the zero-order light for 10, 20 and 30 min, respectively. Under the same fluence of $6 \times 10^{17}$ photons/cm$^2$, the effect of 40 eV VUV irradiation on ITO is the reduction of WF about 3% while those samples treated with the zero-order light are pretty stable, the reduction is less than 1%. To explain the cause of the

increase in the WF of ITO treated by the zero-order light, PES was used to measure the surface chemical composition of the samples before and after irradiation.
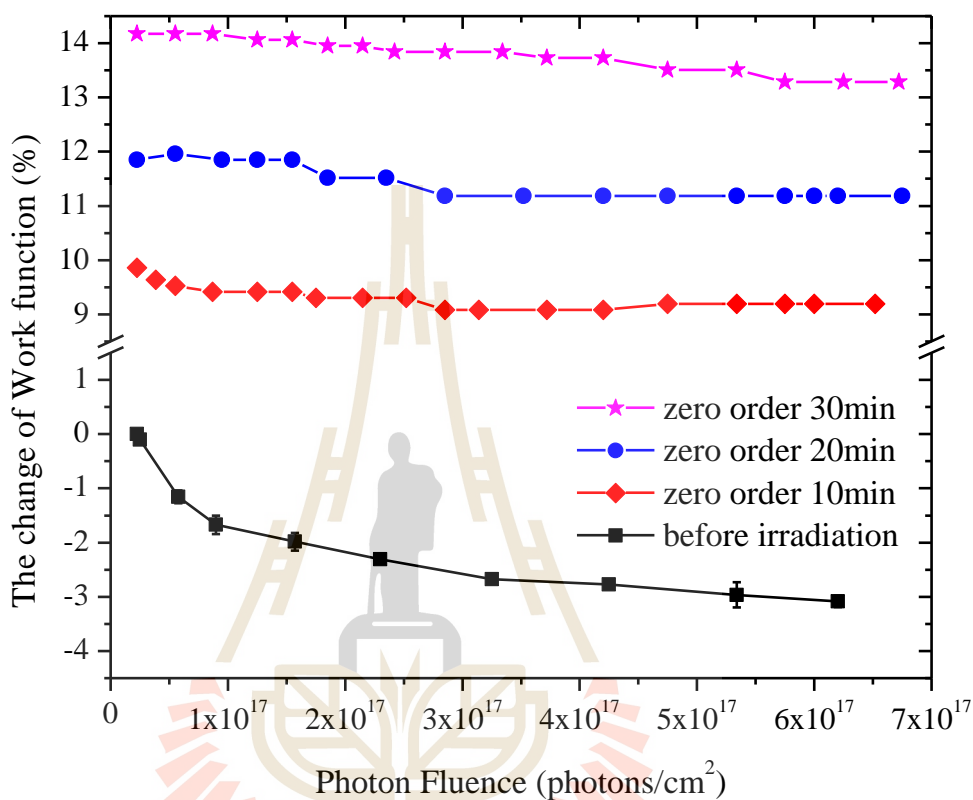


**Figure 4.10**   Plots of the change in WF of ITO irradiated with the zero-order light for 10, 20 and 30 min versus photon fluence of the excitation 40 eV.

Figure 4.11 shows the C1s spectra of ITO before and after irradiated with the zero-order light for 10, 20 and 30 min. The C1s is assigned to the carbon contamination on the surface of ITO. The results show that the intensity of C1s was reduced when the zero-order time increased. This result is related to the components of ITO surface that could be affected to the WF of ITO.
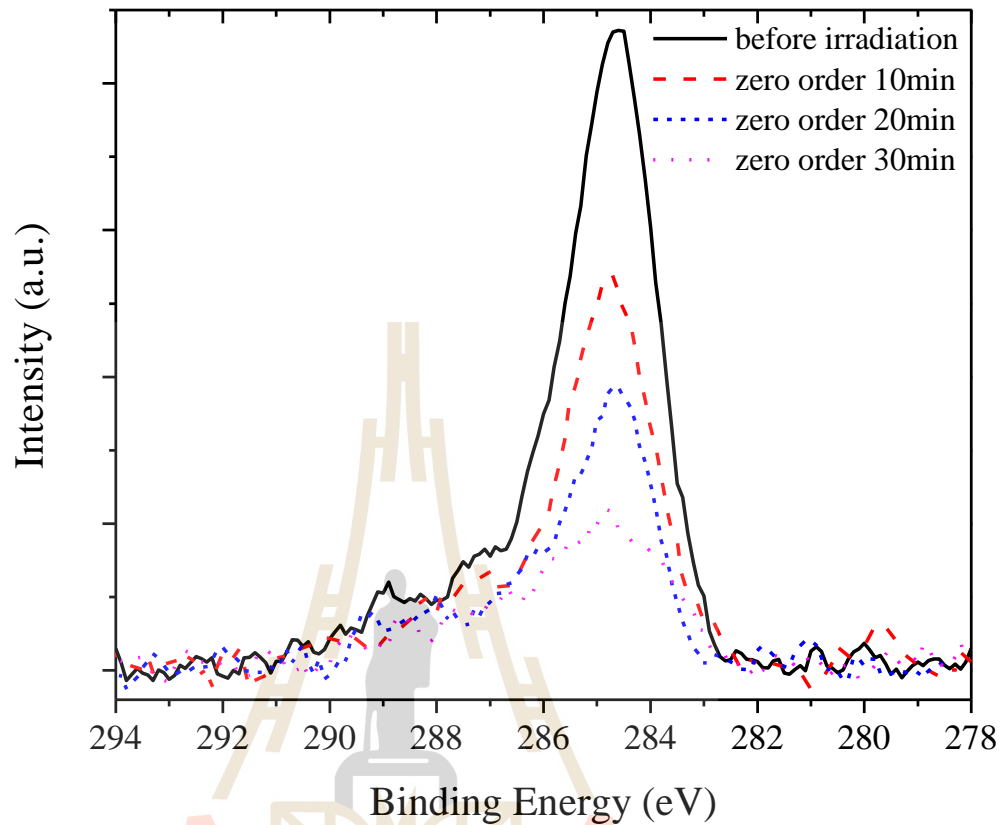
**Figure 4.11**  The C1s spectra of ex-situ chemically cleaned ITO before and after irradiated with the zero-order light for 10, 20 and 30 min.

Figure 4.12 shows WF of ITO and the change of carbon contamination as a function of zero-order irradiation time. As the zero-order irradiation time increases, it is found that WF has increased and the total removal amount of carbon contamination was increased with exposure time. The table 4.2 shows the chemical composition of ITO irradiated with the zero-order light. The results show that the atomic concentration of carbon was decreased after zero-order irradiation from 16.1 to 6.9, 4.4 and 3.5% when exposured to the zero-order light for 10, 20 and 30 min,

respectively. However, oxygen is also increased which is attributed to the loss of indium and tin, resulting in a change in the relative ratio between indium, tin and oxygen.
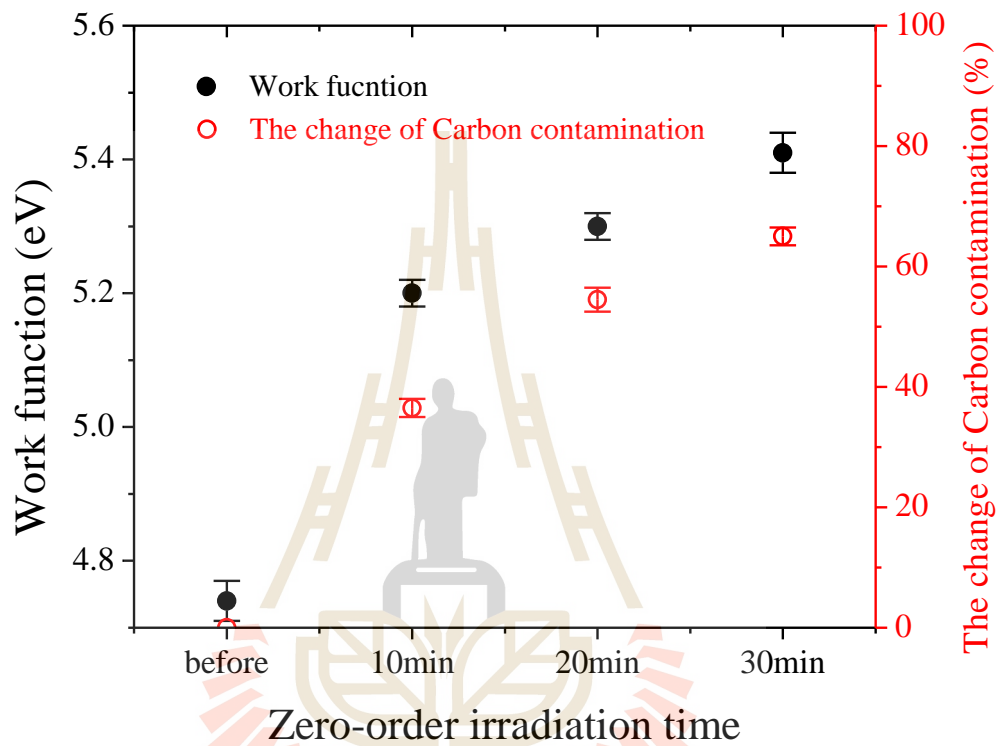


**Figure 4.12**  The work function of ITO and the change in carbon contamination as a function of zero-order irradiation time.

**Table 4.2**     The atomic concentration of ITO irradiated with zero-order light for 10, 20 and 30 min.

| Treatment | Chemical composition in at. % | | | |
|---|---|---|---|---|
| | O | In | Sn | C |
| Before irradiation | 70.7 | 9.9 | 3.3 | 16.1 |
| Zero-order  irradiation 10 min | 77.9 | 11.0 | 4.2 | 6.9 |
| Zero-order  irradiation 20 min | 81.8 | 10.0 | 3.8 | 4.4 |
| Zero-order  irradiation 30 min | 82.7 | 10.2 | 3.6 | 3.5 |

In order to investigation the components in the O1s peak of ITO. The measured O1s peak for each exposure was curve-fitted and shown in Figure 4.13. The first peak at the lowest binding energy of 530.3 eV can be assigned to oxygen in the $In_2O_3$. The peak at the binding energy of 531.0 eV can be assigned to oxygen in amorphous ITO or oxygen deficiency phases. The highest binding energy of 532.3 eV can be assigned to oxygen in the surface contamination. The Oxygen contamination at higher binding energy at 532.3 eV was dramatically decreased from 32.2% to 7.4% after treated with zero-order of 10 min and then slightly declined to 6.2% and 6.4% after exposed for 20 and 30, respectively.

It is interesting to point out that the reduction of surface contaminations on ITO when irradiated with zero-order light is much more than when irradiated with 40 eV VUV. For the zero-order light irradiations, the reduction of C contamination is more than 55% while it is only 8.5% for 40 eV VUV irradiation. Only the reduction of the surface contaminations may not be the reason for the increase of the WF of ITO. The cause for the increase of the WF might be that the zero-order light might

induce chemically interaction between the contaminations and the ITO surface atoms causing the formation of dipole layer on the ITO surface. This dipole layer becomes more effective with the decrease of thickness of the contamination layer or the reduction of the top most contamination layers. This similar to the case of ITO clean with UV ozone where the WF can be increase (Sugiyama *et al.*, 2000).
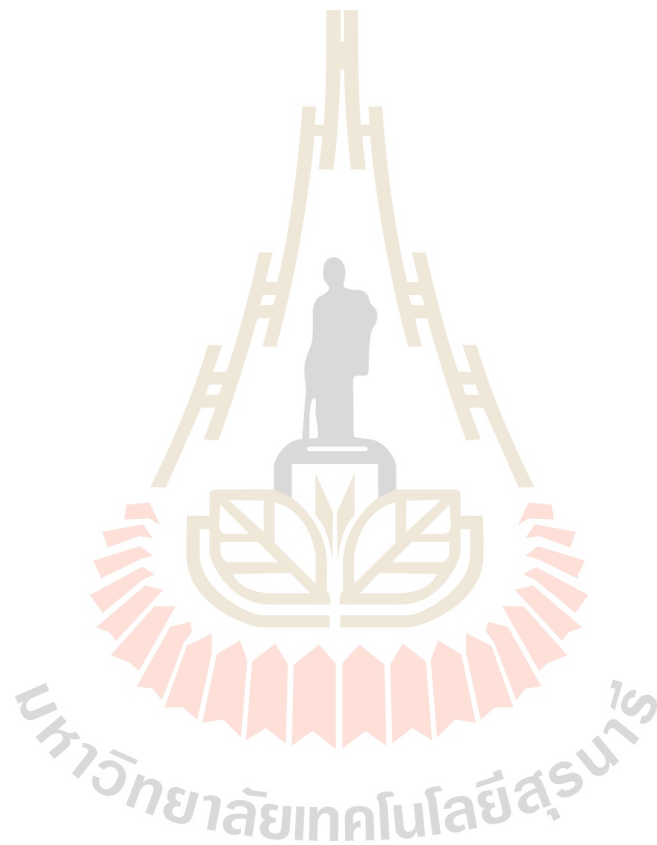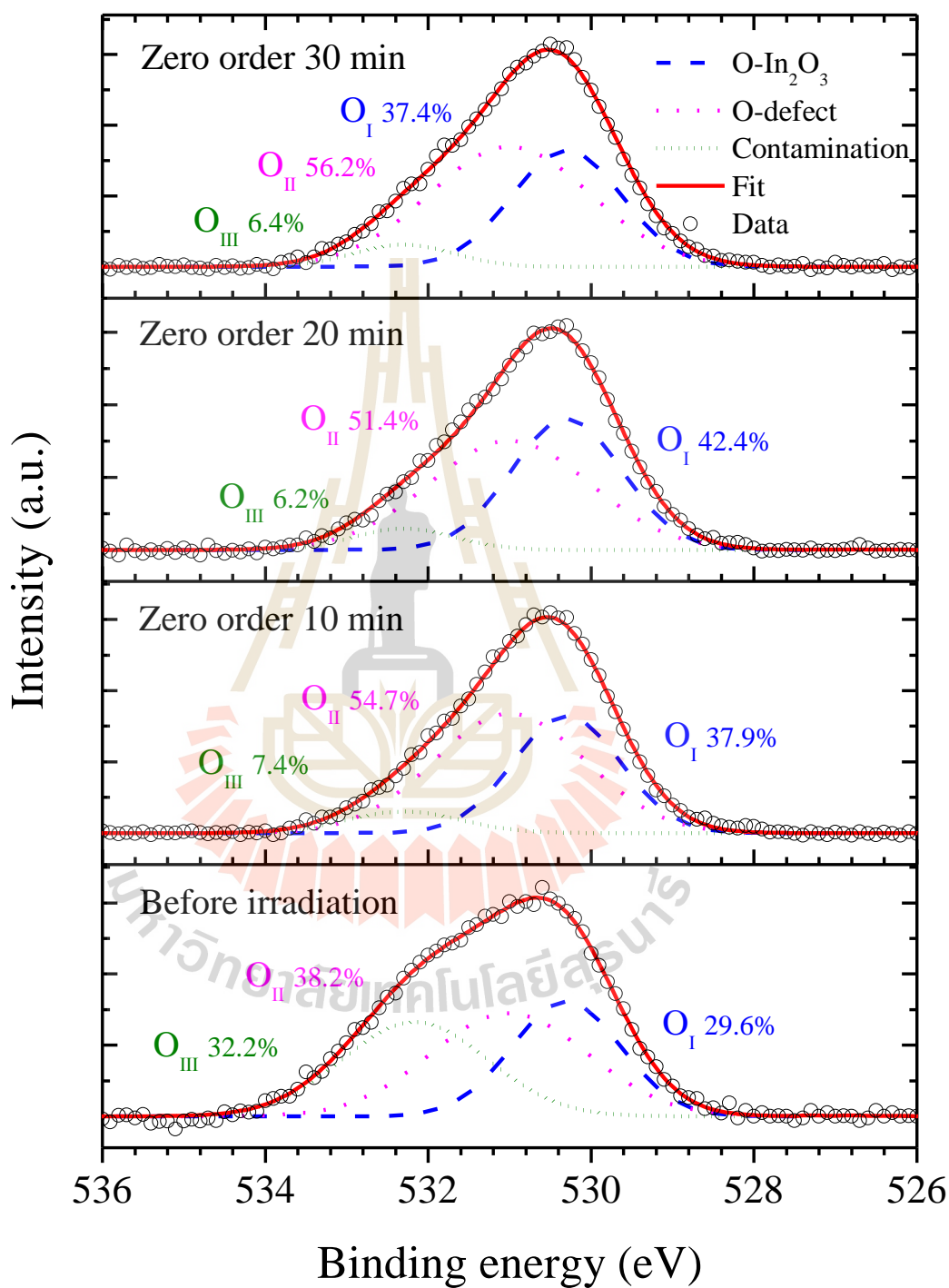
**Figure 4.13** The O1s spectra of ITO before and after treated with the zero-order irradiation for 10, 20, and 30 min.

### 4.2.3   Additional effects from gas exposure

Firstly, the surface contaminations on ITO were removed by using Ar ion sputtering with 3.0 keV for 20 minutes. Then, the samples were exposed to oxygen under the pressures of $5 \times 10^{-8}$, $1 \times 10^{-7}$ mbar, 1 atm. In addition, air exposure was also performed. Oxygen gas was fed into the PES analysis chamber through a liquid N-cooling trap to get rid of possible water vapor. For air exposure, the sputtered sample was bought out to air for 20 minutes and bought back to the PES system again. The WF was evaluated with different environmental conditions by using PES. The core-level PES spectra were measured to identify a chemical state and peak area in each oxygen exposure conditions.

However, to understand the mechanism of carbon and oxygen desorption processes on the ITO surface, it is necessary to systematically study the chemical state and its change with ITO WF change as a function of oxygen under the controlled environment.

Figure 4.14 shows the WF of ITO under different environmental conditions. The WF was measured by using VUV with photon energy of 40 eV as a function of number of scans up to 50 scan. This plots was started from freshly clean ITO samples, the WF was started from around 4.7 eV then decreased by VUV irradiation which is similar to the previous results. Then fresh samples were in-situ cleaned by using Ar ion sputtering. The contamination can be removed by using Ar ion sputtering, which would decreased the WF corresponded to previous report of 4.0 eV and its value does not change during VUV irradiation. This agrees with the results reported previously (Song *et al.*, 2001; Sugiyama *et al.*, 2000). For the samples exposed to oxygen at $5 \times 10^{-8}$ and $1 \times 10^{-7}$ mbar, the WF gradually increased during WF measurements as

shown in the Figure 4.14. For exposure at 1 atm of oxygen for 20 min, the increases of the WF is about 0.4 eV and it does not change during PES measurements using 40 eV VUV. It was found that the WF can be increased close to initial value by exposure to air. However, the WF is still decreased (during VUV irradiation).
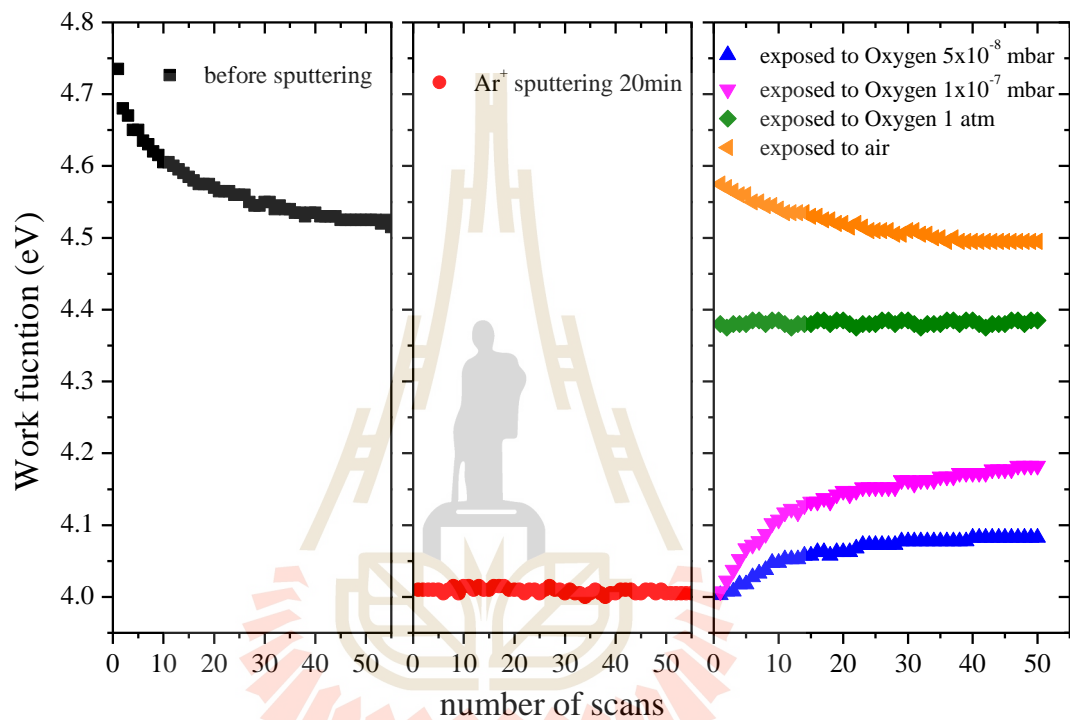


**Figure 4.14** The change of work function induced by VUV irradiation, Ar ion sputtering and surface impurities under pressure different oxygen environments.

To understand the causes behind the change in WF of ITO, the oxygen concentrations were plotted as a function of the change of atomic concentration for each pressure exposure condition as shown in Figure 4.15. These results revealed that the sputtered samples after adding the oxygen in higher pressure indicates the increase of oxygen concentration. It can be seen that the WF largely increases when the change of oxygen increased. These results might be one of the reasons for the increases of ITO WF. However, the difference between exposure to air and 1 atm may be observed. For the sputtered sample exposed to 1 atm of air, the effect of 40 eV VUV irradiation is observed with a number of PES measurements. This is not observed for the sputtered sample that was exposed to 1 atm of oxygen.

More detailed analysis were done by curve-fitting of O1s peak. Figure 4.16 shows O1s core level peak taken from ITO samples with different oxygen exposure conditions. The results can be divided into 3 components at 530.3, 531.0 and 532.3 eV. The first peak at the lowest binding energy of 530.3 eV can be assigned to oxygen in the $In_2O_3$, the medium binding energy of 531.0 eV can be assigned to oxygen in amorphous ITO or oxygen deficiency phases. The highest binding energy of 532.3 eV can be assigned to oxygen from the surface contamination.
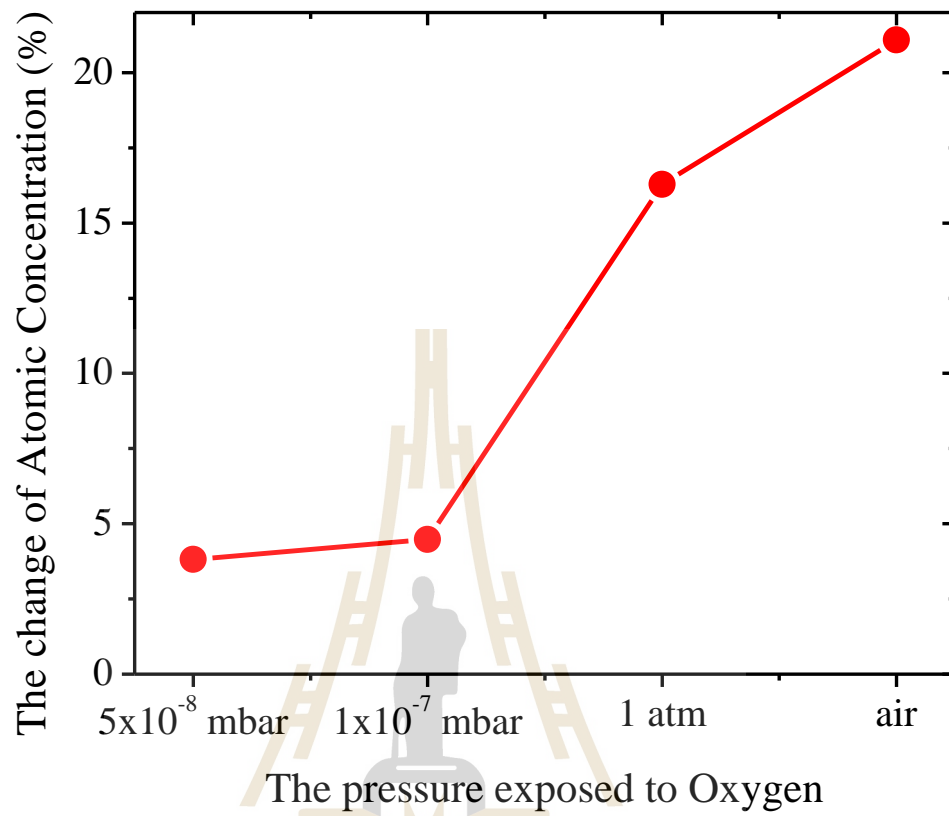
**Figure 4.15**    The increase of O1s after irradiated with the different of oxygen environmental exposed condition.
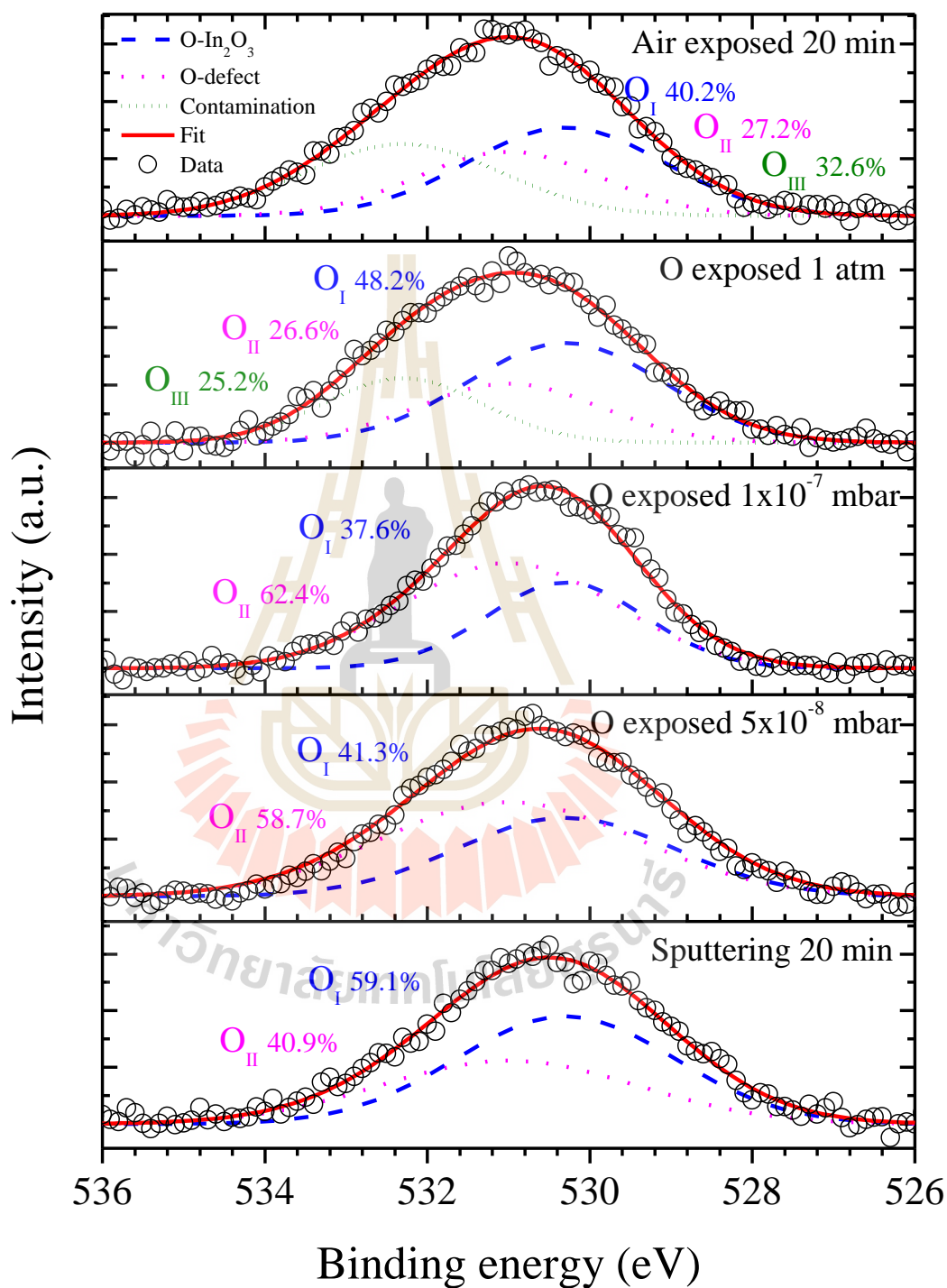
**Figure 4.16**   The curve-fitting of the O1s core level peak taken from ITO samples

with different oxygen exposure conditions.

## 4.3 Effects of surface treatment on WF of ITO

### 4.3.1 Surface chlorination

Figure 4.17 shows the WF of the chlorinated ITO samples as a function of UV exposure time during the functionalisation process. It is obvious that UV-ozone treatment induces great effects on the increase of WF. The WF of the samples before sputtering is shown as the lowest curve. It is found that the WF was increased as the UV irradiation time increases is about 4.7 to 5.0 eV. However, there has been a report that the WFs of chlorinated ITO could be tuned between 6.1-4.7 eV with increasing UV exposure time (Helander *et al.*, 2011). Our measured WF values of the chlorinated ITO are over 1 eV lower than previously reported.

Then the chlorinated ITO samples were sputtered with Ar ion sputtering for 5 min at 0.5 keV to clear the ITO surface. The WFs of the samples after 5 min of sputtering are plotted as the top curve in Figure 4.17. It is interesting to observe the increase of WF up to between 5.7 eV to 5.8 eV, with the highest WF of 5.8 eV for a UV exposure time of 10 min. This can be attributed to the fact that Ar ion sputtering has remove the carbon contaminants on the surface of the Dichlorobenzene (DCB) treated ITO.

However, when the samples were sputtered for a further 5 min, the WF decreased again as shown in the middle curve in the figure. The WFs of the samples after a further 5 min of sputtering have been reduced to between 5.1 eV and 5.3 eV. There are two possible explanations for this reduction, the first being that the argon ion sputtering has not only stripped away the residual DCB, but also the chlorine that has been functionalized to the ITO. The second explanation is that the argon ions have been physisorbed in the ITO surface. Since argon ions are positively charged, it will

not only roughen the surface but also alters the surface potential across the surface. To determine the cause of WF reduction, XPS was used to determine the amounts of carbon, chlorine and argon on the samples relative to the indium present in ITO before and after the sputtering process.
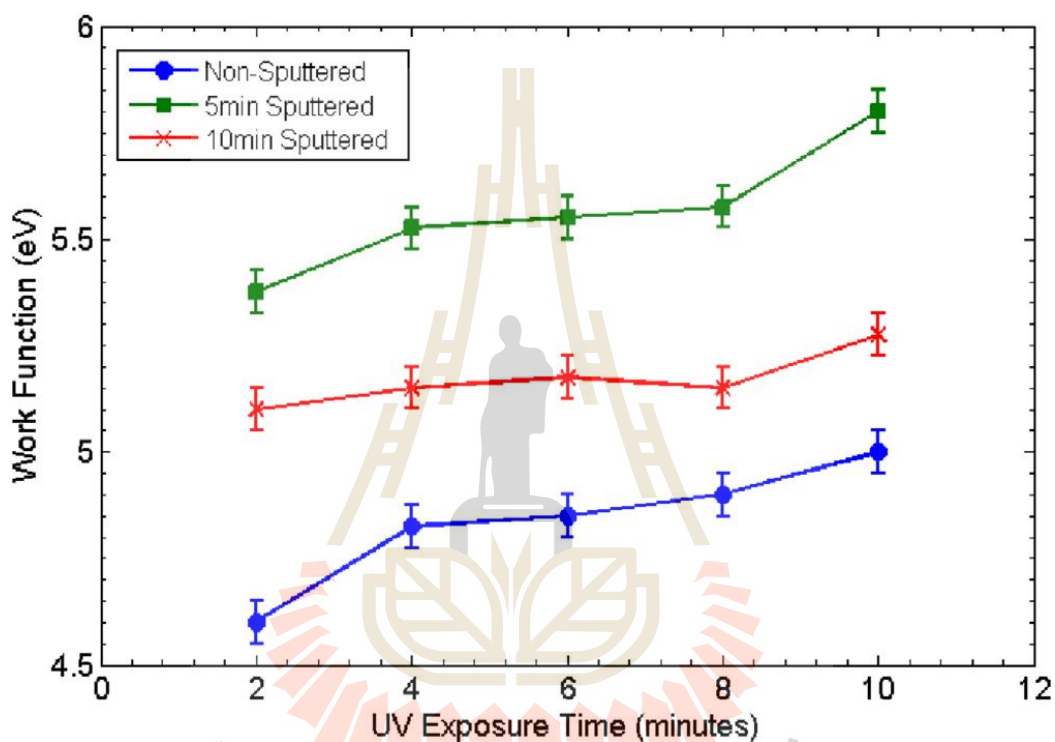


**Figure 4.17** The work function of the chlorinated ITO samples as a function of UV exposure time during the functionalisation process. The bottom line is before any Argon ion sputtering, the top line is 5 min of sputtering and the middle line is 10 min of sputtering.

Figure 4.18 shows the number ratios of the carbon 1s peak, the chlorine 2p peaks and the argon 2p peaks relative to the indium 3d peaks as a function of the UV exposure time in plots (a), (b) and (d) respectively and plot (c) shows the ratio of the

carbon 1s peak to the chlorine 2p peaks. The number ratios between two elements were calculated using the atomic sensitivity factors for each spectral line follow by

$$\frac{n_x}{n_y} = \frac{I_x/S_x}{I_y/S_y}$$

where $I_x, I_y$ are the relative peak area of photoelectrons from element x and y, $n_x, n_y$ are the number of atoms of the element x and y per volume area of the surface, $S_x, S_y$ are the atomic sensitivity factor.

Figure 4.18(a) shows the carbon-indium ratio, the reduction of carbon after Ar ion sputtering for the first 5 min comparing to before sputtering. It was found that most of the carbon contamination has been removed from the surface. The carbon present on the ITO surface is a result of the residual chloro-carbon (Cl-C) fragment in the samples combined with exposure to the atmosphere in the form of free contaminants. There is a further, the smaller reduction in carbon after sputtering 5 min again. The total reduction of carbon contamination is about 6-7% from the initial value.

Figure 4.18(b) shows the chlorine-indium ratio that the chlorine has also been reduced in the ITO surface after Ar ion sputtering. For the first 5 min of sputtering the amount of chlorine has been reduced a haft of the initial value, this might be due to the removal of chloro-carbon fragment from the surface which giving a maximum WF of 5.8 eV. However It is may also have been removed some of the functionalized chlorine. Then the amount of chlorine has been is halved after a further 5 min of sputtering again. The WFs of the samples haven not been increased opposite side the WF have been reduced, this may result from the functionalized chlorine on the ITO surface was be removed that result to lower the WF.

Figure 4.18(c) shows the carbon-chlorine ratio before and after the argon ion sputtering. For the first 5 min, it is clear that the carbon is removed from the sample more than chlorine. In detail it is consistent with the removal of chloro-carbon (Cl-C) fragment and carbon contamination from the surface. However, after sputtering 5 min again there is little change in terms of carbon-chlorine ratio.

Figure 4.18(d) shows the argon-indium ratio the presence of argon within the sample surface after 5 min of argon ion sputtering. After 10 min, the amount of argon in the sample surface doubled and that it is comparable to the amount of chlorine in the sample as seen in Figure 4.18(b). Before the sputtering there is obviously no argon within the sample.

These results suggest that the amount of chlorine in the DCB treated ITO samples for a, when it is clear from Figure 4.17 that it does not correspond to the highest WF of the samples. The sample with the highest WF had a UV exposure time of 10 min but from Figure 4.18(b) it has the second lowest amount of chlorine with respect to the indium. In order to whether the chlorine is originated from chloro-carbon fragment or from chemically bonded chlorine on ITO surface, we exam the high-resolution XPS spectra of chlorine 2p peak. This is shown in Figure 4.19 for the 6 min and 10 min samples that have been sputtered for 5 min.

In opposition, at the amount of chlorine in the ITO, the UV exposure time of 6 min is a maximum amount. But it does not correspond to the highest WF of the samples. In contrast, a UV exposure time of 10 min was obtained the highest WF with the second lowest amount of chlorine with respect to the indium. It is especially important in the case of chlorine is originated from chloro-carbon fragment or from

chemically bonded chlorine on ITO surface. The high-resolution XPS measurement was used to demonstrate for the elements characterization.
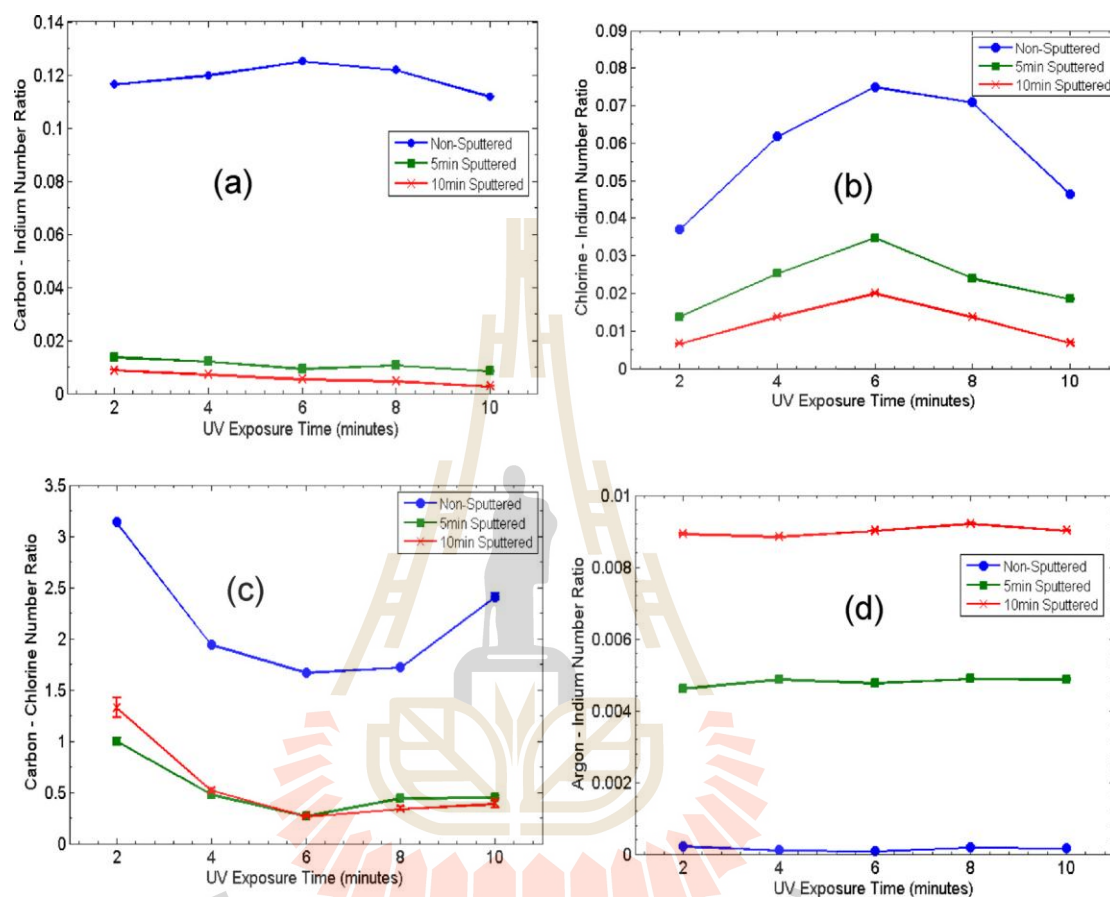


**Figure 4.18** Plots showing the number ratio of two integrated spectral peaks as a function of the UV exposure times and argon ion sputtering times. (a) Carbon 1s to indium 3d, (b) chlorine 2p to indium, (c) carbon to chlorine and (d) argon 2p to indium.

Figure 4.19 shows XPS spectra of the chlorine 2p as a UV exposure times for (a) 6 min, (b) 8 min and (c) 10 min. The samples have been sputtered by 0.5-keV Ar ions for 5 min to remove residual carbon contamination. XPS was performed on the samples using the excitation photon energy of 400 eV. As expected, the measurement

results shown that the chlorine 2p peak can be separated into spin-orbit splitting with the $2p_{1/2}$ and $2p_{3/2}$ (j = 1/2 and j = 3/2) for the 6 min, 8 min and the 10 min UV exposure.

In the 6-min UV exposure samples, shown in Figure 4.19(a), there are two peaks at a lower energy of 200.5 eV for the j = 3/2 orbital and higher energy of 202.5 eV for the j = 1/2 orbital. These two significantly assigned to the carbon-chlorine (Cl-C) bond which indicated residual chloro-carbon fragment.

In the 8-min UV exposure samples, shown in Figure 4.19(b), two components are observed consist of the carbon-chlorine (Cl-C) (at the same position with 6 min samples) and indium-chlorine (Cl-In) at peaks energy of 119.0 eV for the j = 3/2 orbital and higher energy of 201.0 eV for the j = 1/2 orbital.

In the 10-min UV exposure samples, shown in Figure 4.19(c), there are consist of two peaks that assigned to indium-chlorine (Cl-In) (at the same position with 8-min UV exposed samples)

The most interesting peak appears in the indium-chlorine bond cannot be obtained. This could be result to insufficient functionalize on the ITO surface. However, the majority of the chlorine has been bonded to the indium for 8 min and the maximum in the 10 min sample. This means that although the 6 min sample has more chlorine as seen from Figure 4.19, but it does not correspond to the highest WF because the majority of it is from chloro-carbon fragment.

Figure 4.20 shows the chlorine 2p XPS spectra for the 10 min UV exposure sample after 10 min of argon ion sputtering. A comparison between Figure 4.19(c) and 4.20 shows that the chlorine-indium has been significantly reduced in the intensity. This could also be result to the reduction of WF as seen in Figure 4.17.

It can concluded that the initial WFs of the chlorinated samples were low. This is due to the presence of the residual DCB and chloro-carbon fragment after the chlorination. These surface contaminations could be removed by using argon ion sputtering. The WF can be increased and found that functionalisation only occurs after more than 6 min of UV irradiation. For samples that have been irradiated with UV light for 10 min, most if not all, of the chlorine has been bonded to the indium. Further sputtering more time results in removal of functionalized chlorine on ITO and also decreased the WF.
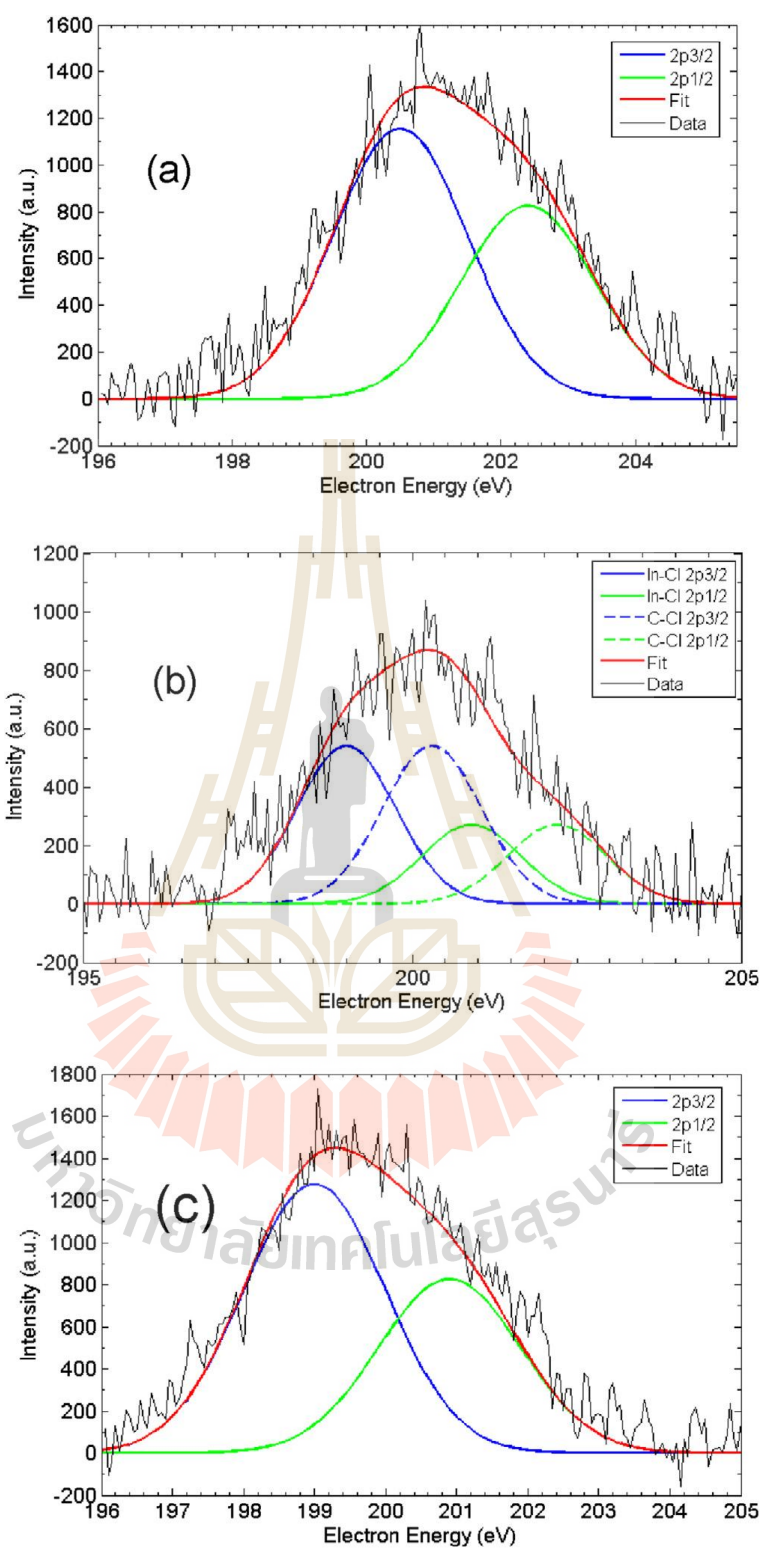
**Figure 4.19** The chlorine 2p XPS spectra for the 6 min UV exposure sample, (b) 8 min UV exposure sample and (c) the 10 min UV exposure sample. The samples have been sputtered for 5 min to remove residual carbon.
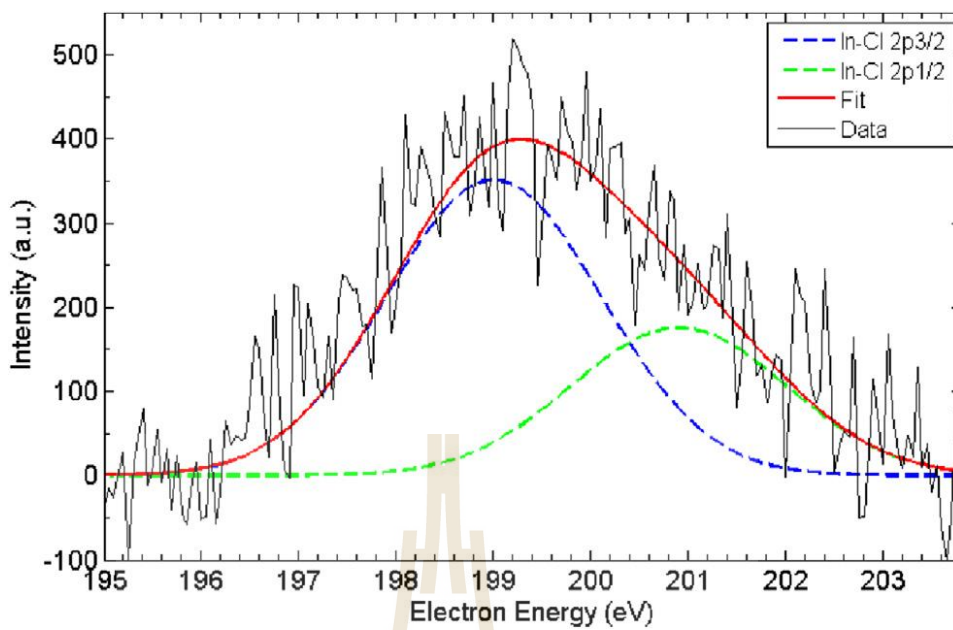
**Figure 4.20**　　The chlorine 2p XPS spectra for the 10 min UV exposure sample after

10 min of argon ion sputtering.

### 4.3.2 Surface treated by using caesium fluoride

Figures 4.21(a) shows photoelectron spectra of the ITO in the region of the low energy cut-off (high kinetic energy cut-off) that represent the valence band maximum (VBM) of the ITO. The results shown that the VBM of the ITO samples are at 3.1 eV with respect to the Fermi level. It is noted that the Fermi level is obtain from a clean gold sample. It is obvious that all CsF treated samples have the same energy level of VBM. This implies that the surface modification by CsF have no impact on the energy level of VBM.

Figure 4.21(b) shows photoelectron spectra of the ITO samples with different CsF concentrations in the region of the secondary electrons cut-off. There is a large difference in the spectra between the samples with the most dilute and most concentrated of CsF. The sample with concentration of 2 mg ml$^{-1}$ CsF is shown the cuts off below 34 eV, while 50 mg ml$^{-1}$ CsF is shown the cut-off about 34.5 eV. This results implies an increased the WF as the concentration of CsF decreases. The samples of 2 mg ml$^{-1}$ CsF ITO is recorded the highest WF. Thus, a plot of the WF as a function of modified ITO as a function of the concentration of CsF solution is shown in Figure 4.22.

Figure 4.22 shows the WF of modified ITO samples as a function of the concentration of CsF. They are separated into two sets of concentration of CsF. First set, it is obvious that the WF is maximum at 5.75 eV with CsF concentration of 2 mg ml$^{-1}$. Then, the concentration increases up to 50 mg ml$^{-1}$, the WF was steady declined to lowest of 5.33 eV. However, ITO WF is still improved if compare to the WF of plain ITO of this set is about 5.1 eV and also the WF of gold is 5.1 eV too. Normally, ITO has a WF of between 4.40 and 4.80 eV depending on the method used to clean

the surface. For this set ITO was cleaned by $O_2$ plasma treatment before modified the ITO surface.
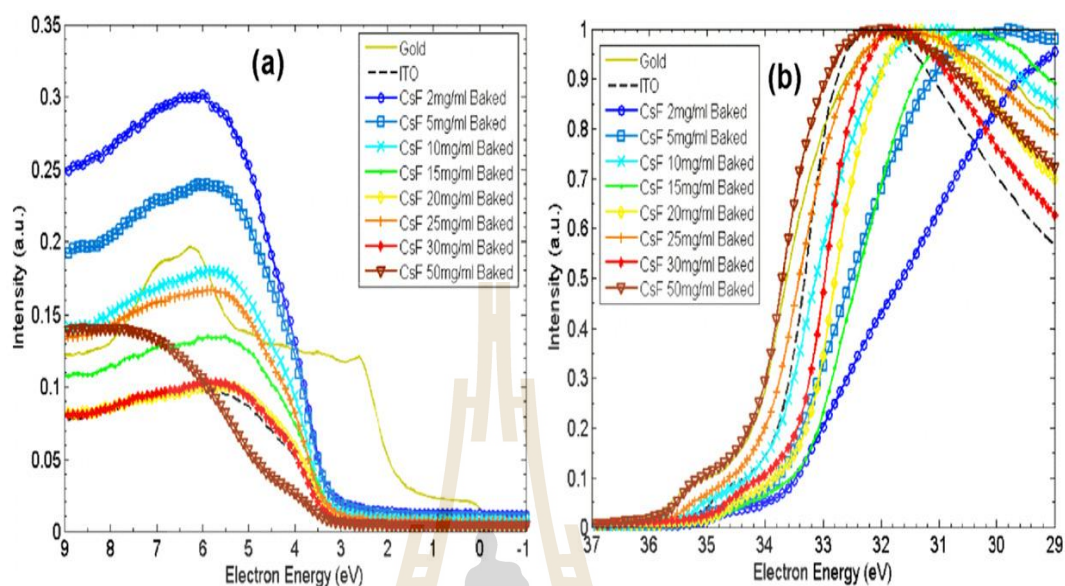


**Figure 4.21**  Low energy end of the normalized ultraviolet photoelectron spectra of baked modified ITO. (b) High energy end of the normalized UPS of modified ITO.

Additional, to improve the WF of ITO, there must be considered to lower concentrations of CsF solution. The second set of CsF functionalized ITO samples was observed with concentrations of 0.04, 0.1, 0.25, 0.5, 1, 2, 5 and 10 mg ml$^{-1}$.

In the second set, it was found that the WF can be increased when the CsF concentration increases up to 2 mg ml$^{-1}$ and then the WF is decreased for the CsF concentrations of 5 and 10 mg ml$^{-1}$ as demonstrated by the first set. However, it must be noted that the WFs recorded for the second set of samples are slightly lower by 0.1–0.15 eV for the CsF concentrations of 2, 5 and 10 mg ml$^{-1}$. These results were caused by the contamination of the sample surface by atmospheric elements that can be confirmed by the detection of C1s peaks in XPS data.
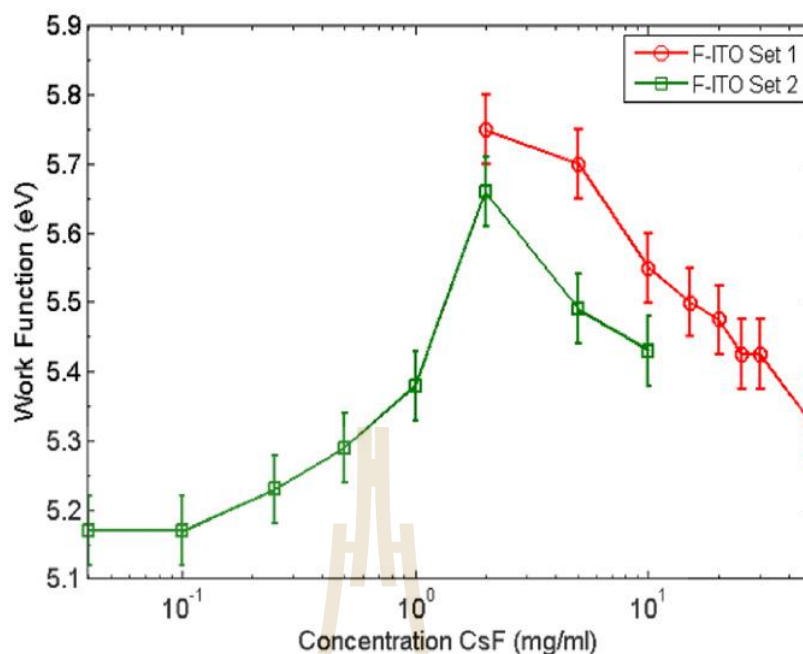
**Figure 4.22**    The WF of modified ITO as a function of the concentration of CsF.
The red line represents the first set of modified ITO samples while the
green line is the second set of modified ITO samples using lower
concentrations of CsF.

Figure 4.23(a) shows the XPS spectra of F1s for the F-ITO samples with CsF
concentration of 2, 5, 10, 25 and 50 mg ml$^{-1}$. The F1s peak is shown very small
intensities for 2, 5, 10, and 25 mg ml$^{-1}$. However, apart from the strongest CsF
concentration at 50 mg ml$^{-1}$, it is important to note that there is very little to no
fluorine within the other samples. Consequently, the fluorine coverage which were
expected on our ITO samples is no longer present and is not contributing to the
increase in WF. Although the absence of fluorine in the samples, surprisingly, the WF
still changes with increasing CsF concentration up to 2 mg ml$^{-1}$.

Figure 4.23(b) shows Gaussian curve-fitting of the F1s peak for 50 mg ml$^{-1}$
sample. The indium auger background of the spectra was subtracted using the Shirley

background. The F1s spectrum consists of three components. The first one at 684.2 eV is assigned to the indium-fluorine bond (In–F). The second at 685.9 eV is assigned to the caesium–fluorine bond (Cs–F). The third at 687.0 eV is attributed to the carbon–fluorine bond (C–F). The Cs–F curve is the largest and this represents the residual CsF after DI water washing. The In–F curve indicates that there is some InF$_3$ remaining after the sample was washed. Although this is very small compared to the residual CsF, it shows that the fluorine has indeed been functionalized to the surface of the ITO. The C–F curve shows that some contamination in the form of carbon has also bonded with the fluorine. This indirectly shows that baking the CsF solution results in the release of fluorine.
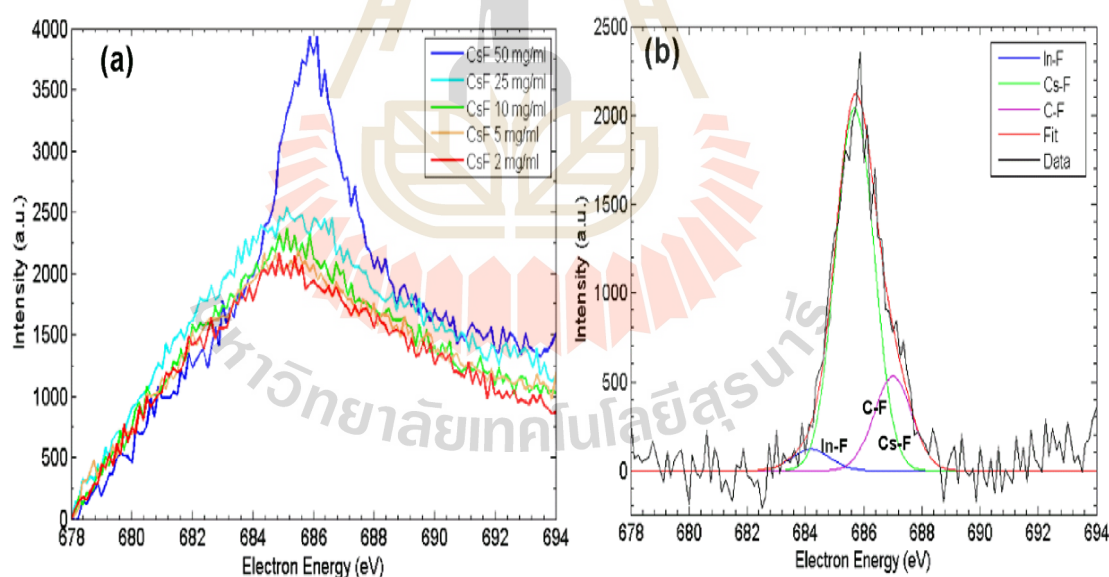


**Figure 4.23**   The XPS spectra of F1s for the F-ITO samples with CsF concentration of 2, 5, 10, 25 and 50 mg ml$^{-1}$. (b) Gaussian curve-fitting of the F1s peak.

Table 4.3 shows the In, O and Sn atomic content of ITO surface with the concentration of CsF solution of 2 , 5, 10, 25 and 50 mg ml$^{-1}$. When CsF concentration increase, it shows that the increase of oxygen content is about 4%. However the indium and tin content decreases by approximately 4% and 0.4% respectively. This could only be explained by the loss of indium and tin by washing. There is also an increase in oxygen which is attributed to the loss of indium and tin, resulting in a change in the relative ratio between indium, tin and oxygen.

The increase of oxygen content in ITO only explain in case of increase the WF However, this does not explain the decrease in WF seen for higher CsF concentrations.

**Table 4.3**    The atomic content of ITO samples were performed with the concentration of CsF solution of 2 , 5, 10, 25 and 50 mg ml$^{-1}$.

| CsF Concentration | Chemical composition in at. % | | |
|---|---|---|---|
| (mg ml$^{-1}$) | O | In | Sn |
| 2 | 62.32 | 34.46 | 3.22 |
| 5 | 62.61 | 34.03 | 3.36 |
| 10 | 62.58 | 34.21 | 3.21 |
| 20 | 63.30 | 33.59 | 3.11 |
| 50 | 66.81 | 30.38 | 2.81 |

Recently, it has been demonstrated that the electronic WF of a copper can also be related to its surface roughness when the effect of grain sizes and textures are

minimized. The loss of indium and tin in our samples will change the physical surface of the ITO and affection of surface have to be evaluated.

Figure 4.24 shows the AFM images of modified ITO surface of the samples with CsF concentrations of (a) plain ITO, (b) 2 mg ml$^{-1}$ and (c) 50 mg ml$^{-1}$. The first sample shown in Figure 4.24(a) is untreated ITO and has a moderately rough surface. This is then smoothed out as the concentration of CsF is increased to 2 mg ml$^{-1}$. This is indicated in Figure 4.24(d) where both the average and root-mean squared surface roughness ($r_{av}$ and $r_{rms}$) are shown to be higher for the untreated ITO at 1.55 nm and 2.20 nm, respectively, compared to the samples with lower concentrations of CsF. The 2 mg ml$^{-1}$ CsF sample has the lowest $r_{av}$ and $r_{rms}$ measured at 0.96 nm and 1.23 nm, respectively.

From the 2 mg ml$^{-1}$ CsF sample, $r_{av}$ and $r_{rms}$ start to increase with the 50 mg ml$^{-1}$ sample in Figure 4.24(c) showing more numerous and larger peaks in the surface. The $r_{av}$ given by AFM measurements for the 25 and 50 mg ml$^{-1}$ samples is 1.62 and 2.30 nm, while the $r_{rms}$ is 2.20 nm and 3.23 nm. This is an overall increase of 2.4 and 2.6 times the original values from the 2 mg ml$^{-1}$ CsF to the 50 mg ml$^{-1}$ CsF samples.

The decrease and subsequent increase in surface roughness and the relative increase in oxygen content of the ITO samples both contribute to the change in WF as seen in Figure 4.22. Whilst the change in the composition of the modified ITO is very small, the slight levelling of the surface helps to increase the WF to 5.75 eV. However, the damage to the surface of the samples is ultimately what drives the WF back down to a value of 5.33 eV, despite the increasing oxygen content. This indicates that the change in surface roughness has a greater effect on the WF than the change in the ITO composition. This can be explained by the fact that the localized

surface potential difference increases when the surface is rougher. The electrons in a trough in the ITO surface are surrounded by more nuclei resulting a higher potential at that point. However, the electrons in an atom near the peak of ITO surface have relatively fewer surrounding nuclei and will have a lower potential. This creates a potential difference which is proportional to the distance between the peak and trough. This directly affects the WF as the potential difference will help an electron escape to the surface. Thus, an increase of surface roughness of ITO will result in lower WF.
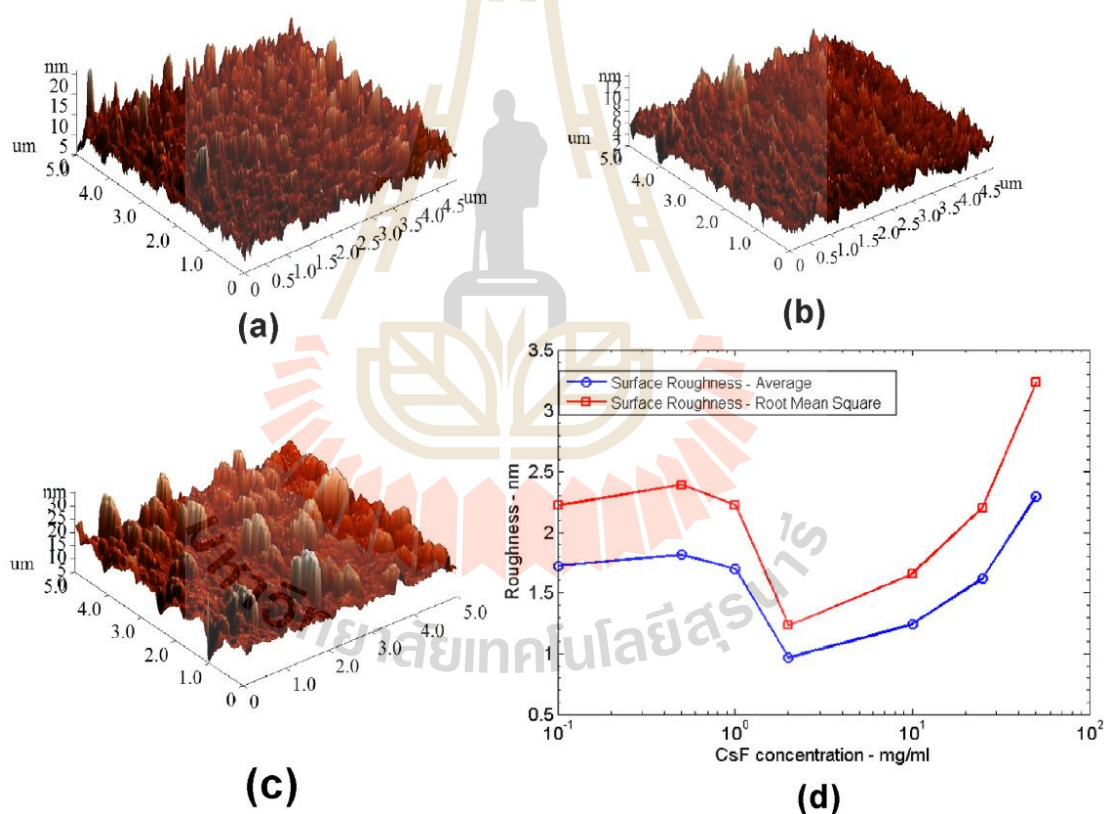


**Figure 4.24**    Atomic force microscopy (AFM) images of the surface of the (a) plain ITO and the modified ITO samples at CsF concentrations of (b) 2 and (c) 50 mg ml$^{-1}$. (d) The average (blue) and root-mean squared (red) surface roughness ($r_{av}$ and $r_{rms}$) of the ITO samples as a function of the concentration of CsF solution used.

## 4.4    References

Beerbom, M. M., Lägel, B., Cascio, A. J., Doran, B. V. and Schlaf, R. (2006). Direct comparison of photoemission spectroscopy and in situ Kelvin probe work function measurements on indium tin oxide films. **Journal of Electron Spectroscopy and Related Phenomena** 152: 12.

Helander, M. G., Wang, Z. B., Qiu, J., Greiner, M. T., Puzzo, D. P., Liu, Z. W. and Lu, Z. H. (2011). Chlorinated Indium Tin Oxide Electrodes with High Work Function for Organic Device Compatibility. **Science** 332: 944.

Park, Y., Choong, V., Gao, Y., Hsieh, B. R. and Tang, C. W. (1996). Work function of indium tin oxide transparent conductor measured by photoelectron spectroscopy. **Applied Physics Letters** 68: 2699.

Schlaf, R., Murata, H. and Kafafi, Z. H. (2001). Work function measurements on indium tin oxide films. **Journal of Electron Spectroscopy and Related Phenomena** 120: 149.

Song, W., So, S. K. and Cao, L. (2001). Angular-dependent photoemission studies of indium tin oxide surfaces. **Appl Phys A** 72: 361.

Sugiyama, K., Ishii, H., Ouchi, Y. and Seki, K. (2000). Dependence of indium--tin--oxide work function on surface cleaning method as studied by ultraviolet and x-ray photoemission spectroscopies. **Journal of Applied Physics** 87: 295.

Thomas, J. W., Keat Hoe, Y., Yi Bin Calvin, N., Noor Azrina, T., Chong Lim, C., Kai Lin, W., Narong, C., Hideki, N., Thanit, S., Prayoon, S., Steffen, O. and Boon Kar, Y. (2013). Enhancement of the work function of indium tin oxide by surface modification using caesium fluoride. **Journal of Physics D: Applied Physics** 46: 475102.

Wang, R. X., Beling, C. D., Djurišić, A. B., Li, S. and Fung, S. (2004). Properties of ITO thin films deposited on amorphous and crystalline substrates with e-beam evaporation. **Semiconductor Science and Technology** 19: 695.

Whitcher, T. J., Yeoh, K. H., Chua, C. L., Woon, K. L., Chanlek, N., Nakajima, H., Saisopa, T. and Songsiriritthigul, P. (2014). The effect of carbon contamination and argon ion sputtering on the work function of chlorinated indium tin oxide. **Current Applied Physics** 14: 472.

Yi, Y., Lyon, J. E., Beerbom, M. M. and Schlaf, R. (2006). Characterization of indium tin oxide surfaces and interfaces using low intensity x-ray photoemission spectroscopy. **Journal of Applied Physics** 100: 093719.
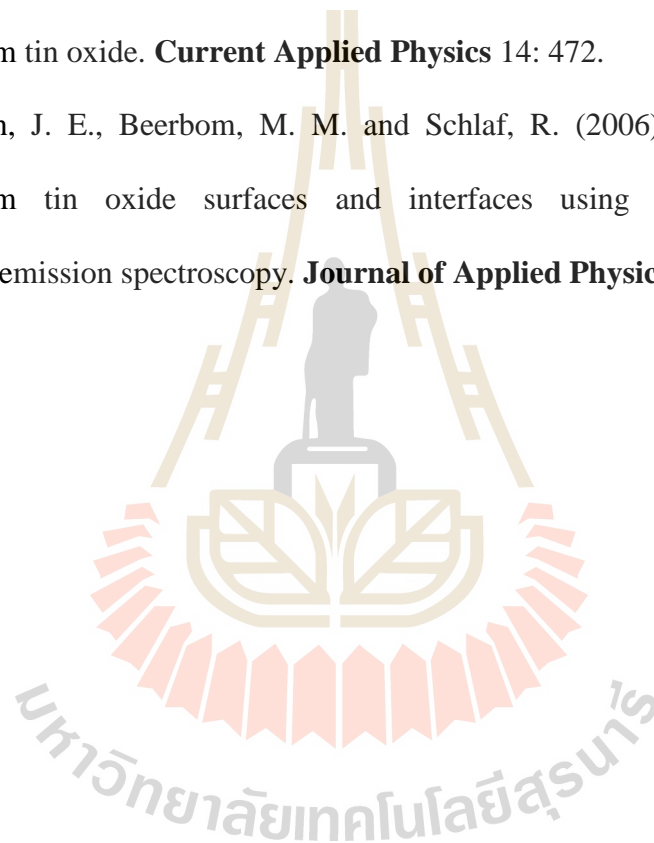
# CHAPTER V

# CONCLUSIONS AND REMARKS

This thesis demonstrates that the WF of ITO can be altered by VUV irradiation, zero-order light irradiation, surface contamination, and surface treatments. In VUV irradiation, it was shown that the reductions of the WF of 3.5%, 3.0% and 1.5% after exposed to VUV with photon energy of 40, 60 and 80 eV, respectively, at photon fluence of $1.5 \times 10^{18}$ photons/cm$^2$. It is obvious that VUV light with lower photon energy gives the higher influence on the reduction of the WF. At lower photon energy, the penetration power of the radiation is lower. In the other word, the top most layer, surface contaminations, absorbs more photons with lower energy than higher ones. The absorbed energy may causes the reduction in the surface contaminations resulting in the decrease in the WF of ITO. This assumption has been experimentally confirmed; when the surface contaminations were removed, no change in the WF was observed after VUV irradiation. Whenever, surface contaminations exist the reduction of the WF of ITO is always observed. This was confirmed with air and oxygen exposure measurements.

It is interesting to point out that the WF of ITO can be increased by irradiating with the zero-order light. It was found that the WF of chemically cleaned ITO could be increased by 10%, 12% and 14% when irradiated with the zero-order light for 10, 20 and 30 min, respectively. The cause for the increase may be due to the formation of a dipole layer of the surface contaminations after exposing to the high photons flux

of the zero-order light. The dipole layer becomes more effective in increasing the WF of ITO as the thickness of the dipole layer reduces.

When the surface of ITO was chlorinated, the WF of Cl-ITO with a maximum WF of 5.8 eV could be obtained. The effects of carbon contamination and argon ion sputtering on the WFs of the chlorinated samples were examined by elemental core-level PES analyses. By using argon ion sputtering to remove the residual DCB and chloro-carbon fragment a drastic increase in the WF is recorded. PES core level spectra were taken to determine whether the chlorine has been bonded to the indium tin oxide for the samples and found that functionalisation only occurs after more than 6 min of UV irradiation for the chlorination. For the samples that have been chlorinated for 10 min, most if not all, of the chlorine has been bonded to the indium. Further sputtering results in removal of functionalized chlorine on ITO.

In fluorination treatment, the surface of the ITO samples were modified by using varying concentrations of CsF solution. It was found that the WF of the modified samples increased to a maximum of 5.75 eV. However, the WF decreases as the concentration of CsF solution continues to increase, resulting in an optimal CsF solution of 2 mg ml$^{-1}$. It was found that the change in WF due to surface roughness overrides the change in WF due to elemental composition, indicating that physical changes have a more profound effect on the WF than chemical changes.

Base on the results obtained from this thesis work, further studies are required to fully understand the mechanism behind the change of the WF of ITO induced by electromagnetic wave. It is interesting to carry out further study on the increase of WF after irradiating by zero-order light by investigating carbon species before and after the irradiation in order to understand what kinds of chemistry occurring during the

irradiation. It is also interesting to investigate influence of higher photon energy on the change of the WF.

For chlorinated ITO surface, more works are needed to understand the atomic arrangements at the chlorinated ITO surface. This may be studied by a combined computational works with surface X-ray absorption experiments.
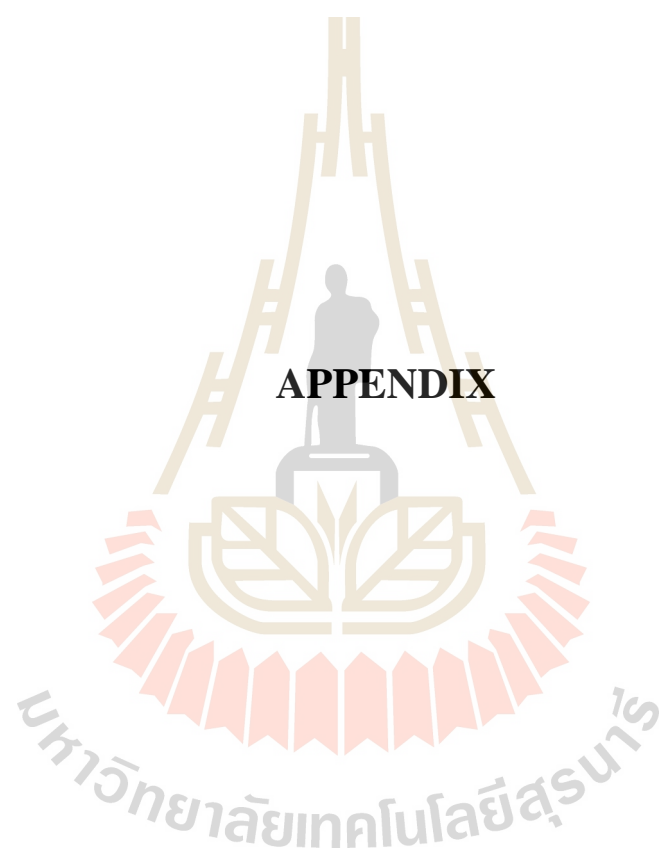
**APPENDIX**

# APPENDIX

During the course of this thesis work, the research results were published or presented in/at the following scientific journals or conferences:

1. T.J. Whitcher, K.H. Yeoh, C.L. Chua, K.L. Woon, N. Chanlek, H. Nakajima, <u>T. Saisopa</u>, P. Songsiriritthigul, **The effect of carbon contamination and argon ion sputtering on the work function of chlorinatedindium tin oxide,** Current Applied Physics 14 (2014): 472-475.

2. T.J. Whitcher, K.H. Yeoh, Y.B.N. Calvin, N.A. Talik, C.L. Chua, K.L. Woon, N. Chanlek, H. Nakajima, <u>T. Saisopa</u>, P. Songsiriritthigul, S. Oswald and B.K. Yap, **Enhancement of the work function of indium tin oxide by surface modification using caesium fluorid**, Journal of Physics D: Applied Physics 46 (2013): 475102.

3. T.J. Whitcher, K.L. Woon, W.S. Wong, N. Chanlek, H. Nakajima, <u>T. Saisopa</u> and P. Songsiriritthigul, **Interfacial behavior of resistive switching in ITO-PVK-Al WORM memory devices**, Journal of Physics D: Applied Physics 49 (2016): 075104.

4. T.J. Whitcher, N.A. Talik, K.L. Woon, N. Chanlek, H. Nakajima, <u>T. Saisopa</u> and P. Songsiriritthigul, **Determination of energy levels at the interface between $O_2$ plasma treated ITO/P3HT : PCBM and PEDOT : PSS/P3HT : PCBM using angular-resolved x-ray and ultraviolet photoelectron spectroscopy**, Journal of Physics D: Applied Physics 47 (2014): 055109.

5. **Modifications of work function of ITO by synchrotron irradiation,** (in manuscript).

6. C. Songsiriritthigul, <u>T. Saisopa</u>, M. Phanak, N. Mothong, N. Yachum,S. Chidchob, N. Sumano, P. Songsiriritthigul, **Soft X-ray Fluorescence Spectroscopy at the Siam Photon Laboratory,**the3[rd] ACADEMIC CONFERENCE ON NATURAL SCIENCE FOR MASTER AND PhD STUDENTS FROM ASEAN COUNTRIES (CASEAN 2013), Cambodia.

7. T. Saisopa, H. Nakajima, N. Chanlek, and P. Songsiriritthigul, **In-situ Photoemission Study of Copper (II) phthalocyanine and Pentacene Thin Films,** Siam Physics Congress SPC2014, 26-29 March 2014.
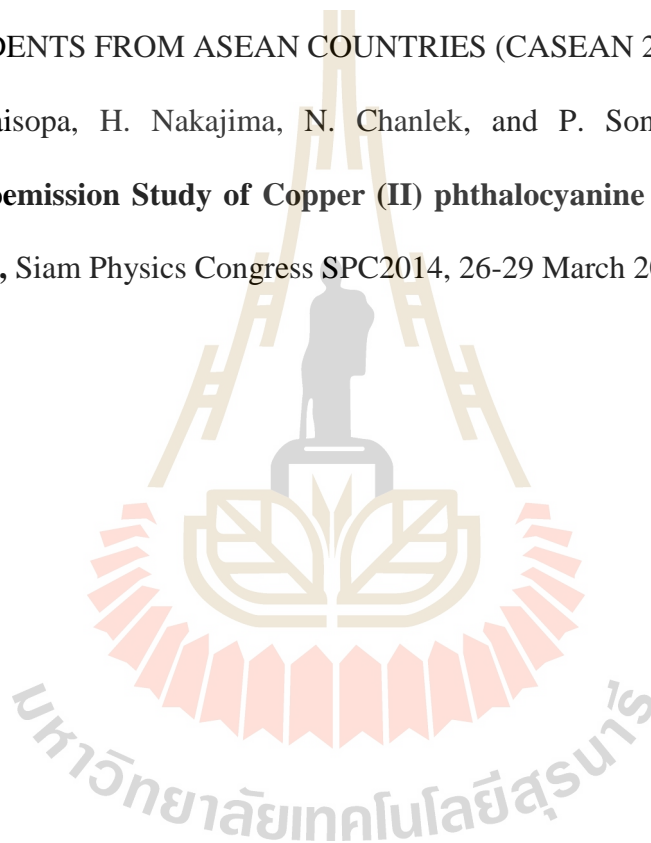
# CURRICULUM VITAE

**Name :**                      Mr. Thanit  Saisopa

**Nationality :**               Thai

**Date of Birth :**             11 January 1987

**Address :**                   115 Mu.3, T. Dorn, Pakthongchai District,

Nakhon Ratchasima, 30150 Thailand

Tel. +66-86-2457168

**E-mail :**                     t.saisopa@gmail.com

**Education Background :**

2005-2009      B.Sc. (Physics) Khonkaen University, Khonkaen, Thailand.

2009-2016      Ph.D. (Physics) Suranaree University of Technology with scholarship from the Science Achievement Scholarship Program of Thailand (SAST), Nakorn Ratchasima, Thailand.

**Work Experience :**

1. Ph.D. Research at Department of Physics and Astronomy at Uppsala University (UU), Uppsala, Sweden.

2. Ph.D. Student Research Assistant at Photoemission beamline BL3.2a at Synchrotron Light Research Institute (Public Organization), Thailand.

3. Teaching Assistant at Laboratory, School of Physics, Suranaree University of Technology, Thailand.